An experimental and simulation framework for the characterization of the structural response of fiber reinforced concrete manufactured with EAFS

Aratz García Llona

Supervisors: Vanesa Ortega López

Ignacio Piñero Santiago

Department of Civil Engineering

Universidad de Burgos

This dissertation is submitted for the degree of

Doctor of Philosophy

February 2020

Acknowledgements

Neure gurasoei eskainia...

Abstract

The limited regulatory framework covering fiber reinforced concrete limits the application of it in structural elements. Design guidelines, such as Model Code [38] or Spanish Structural Concrete Code (EHE-08) [108], show weaknesses that results in a limited application of this composite in structural elements. For this reason, the proposed framework combined experimentation, which provided mechanical expertise of the material, and simulation, which extended the applicability to structural elements.

The leading question when fiber reinforced concrete elements are being designed, is how many fibers must be added to gain the required structural strength. The answer of this question is not a simple task since the performance of the composite depends on the matrix, the fibers and the interaction between them [83, 164, 174, 194].

Furthermore, the used concrete had also the particularity that natural aggregates were substituted by Electric Arc Furnace Slag (EAFS). Reusing EAFS as aggregate did not result only in an environmental benefit, but also improved the mechanical performance of concrete [59, 151, 152]. Concrete had also to comply workability conditions (self-compacting or pumpable), in spite of the weight of EAFS.

In this context, the performance of four mixes were studied along this dissertation. The mixes were made with synthetic or steel fibers and different types of cements [152]. The planed experimentation provided properties of the mixes to asses the performance of the material in terms of durability, workability and mechanics. A direct vision along with material properties brought also a valuable understanding of the behavior of fiber reinforced concrete at the material level. Therefore, the purpose of the experimentation was also to increase the confidence upon the mechanical performance of the material.

The tests were also planned to provide the inputs required by the numerical model. The developed in-house Finite Element Method (FEM) code was based on interface elements to model the fracture of concrete [100, 150] and the bridging phenomena due to the addition of fibers. Two damage models and an elastoplastic model were implemented to model the behavior of concrete, fibers and reinforcement.

The numerical tool enabled to extend the conclusion of the experimentation and reduce the extension of experiments. A calibrated numerical model allowed also to make a leap from material scale to structural scale.

In summary, the dissertation proposes a method that consists in an experimental part, which studied the properties of the material and was used also to calibrate the constitutive models, and in a numerical part, where an in-house FEM code was developed to design structural elements.

"Life is like riding a bicycle. To keep your balance you must keep moving"

- Albert Einstein

Table of contents

List of figures

List of tables

Chapter 1

Introduction

1.1   Introduction and research group background

This thesis is part of the research line developed during the last decades by Universidad de Burgos (UBU), Euskal Herriko Unibertsitatea (UPV/EHU), Universidad de Cantabria (UC) and Tecnalia Research & Innovation (Tecnalia). They have shown, among other developments, that electric arc furnace slag (EAFS) can be used as a replacement for natural aggregates in concrete [12, 13, 59, 98, 96, 97, 151, 153, 159]. Over the last decades, several papers and studies have been published from the dissertations supervised by the mentioned research groups as it is reported in Figure 1.1.

Concrete is one of the most common construction material [137] and it is the result of the development of many years [102, 103]. Many research groups have worked on it to improve its properties and to increase the understanding of its behavior [36, 64, 94, 126, 136, 76]. There are several different aspects in which experts have been working on, from micro-scale study of chemical reactions which take place during the curing [193] to structural behavior, such as bridge columns [104].

Nevertheless, concrete has weaknesses that may be solved in several different ways and one of them is by adding fibers. The use of fibers to improve its behavior is not new [206]. Fiber reinforced concrete is a composite material consisting of a mix of concrete and dispersed fibers. The properties of the composite vary considerably depending on the type of concrete and fibers used [164]. The high variability and heterogeneity of the material, along with its mechanical behavior make it less known and reliable than the conventional concrete [61]. Furthermore, the uncertainties surrounding this material are still greater in some countries due to a lack of a normative to be followed.

Despite the fact that many studies have been carried out to show the advantages of the material [22, 55, 36, 82, 164], it is not widely used in the design of structural elements

SLAG FROM STEEL INDUSTRY AS AGGREGATE FOR CONCRETE

Ladle furnace slag (LFS)
A. Rodriguez's PhD(2008):
- Analysis of the characteristic of masonry mortars made of LFS.

T. Herrero' PhD (2015):
- Characterization and study of the durability of mortars.

Mixture of LFS and EAFS
M. Losañez's PhD (2005):
- Study of LFS and EAFS mixture to make concrete.
- Deepen knowledge of dosage rate of concrete.

M. Skaf's PhD (2016):
- Study of EAFS and LFS mixtures in porous asphalt mixtures.

V. Ortega-López's PhD(2011):
- Application of LFS and EAFS in soil stabilization and road Surface layers.

Electric arc furnace slag (EAFS)
J.M. Manso's PhD (2001):
- EAF slag is suitable to be used as aggregate.
- Promising results have been showed.

I. Arriba's PhD (2011):
- Confirmation of mechanical and durability properties.
- Real application: Foundation and basement walls.

J.A. De la Fuente's Phd (2015):
- Study of the behavior of concrete made of EAF slag and steel/synthetic fibers.

A.Santamaria's PhD (2017):
- Analyze structural behavior: Pumpable and self-compacting concrete.

A. Esteban's Phd (2018):
- Study of acoustic performance of concrete made of EAFS.

This thesis:
- Numerical simulation of SFRC: Bridging behavior and fracture.
- Experimental/Numerical framework for the design of structural elements.

ACHIEVEMENTS
- Use of slags (LFS and EAFS) from steel industry as aggregate to fabricate **high performance hydraulic material:** mortar, bituminous mixture and concrete.
- **Standardization** and setting of rules for the design:
  - Pumped concrete.
  - Self-compacting concrete.
  - Fiber reinforced concrete.
  - Structural performance, durability, rolling resistance and acoustic performance.
- Study at different **scales:** microscale and mesoscale.

Fig. 1.1 Research group's experience

yet. Fibers provide certain advantageous properties that extend the use of concrete and new performances might be developed [36]. Therefore, reliable calculation tools are needed to design structural elements [77]. A framework that combines experimental and numerical results might increase the trustability and applicability of the material [120]. The experimental data do not only feed the numerical tool, it also provides a real vision of the mechanical behavior. Whereas the numerical results allow extending the behavior of the material, enabling it to apply in the design of structural elements [120].

In addition, Electric Arc Furnace Slags (EAFS) from steel industry have been used to make self-compacting concrete [151, 152]. It introduces complexity as well as allow to get a versatile and high performance concrete. It should be noted that there are not using slags as a disposal of waste, but rather as an enriching item. Therefore, a high-performance material is produced from industrial waste avoiding storage problems [12, 13, 151].

Dissertations main goal is proposing a method to design structural elements using fibers reinforced concrete (FRC), where concrete is made with EAFS. The proposed methodology aims to combine numerical and experimental results to overcome the lack of experience. The numerical tool is calibrated through experimental results, enabling simulating more complex behavior. A well-calibrated numerical tool should reflect and extend the conclusions showed thus far.

1.2   Research scope and objectives

The main objective of the thesis is to provide a framework to design structural elements made of fiber reinforced concrete. The proposed framework in this thesis consists in an combination of experiments and numerical models, which intend to make a leap from material scale to structural scale. The experimental part studies the properties of the material and it is also used to calibrate the numerical models. The numerical models provides a tool to simulate the structural response.

In order to attain the main objective, the following outcomes are worth mentioning:

- A mechanical characterization plan is proposed to evaluate the performance of the material and to define the inputs needed by the numerical model. The dog-bone test should be highlighted among all the tests, which has been designed exclusively for this research.

- The properties of concrete made with EAFS are studied. In this dissertation EAFS are not only applied due to environmental considerations. EAFS are used as aggregate to produce concrete with superior properties to the ones made with natural aggregate. The performance of four concrete mixes were studied, where different type of cements and fibers were used.

- An in-house code for finite element analysis of fiber reinforced concrete beams under static load is developed. The structural elements are modeled by using 2D triangular elements and 1D element (reinforcement). The developed code has the capability to postprocess numerically and graphically the results. The numerical results obtained from the in-house FEM code were validated through experimental results.

- The performance of interface elements to model concrete fracture and bridging phenomena due to the addition of fibers is studied. Interface elements allow to introduce softening models, such as tensile damage model and bridging law. The introduction of interface elements requires a new discretization scheme for the reinforcement to allow the development of the cracks.

1.3   Outline of the thesis

The dissertation is structured around four main parts. Chapter 1 and Chapter 2 identifies the aims and scope of the research and provides a background on the the material. Chapter 3 and Chapter 4 focuses on the numerical tool. The finite element model and the constitutive

models are presented and validated through bibliographical results. Chapter 5 and Chapter 6 explains the characterization of the material and the properties of the material are studied. Lastly, Chapter 7 presents the results of the experimental and computational studies which validated the proposed framework. The dissertation ends with a last chapter of conclusions and future works.

- Chapter 2: A review of concrete made with EAFS and reinforced with fibers is presented to give a background on the material studied in the dissertation. The particularities of EAFS concrete are reported and the main properties of the composite are presented.

- Chapter 3: It provides background information on the mechanics of crack formation and propagation. The finite element method is explained and the constitutive models to model the fracture of concrete, the bridging effect of the fibers and the reinforcement are proposed.

- Chapter 4: This chapter deals with the implementation of the FEM. The flowcharts of the damage and elastoplastic models are presented and the finite element model is also presented. The numerical models are validated through bibliographical results. This chapter enables to identify the inputs required by the numerical models.

- Chapter 5: The studied materials are presented by specifying the dosage of concrete and the fresh properties of the different mixes. The specimens, test setup and the measured variables are presented to asses the hardened properties.

- Chapter 6: The experimental results are presented and discussed. The performance of the material is evaluated and the inputs needed to carry out the simulation are reported.

- Chapter 7: The designing framework is presented and applied to design structural elements. In this chapter, the scale is switched from material level to structural approach. Therefore, the proposed framework is used and its applicability demonstrated.

- Chapter 8: The conclusions and recommendations for further research are presented.

Chapter 2

State of art

2.1 Historical aspects

The concept of using fibers as reinforcement is not new. The practice of adding certain fibers to construction materials dates back to the ancient times, more than 4,500 years ago. This reinforcing technique was applied to the most widely used structural material at that time, dried mud bricks. Ancient civilizations used straw, bamboo fibers or horse-hair to strengthen the bricks [206].

More recently, since concrete started to be used more extensively, engineers had to overcome deficiencies like brittleness, poor tensile strength, poor resistance to impact strength, fatigue, low ductility, etc [207]. Randomly distributed small fibers were added to concrete to solve some of these problems. The role of fibers are essentially to arrest any advancing cracks by applying punching forces at the crack tips, thus delaying their propagation across the matrix. However, addition of fibers possess certain problems regarding mixing and workability. They tend to form balls, which changes the properties of the composite [3, 125, 200].

Initially, asbestos fibers were widely used along the XX century. They were often mixed with cement and concrete due to its tensile strength and fire resistance. The use of asbestos fibers rose until it was heavily restricted in many countries owing to the hazard for public health. Consequently, new materials like steel, glass and synthetic fibers replaced asbestos as reinforcement [206].

In recent years, steel fibers are used in concrete to improve its performances. Steel fibers have been proven, mainly by empirical observations, to improve significantly the behavior of concrete beams and slabs by limiting the crack widths and by assuring a more favourable crack distribution. Promising research results allow also the consideration of using SFRC

in structural applications. However, the utilization of SFRC for structural purposes is quite limited mainly due to the lack of code for this material.

2.2 Constituents of fibers reinforced concrete

2.2.1 Fibers

There is a wide range of fibers to choose in the market, which can solve the brittleness of concrete. Although different treatments can be applied to them that would change their characteristics, they might be mainly classified by its material and size. In fact, no single fiber reinforced concrete has the perfect mechanical properties.

The main parameters that influenced the behavior of the composite are the material and size of the fibers, matrix-fiber interaction and fiber distribution and orientation [84, 129, 164, 194]. The following points describe the effects of fibers more deeply.

MATERIAL

As regards the material, steel fiber is the most commonly used type for most structural and non-structural purposes, but other materials as polypropylene and glass fibers are also used:

- **Steel fibers:** Concrete post cracking tensile resistance and toughness are improved by the addition of steel fibers [129]. Nevertheless, the use of SFRC has been very limited in buildings, even though steel fibers have been shown to enhance flexural and shear behavior of concrete [163]. The limited use of SFRC in building structures is primarily due to the lack of design codes and standards [49]. Mechanical properties of SFRC are closely related to the fibers properties, matrix strength and their interaction [84, 164, 194].

- **Synthetic fibers:** Polypropylene and nylon fibers are the most used material among the synthetic fibers. The presence of them has no significant effect on compressive strength of concrete. Nevertheless, they are effective to increase flexural strength and durability [4]. The main advantage is that they are chemically more inert than the other materials, which have opened the field to new applications where the corrosion of steel fibers might be an issue [4, 68]. However, the synthetic fibers are not able to borne high loads at small deformations due to its low modulus of elasticity and frictional adhesion with matrix [4].

- **Glass fibers:** Glass fibers increase the tensile resistance of concrete however the long-term durability is reduced because the alkalis of the cement affect the properties

of fibers [81]. As they do not replace the reinforcement, GFRC (Glass fiber reinforced concrete) are mainly used in fireplace environment, shells where loads are light and other similar elements [81]. The applicability of glass fibers in concrete is very limited because they lose strength due to abrasion and impact forces generated during the mixing [81].

FIBER SIZE (LENGTH AND DIAMETER)

Fracture process in concrete begins with microcracks in the intermediate zones around aggregates. While the tensile loading continues increasing, the microcracks grow and connect each other forming larger cracks.
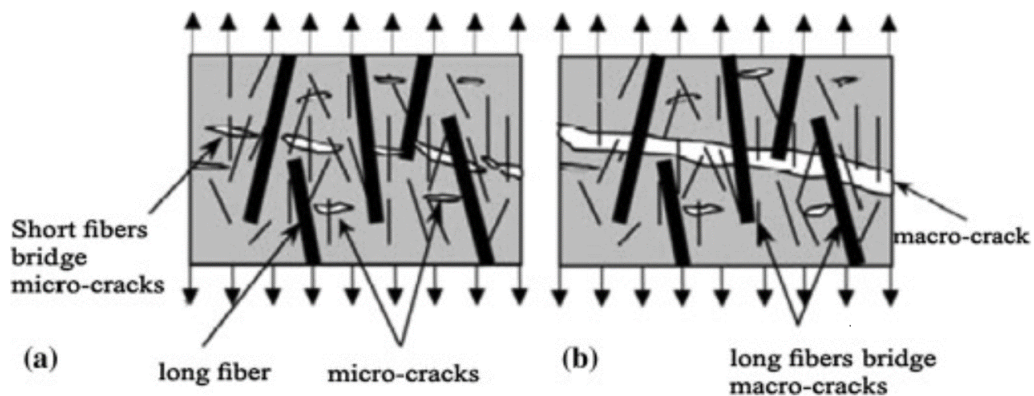
Fig. 2.1 Bridging effect of the fibers [129]

Short fibers would be the responsible for bridging the microcracks due to they are very thiner than greater fibers (see Figure 2.1). The short fibers would have significant influence on the increase of tensile strength at the beginning of the loading process. Nevertheless, short fibers will lose their effectiveness as the crack width increases, because they will be pulled out of the matrix. In contrast, the long fiber will be the responsible to control the macrocracking Figure 2.1. The combination of fibers is an optimal solution to increase the tensile strength and ductility [164].

Although combining large and short fibers seems to be a promising concept, Figure 2.2 suggest that small diameter fibers alone get better properties than the hybrid ones [19]. Therefore, further studies are needed to study this phenomenon. Overall, the values of diameters and length are between 0.15-0.8 mm and 10-75 mm, respectively.
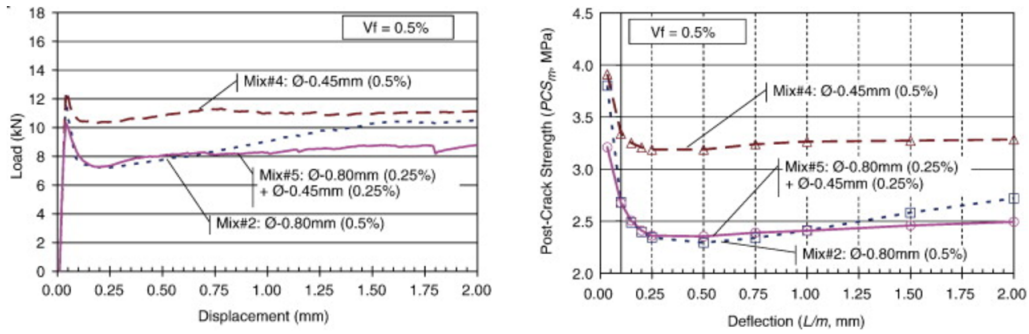
Fig. 2.2 Load-deflection curve and post-crack strength [19]

MATRIX-FIBER INTERACTION

Fiber-matrix interaction has to be ensured because it affects to the transferred force from the fibers to the matrix. An incorrect setting of fibers can pull off fibers from the matrix at low loads, which reduce the tensile strength. There are different types of steel fibers (straight, hooked, crimped, twisted...) depending on the commercial supplier as it is showed in Figure 2.3. Logically, fibers deformed at their ends allow better anchoring in concrete, but not many studies have carried out about the proper form of fibers [194].
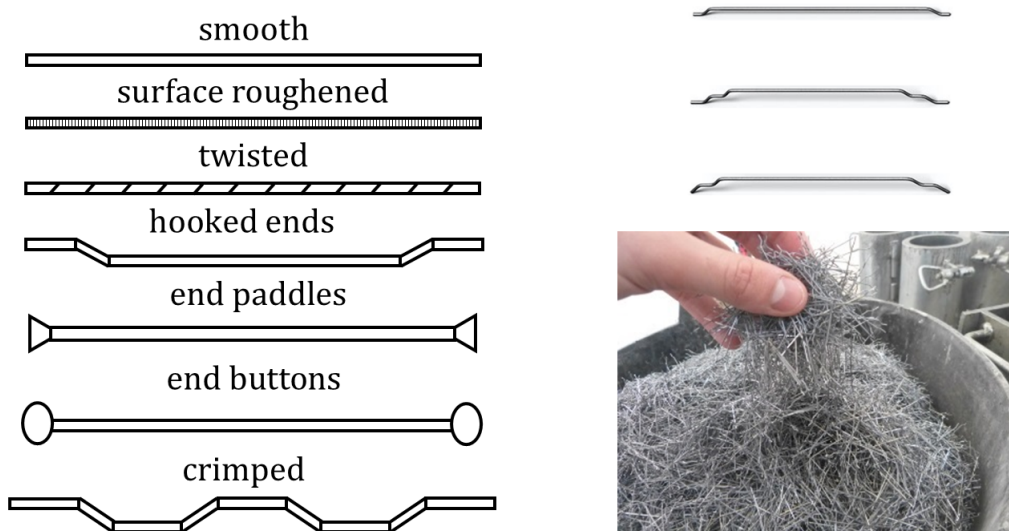
Fig. 2.3 Profiles of steel fibers used in concrete

FIBER DISTRIBUTION AND ORIENTATION

Another important facts to control are the distribution and orientation of fibers. Although an advantageous orientation of fibers is beneficial to reduce the cracking, generally, it is

assumed that fibers are uniformly and randomly distributed [84, 83, 163]. This allows the designers to assume an isotropic behavior [61]. In practice, fibers tend to align with the flow of the concreting except around the formwork as is showed in Figure 2.4. The frictional restraint orientates the fibers parallel to the wall [166].
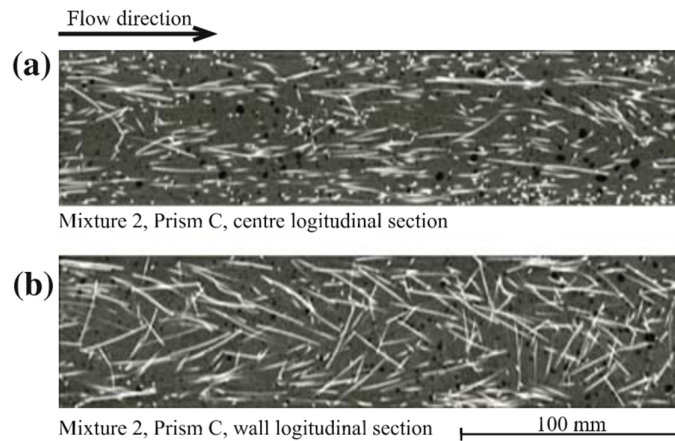
Fig. 2.4 Fiber orientation for different flow direction [166]

The effectiveness of the solution is reduced, if the fibers are not aligned in the stress direction. Many methods were studied to control the orientation of fibers in the past, such as the magnetic fields [173]. Most of them are limited to be applied in the laboratory [173]. Nevertheless, several researchers have highlighted the influence of the direction of the casting on the orientation of fibers [173, 166].

2.2.2 Concrete

Concrete is one of the most used man-made material in the world and this industry is increasing all over the world especially in the developing countries such as India and China. Although concrete production is difficult to track, it is reported that the annual concrete production in the world increased from more than 10 Gt in 2006 [106] to 32 Gt in 2017 [11]. Thus, by considering the size and the growing rate of the industry, it is necessary to produce sustainable materials. In order to fulfill this objective, factors such as energy savings techniques, increasing service life, reusability/recycling of materials need to be seriously considered in every stage.

Concrete is mainly composed of aggregates, cement, water and additives. Aggregate fraction in concrete is about 75% of its total volume and it plays a vital role in the overall performance of concrete. Therefore, the sustainability of concrete as material is strongly influenced by the aggregate. Regarding cement, the other main component, clinker manufacturing demands high amount of natural resources and energy. Furthermore, it generates a

large amount of CO_2, approximately 1 tone of CO_2 per clincker tone [21]. Water directly affects the workability and strength of concrete, apart from its durability. Workability is improved when water is added, however concrete strength is reduced. Water/cement ratio is one of the key parameters to get the desired properties in concrete. Lastly, additives modify characteristics of the hydratation to improve their properties and last performance.

In the following sections the role of the mentioned constituents are presented.

AGGREGATES

Currently, it is faced with an important consumption and a growing need for aggregates because of the growth in concrete production, this situation has led to a fast decrease of available resources. On the other hand, several industries has generated a considerable amount of solid disposal, which have a serious impact on the environment. The usage of waste bring about a practical end-of-life alternative for their lead in landfills. Therefore, it has become necessary to reuse these wastes as a substitute rather than natural aggregates in concrete production.

Among other origin, wastes can come from slag industry [151], tire rubber [168], plastic waste [172] or agro-based industry [95]. In this research Electric Arc Furnace Slag (EAFS) was used as aggregate, which are an industrial waste generated during steelmaking process.

Several studies proved that the use of EAFS in concrete as coarse aggregate has not undesirable consequences. Moreover, they can even improve its performance under long term (durability) and short term (mechanical properties) effects [151, 12, 59, 98, 135]. In the following points are summarized the main characteristics of concretes made by EAFS:

- **Compressive strength:** Concretes produced with EAFS obtained a higher compressive strength than conventional concrete due to a higher density of Interfacial Transition Zone (ITZ) [136, 151]. Unlike natural aggregates that have smooth faces, the slags generate stronger bond between cement and aggregates due to the porosity and roughness [136]. The porous nature of EAFS provide a strong interlocking effect. The higher stiffness and density of EAFS allow to attain mixtures with higher cohesion between aggregate and matrix leading to significant mechanical improvements.

- **Specific density:** The density of EAFS is higher than natural aggregates; consequently, the density of concrete might increase about 15% [151]. This downside is offset by the increasing in strength [12]. Its high density might be an advantageous property when weight of concrete is a key factor, such as in sea-walls, foundations and ballast.

- **Permeability and porosity:** The porous nature of EAFS provide a strong interlocking effect [151]. The water absorption of the steel slag aggregates concrete is lower than for crushed limestone aggregates, which contribute to impermeabilize the concrete [149].

- **Workability:** The specific density and water absorption capacity of slags are higher than for natural aggregates, factors that has to be taken into account in concrete mixture design [135]. This is not a significant problem to obtain the required workability of the mixture due to the possibility of using plasticizers and higher content of fines [145].

- **Durability:** The performance of EAFS concrete is similar to that of traditional concrete or even better [13, 98]. EAFS conglomerate tend to expand more than traditional ones when they are subjected to wetting and drying cycles [136]. Nevertheless, exposing to outdoors condition in advance might stabilize chemically and physically addressing the problem [136].

- **Environmental sustainability:** The use of EAFS as coarse aggregate in concrete mixes helps to maintain sustainability of the environment reducing the problems created by storage these materials. It is also a sustainable approach to preserving the need of new quarries.

In summary, the properties of EAFS concretes are not significantly different from natural aggregates concrete, although its particularities must have been considered. Using EAFS as aggregate is rising due to the promoted regulations aimed at fulfilling the environment requirements such as in the north of Spain (see *BOPV Nr 80 30th April, 2019*).

CEMENT

Cement influences concrete workability in the fresh stage, heat release ratio in the hydratation stage and stability in the hardened stage. The raw material used in the manufactured of cement consist mainly of lime, alumina, silica and iron oxide, which are obtained from calcareous, argillaceous, and argillocalcareous rocks. They are mixed on the basis of the properties required for concrete or mortar and heated up to $\pm 1.400°C$ to create the clinker. The typical physical requirements are expansion, strength, heat of hydration and setting time [207].

The European Standard UNE-EN 197-1 [181] defines different types of cements based on its composition (CEM-I, CEM-II, CEM-III, CEM-IV, and CEM-V). The following letter (A, B or C) specifies the clinker content. The remaining letters indicate the component used in addition to the clinker. Table 2.1 shows the composition of every type of cement according to [181].

- **CEM I: Portland cement.** Clinker is almost the only component. This cement is suitable for all general concrete application, it has not any special property. It is not resistant to sulphate and releases a large amount of heat during the hydration process.

- **CEM II: Portland-composite cement.** It is a mixture of ordinary Portland cement and supplementary cementing materials, which improve the performance of concrete.

  - **Blast-furnace slag:** It is a fine granulated slag obtained as a by product in the steel industry (blast furnace route). It is used as a replacement material for Portland cement, which reduce the production cost. The fineness reduce the permeability and increase the durability. The initial strength is less than the Portland cement, but the ultimate strength can be even higher [54].

  - **Silica fume:** Addition of silica fume, also known as microsilica, increases the strength and density of concrete. The increased density of the matrix reduces the permeability of concrete. It also becomes more sticky concrete, which improve the workability. However, silica fume increases water demand [87].

  - **Pozzolana:** Although natural and artificial pozzolanas are not cementitious materials in themselves, they contain compounds which combined with lime contribute to cementing properties. The strength of cement is lower than that of plain Portland cement at early ages, but can reach the same order of strength at longer curing periods.

  - **Fly ash:** The fly ash is a by-product from the combustion of coal. The benefits of fly ash include decreased permeability, and higher ultimate strengths. Fly ash fills the voids leading to reduction in pore connectivity. It also limits the early heat generation [50].

  - **Burnt shale:** The replacement of Portland cement by burnt shale does not only reduce its cost reduce and the compressive strength, it also contribute to improve its compressive strength. It posses limited cementitious value on itself, nevertheless, it is involved in the pozzolanic reactions [160, 24].

  - **Limestone powder:** The limestone cements indicate satisfactory strength and generally demand less water. It improves the clinker reactivity and the exploitation of its hydraulic potential. The Portland limestone cements indicate competitive concrete properties and improve the corrosion performance of concrete [175].

- **CEM III: Blast furnace cement.** They are cements with high proportion of furnace slags. It is used for works where economics considerations are predominant. It devel-

oped lower compressive strength at early ages, but equal or higher at later ages [128]. CEM III can be classified as a sulphate resistant and seawater resistant cement [71, 67].

- **CEM IV: Pozzolanic cement.** It has high resistance to chemical attacks compared with portland cement. It is widely used in marine environment, sewage works or in structures placed under water.

- **CEM V: Composite cement.** This cement consists of cement clinker with following additions: blast furnace slag, fly ash and natural pozzolan. However, the clinker is replaced by materials like fly ash, slag, limestone powder, natural pozzolanas, etc. to reduce the emissions of CO_2.

Main types	Notation of the 27 products (types of common cement)	Composition (percentage by mass [a])										Minor additional constituents
		Main constituents										
		Clinker	Blast-furnace slag	Silica fume	Pozzolana		Fly ash		Burnt shale	Limestone		
					natural	natural calcined	siliceous	calca-reous				
		K	S	D [b]	P	Q	V	W	T	L	LL	
CEM I	Portland cement — CEM I	95-100	–	–	–	–	–	–	–	–	–	0-5
CEM II	Portland-slag cement — CEM II/A-S	80-94	6-20	–	–	–	–	–	–	–	–	0-5
	Portland-slag cement — CEM II/B-S	65-79	21-35	–	–	–	–	–	–	–	–	0-5
	Portland-silica fume cement — CEM II/A-D	90-94	–	6-10	–	–	–	–	–	–	–	0-5
	Portland-pozzolana cement — CEM II/A-P	80-94	–	–	6-20	–	–	–	–	–	–	0-5
	Portland-pozzolana cement — CEM II/B-P	65-79	–	–	21-35	–	–	–	–	–	–	0-5
	Portland-pozzolana cement — CEM II/A-Q	80-94	–	–	–	6-20	–	–	–	–	–	0-5
	Portland-pozzolana cement — CEM II/B-Q	65-79	–	–	–	21-35	–	–	–	–	–	0-5
	Portland-fly ash cement — CEM II/A-V	80-94	–	–	–	–	6-20	–	–	–	–	0-5
	Portland-fly ash cement — CEM II/B-V	65-79	–	–	–	–	21-35	–	–	–	–	0-5
	Portland-fly ash cement — CEM II/A-W	80-94	–	–	–	–	–	6-20	–	–	–	0-5
	Portland-fly ash cement — CEM II/B-W	65-79	–	–	–	–	–	21-35	–	–	–	0-5
	Portland-burnt shale cement — CEM II/A-T	80-94	–	–	–	–	–	–	6-20	–	–	0-5
	Portland-burnt shale cement — CEM II/B-T	65-79	–	–	–	–	–	–	21-35	–	–	0-5
	Portland-limestone cement — CEM II/A-L	80-94	–	–	–	–	–	–	–	6-20	–	0-5
	Portland-limestone cement — CEM II/B-L	65-79	–	–	–	–	–	–	–	21-35	–	0-5
	Portland-limestone cement — CEM II/A-LL	80-94	–	–	–	–	–	–	–	–	6-20	0-5
	Portland-limestone cement — CEM II/B-LL	65-79	–	–	–	–	–	–	–	–	21-35	0-5
	Portland-composite cement [c] — CEM II/A-M	80-94	<------------------------------- 6-20 ------------------------------>									0-5
	Portland-composite cement [c] — CEM II/B-M	65-79	<------------------------------- 21-35 ------------------------------>									0-5
CEM III	Blastfurnace cement — CEM III/A	35-64	36-65	–	–	–	–	–	–	–	–	0-5
	Blastfurnace cement — CEM III/B	20-34	66-80	–	–	–	–	–	–	–	–	0-5
	Blastfurnace cement — CEM III/C	5-19	81-95	–	–	–	–	–	–	–	–	0-5
CEM IV	Pozzolanic cement [c] — CEM IV/A	65-89	–	<------------------- 11-35 ------------------->					–	–	–	0-5
	Pozzolanic cement [c] — CEM IV/B	45-64	–	<------------------- 36-55 ------------------->					–	–	–	0-5
CEM V	Composite cement [c] — CEM V/A	40-64	18-30	–	<-------- 18-30 -------->		18-30	–	–	–	–	0-5
	Composite cement [c] — CEM V/B	20-38	31-50	–	<-------- 31-50 -------->		31-50	–	–	–	–	0-5

a   The values in the table refer to the sum of the main and minor additional constituents.
b   The proportion of silica fume is limited to 10 %.
c   In Portland-composite cements CEM II/A-M and CEM II/B-M, in pozzolanic cements CEM IV/A and CEM IV/B and in composite cements CEM V/A and CEM V/B the main constituents other than clinker shall be declared by designation of the cement

Table 2.1 Main types of cements [181]

WATER/CEMENT RATIO

One of the most influencing factor is the water/cement ratio (w/c). These two ingredients are responsible for binding everything together. Historically in civil engineering, Abram's cone has been used to describe the dependence of concrete strength on w/c ratio. The law states the strength of a concrete mix is inversely related to the mass ratio of water to cement [155, 196, 141].

   Great amount of water reduce the consistency of the mix and enlarge the spacing of the cement particles. This means the cement paste is more diluted and it influences to the most of the properties of concrete, such as strength, porosity and permeability [69, 117]. In the following points are analyzed the main properties that are affected by the w/c ratio:

- **Hardened properties:** Mechanical properties decreased with the increase of w/c ratio according to *Haach et al.* [69]. Despite the reduction is very limited, mixtures with high w/c ratios respond less rigidly. They presents lower values of the elastic modulus [63, 204]. The increase in the w/c ratio also means that compressive strength decreases due to the increase in the porosity [204, 69, 80]. Similarly to the relation between compressive strength and w/c ratio, flexural strength decreased with the increasing of w/c ratio [141].

- **Fracture behavior:** The w/c ratio changes the strain/stress curve. The slope of the stress/strain curve after peak value is steeper for low w/c ratio than that for high w/c ratio mortar. This affects directly to the ductility and toughness of the material. Therefore, low w/c ratio mortar shows more brittle behavior than high w/c ratio mortar [204, 141].

- **Durability:** Durability is strongly associated with the internal structure of concrete. The increase in the w/c ratio means that there is more water between the solid particles and consequently there are more voids [69]. Permeability is one of the parameters used to evaluate the porosity of concrete. Water flow increases with increase in w/c ratio due to change in pore structure [205, 80].

   In conclusion, a low w/c ratio leads to a stronger and more durable concrete. However, the w/c reduction is limited by workability and the amount of water required for hydratation of cement particles [69].

ADMIXTURES

Admixtures are added mainly for the purpose of modifying setting conditions and reducing water requirements. Nowadays concrete contain one or more admixtures to meet the requirements for fresh and hardened concrete.

- **Air-entraining admixtures:** It causes small bubbles of air to form uniformly distributed through concrete. It is used to design concrete to resist freezing/thawing and wetting/drying cycles. These increases the durability of the mixture.

- **Water-reducing admixtures:** They are called plasticizer or superplasticizers depending on the water reducing range. The effect of this polymers are 1) a repulsive force which overcomes the flocculation tendency of cement 2) retarding the hydratation process creating a layer around cement particles. Therefore, the fluidity of concrete increase without adding water and the setting time is retarded. Workability is increased while at the same time maintaining strength. However, it causes more bleeding and more air is entrained [151, 207]. This admixtures enables the casting of structures with complex shape or heavily reinforced because it is consolidated by its own gravity, without any external vibration.

- **Retarding admixtures:** Retarding admixtures are used to delay the hydration of cement and extend the setting time of concrete. These types of concrete admixtures are commonly used to reduce the effect of high temperatures and keep concrete workable throughout the placing of large structure [87].

- **Accelerating admixtures:** Accelerating concrete admixtures are used to increase the rate of concrete strength development or to reduce concrete setting time. They are usually used in cold climate zones and precast industry. The main disadvantage of this additive is that induces corrosion due to the using of chlorides [119].

- **Shrinkage-reducing admixtures:** This type of admixture can reduce drying shrinkage and restrained shrinkage cracking. Nevertheless, early strengths might be reduced [57].

2.3   Mechanical properties of the SFRC

The addition of fibers reduces the formation and development of cracks and provides a post-cracking loading capacity. The ductility and toughness are improved significantly [174], however the compressive behavior is slightly affected [31]. A quick overview of the properties of the SFRC is presented in the following points.

2.3.1   Tensile behavior

The tensile resistance of the cement based materials is insignificant and it is usually dismissed. Many traditional designers and authorities are reluctant to consider this property and reduce the reinforcement [82]. However, one of the main advantages provided by the steel fibers is the improvement of the tensile behavior, which should be considered to make the most of its capacities.

The precracking behavior is governed by matrix properties and on the contrary, the steel fibers changes the cracking phase. The steel fibers bridge the cracks and the stresses are transferred to the fiber. The stresses in the fiber increase while the loading increased. The failure usually occurs due to the pull-out of the fiber and not because of the exhaustion of the steel [165]. The properties and the amount of steel fibers will change the postcracking behavior of SFRC Figure 2.5.
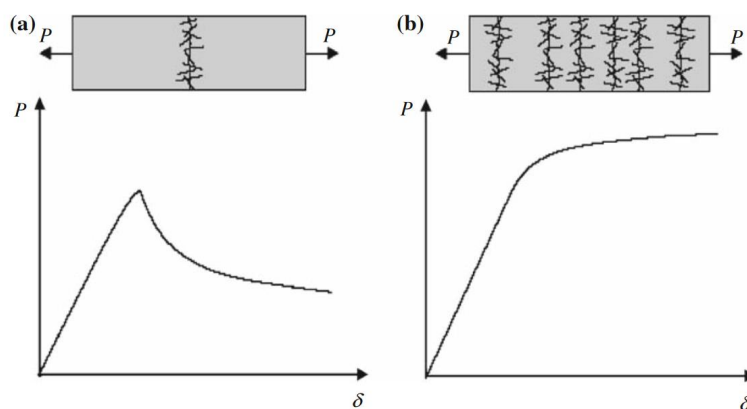
Fig. 2.5 Loading-deformation curve for post-cracking (a) softening and (b) hardening [47]

The postcracking behavior in uniaxial tensile is governed by the steel fibers, which provides a mean to transfer stresses across cracks. SFRC has a softening behavior, even though it can be extended to hardening by improving the matrix properties and increasing the fiber content [47]. Therefore, the tensile behavior has strong dependency on fiber volume fraction and bond behavior between fibers and matrix [194]. Increasing the amount of fibers smeared the damage along the element promoting a multicracking and hardening behavior. Figure 2.6 shows the behavior of SFRC in tension, where can be differenced three ranges:

1. **Linear-elastic part**

   The maximum stress attained in this regime coincided with the tensile strength of the matrix and it was observed that the first cracking stress is slightly influenced by the presence of fibers [22]. The major part of maximum tensile strength was achieved in

this regime, but with a very small part of corresponding deformation. During the elastic regime the weakest part of the composite, concrete, began to break into microcracks. However, it might be continued considering as linear-elastic, with the modulus of elasticity corresponding to the initial modulus of elasticity in compression [194].

The end of the elastic regime corresponded to a fictitious point of transition from ideal linear elastic to strain hardening behavior. Depending on the amount of fibers, the hardening part may disappear moving directly to the softening phase [194]. In this particular case, a sharp drop in the stress value occurred.

2. **Strain hardening part**

At the beginning of this phase as the crack-width is usually fine and a composite behavior still exists. However, concrete effect quickly vanishes with the increase of deformations, while the fibers begin to acquire a more relevant role. The main function of the fibers is sewing the cracks, which might change the brittle behavior of concrete [194]. The brittleness is reduced as the fiber dosage increase because the damage is distributed along the element (multiple-cracking) while the mixture could even achieve greater strengths. In such case, concrete exhibits hardening behavior after the peak.

This continuous microcracking process resembled a plastic or strain hardening behavior. Owing to the fact that no true plastic microstructural changes take place, a term "pseudo strain hardening" or "pseudo plastic" is often used to describe this behavior. Therefore, the hardening behavior is due to the high quantity of fibers accompanied by multicrack damage mode [194].

3. **Strain softening part**

The end of strain hardening phase coincides with the moment when the transfer of the stress cannot longer be assured. This can be expressed as the moment when the strain hardening capacity of the material is exhausted.

In this phase the cracks are well defined and the fibers are the responsible to resist the opening. The fibers are randomly oriented within concrete and consequently they do not contribute to the strength in the same way. As the anchorage level is different for every fiber, with increasing crack opening most fibers are pulled out or got exhausted. Therefore, the residual tensile strength exhibits a progressive decreasing while the deformation capacity was more pronounced. At this stage, the behavior is so nonlinear and it is linked with the fracture energy (stored energy) [194].
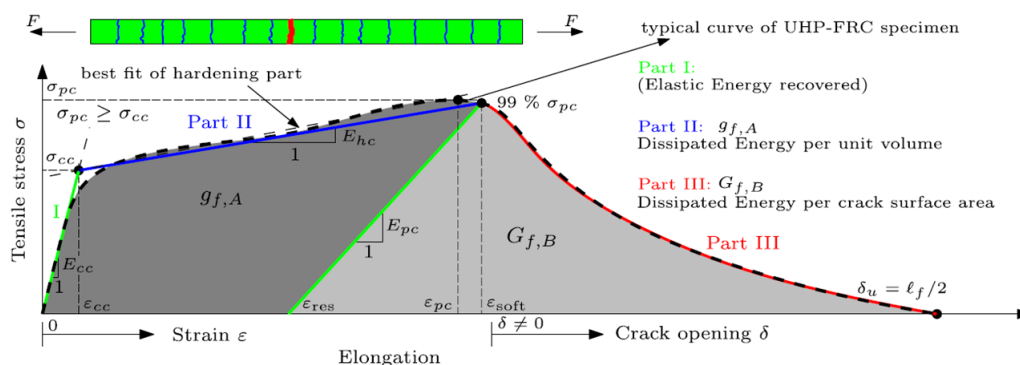
Fig. 2.6 Uniaxial tensile response of SFRC [194]

2.3.2 Compressive strength

The addition of steel fibers has little effect on compressive strength [31]. As it has been mentioned before, the steel fiber would affect mainly to properties regarding to the tensile strength and ductility. Therefore, the ascending and descending part of the stress-strain curve are affected as it is illustrated in Figure 2.7, especially, the descending part after the peak [191]. This concept is closely related to the toughness and ductility.
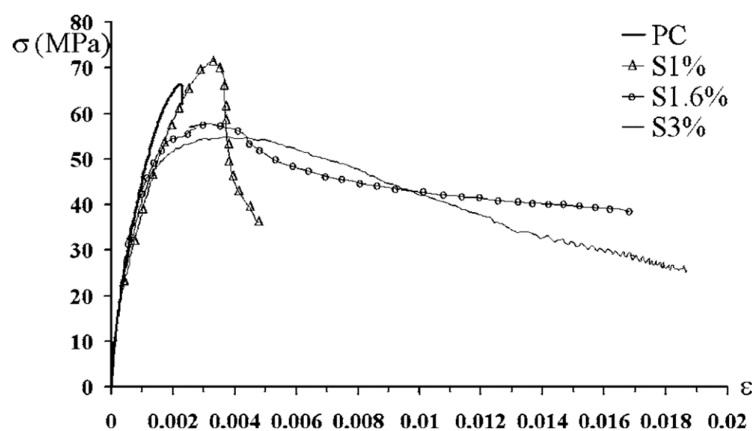
Fig. 2.7 Stress-strain curve for specimens without (PC) and with fibers (S1%, S1.6%, S3%) [31]

The rapid development in concrete technology has made it possible to increase the strength of concrete, which also increases the brittleness. With the goal of making the best of the capacities of concrete, adding fibers is a possibility that can reduce this problem. Therefore, although fibers do not increase directly the compressive strength, it can be considered that indirectly they would help to improve the compressive behavior.

2.3.3   Shear strength

Shear capacity is traditionally enhanced by the stirrups. Space limitations and changes of the loading state may make difficult to place the required reinforcing. For this reason, several studies [42, 90, 99] have been carried out to analyses the use of steel fibers as substitute of traditional reinforcement. It has been established that, depending on the shape and quantity, they can increase the shear strength of concrete beams as it is showed in Figure 2.8. The main advantages over stirrups are [99]:

- Fibers are distributed randomly through the element and provide equal resistance in all direction.

- Fibers increase the first crack tensile strength and the ultimate tensile strength, which enabled the beam to develop the full shear strength.

- The shear-friction strength is increased by the bridging phenomenon.
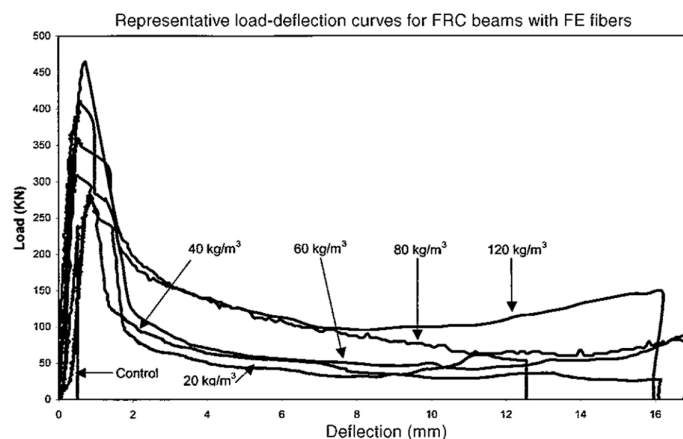
Fig. 2.8 Load-deflection curve in shear for fiber reinforced concrete [109]

There are many studies that confirm the improvements of fibers as shear reinforcements, even going so far as to propose the replacing of part of the reinforcement [82]. Some studies, such as in the study of *Li et al.* [90], conclude that the shear strength increases in the range of 100-200%. Other studies also noted that at least 1% of fiber is needed to avoid shear failure and change the mode of failure from shear to flexure [91]. Although structural test shows the effectiveness of fiber reinforcement on exposure to shear stresses [85], the design codes still does not implement these improvements.

2.3.4 Flexural strength

The flexural strength is directly related to the tensile strength. As the fiber reinforced greatly increases the tensile capacity, it is usually employed to increase the flexural capacity [197]. The flexural strength and deflection increased with fiber content because ductile behavior of SFRC on the tension side of a beam alters the normally elastic distribution of stress and strain over the member depth Figure 2.9. Moreover, the addition of steel fibers reduces the amount of cracks at the same applied load, due to the bridging effect. Above the cracking load, the cracks reduce the tensile stress carried by concrete, transmitting the loads to the reinforcement. The degree of cracking define the moment of inertia, which will change from a maximum value (uncracked section) to a minimum value (fully cracked section) [148].
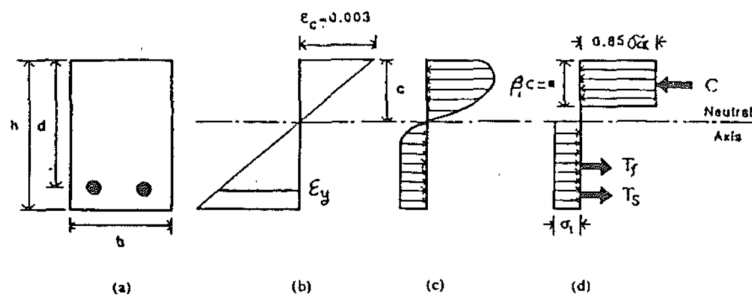
Fig. 2.9 Strain-stress distribution of SFRC beam [121]

Therefore, an increment of fiber content produces an increase in ductility and flexural strength. It should be noted that, the increase in flexural strength is much significant at lower fiber volume concentrations than for higher fiber density [55].

2.3.5 Impact loading

Stress waves, which transport energy in every direction, are produced when a projectile strikes the plate. The increase in the stress generates perpendicular cracks to the direction of propagation, leading to tensile rupture. Therefore, being consequent with what has been explained in the previous sections, the SFRC element will exhibit superior performances compared with nonfibrous mixtures [73].

The two most important properties to characterize the behavior under impact loading are the strength and the fracture energy of the SFRC. Fibers improve the impact energy absorption, which depends on the type of added fibers [73, 18]. Nevertheless, the strength of the matrix plays a stronger role in improving fracture energy than does just the fibers. The improvement is considerably smaller than that obtained in static loading, due to fiber failure [18].

Experimental results show that the major advantage is the reduction of scabbing, fragmentation, spalling and the damage area, due to the increase in toughness tensile strength [93]. Although fibers do not reduce the penetration depth of the projectile, it is a viable alternative because it enables the use of thinner plate [93].

2.3.6   Fatigue behavior

The repeating loads, although they are smaller than the static failure load, induce microcracks that cause reinforced members to fail abruptly as it is shown in Figure 2.10. Cracks are opened in the compressive part when the most compressed fiber of concrete is degraded, due to the fatigue stresses. The lever arm is reduced because of the cracking and the stresses are redistributed. The new stress state increases the tensile loads upon the reinforcement bar and it would fail because of brittle fracture of the steel reinforcing bar [134].
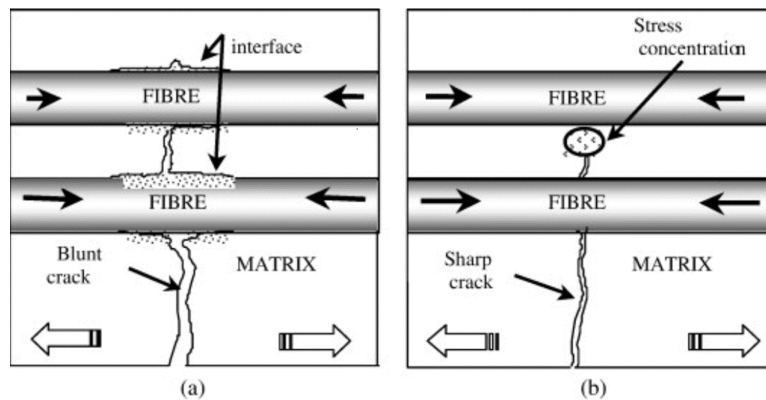
Fig. 2.10 Cracking appearance in presence of fibers: a) during static loading following a stage of fatigue loading, b) during static loading without previous fatigue loading [146]

Fibers reduce the stress concentrations in the bar because they stitch the cracks and delay the propagation. Therefore, there is a significant increase in ductility with increasing fiber content and they are more efficient in dynamic than in static condition. The cracking during the cyclic loading is defined by the loading rate and properties of the material. The matrix strength and matrix/fiber iteration define the fatigue strength, the latter being more critical aspect. In order to understand the phenomenon, Figure 2.11 shows the evolution of the different stages [146]:

1. **Development of microcracking**

   At this stage the rigidity of the composite material is reduced due to the matrix and matrix/fiber interface damage. The creation of new microcracks are stabilized but the
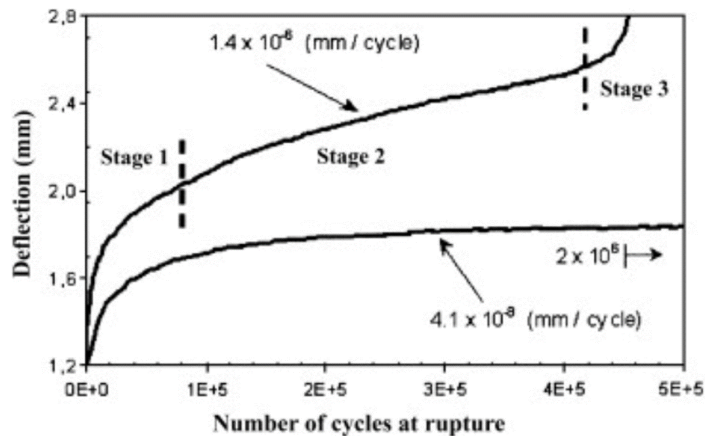
Fig. 2.11 Evolution of deflection with number of cycles [146]

fiber/matrix interface continues loading and damaging. The microcracking induces a
rapid increase in the deflection [146].

2. **Propagation of some microcracking**

   In this second stage, the deflection increase slowly and lineally. The bridging effect of
   the fibers stabilizes the opening of cracks during fatigue cycles. However, new cracks
   are generated and the fiber/matrix interface continues damaging gradually.

3. **Development of macrocracking**

   Fiber/matrix interface has been degrading gradually up to reach a significant damage
   level. Hence, the crack begins to open quickly, causing the brittle rupture of the
   element.

2.3.7   Durability

Durability is one of the most advantageous properties of concrete. Nevertheless, the corrosion
of reinforcement, the most common degradation phenomenon of reinforced concrete struc-
tures, may affect the integrity and reduce the life cycle of the structure [64]. The principal
effects are:

1. Reduction of the section of the bars and fibers.

2. Damaging concrete surrounding the reinforcement due to the expansion of the oxides.

3. Impairment of the bond between the reinforcement and concrete.

Uncracked concrete specimens are largely unaffected by corrosion, however once cracks are formed it can degrade the long-term performance. In this context, steel fibers are presented as a crack controller solution [188]. Fibers stitch the cracks shortening the depth and reducing the width of the crack. Therefore, the use of fibers reduce the permeability and the exposure of concrete. Moreover, the corrosion of steel fibers is less severe compared with bar reinforcement, due to large surface area/volume ratio [142]. The generated expansive forces due to the increase in volume produced by the oxidation, are not enough to split the surrounding concrete.

Although determining a universal crack width is difficult, cracks width thinner than about 0.1 mm has a negligible influence on durability [64]. Instead, the corrosion decreases with the distance from the crack face. The carbonation starts at concrete surface and continues inwards, as long as there is enough carbon dioxide available [44]. In this area, fibers lose the passivation of concrete and show signs of corrosion. Excluding this rim, light corrosion of the fibers may see but would not affect its mechanical properties [15, 64].

In conclusion, SFRC durability is superior to the conventional reinforced concrete even where steel fibers are used as reinforcement [64]. The small volume of fiber is insufficient to damage concrete as occurs to large diameter bar reinforcement and the corrosion is restricted to the surface of concrete. Moreover, some authors suggest that the flexural resistance increase after the corrosion process [64]. Thus, the corrosion phenomena is minimized by the addition of fibers but the porosity of concrete continues having the dominating effect [15].

2.3.8 Toughness

The toughness is recognized as the most distinguishes characteristic from normal concrete. It may be defined as the area enclosed by the stress-strain curve and sometimes it is also defined as the total energy of fracture. Figure 2.12 shows the difference in the area enclosed by mixtures with and without fibers. Analyzing the enclosed areas, toughness depends on the first crack load, ultimate load and deflection [3].

Fibers are added primarily to improve toughness or energy absorption capacity. Steel fibers induce crack-bridging effect that delays crack formation and provide energy absorption mechanism, related to the pull-out processes of the fibers. SFRC can carry significant stresses over a large strain capacity in the post-cracking stage. However, the stress-strain curves can vary for different types and volumes of steel fibers [74]. For example, fibers with better bond characteristics give higher toughness than straight fibers at the same volume concentrations [174]. As well, low fiber volume mixes exhibit strain softening behavior beyond the peak load and have lower toughness than mixes with high fiber volume [113].

	Peak Load kN	Deflection at First-Crack (mm)	Energy at 2mm (N-m)
Plain	23.96	.0328	0.44
F1	23.33	.0412	34.10
F2	22.38	.0386	21.48
F3	23.06	.0381	17.57
F4	23.37	.0362	26.68
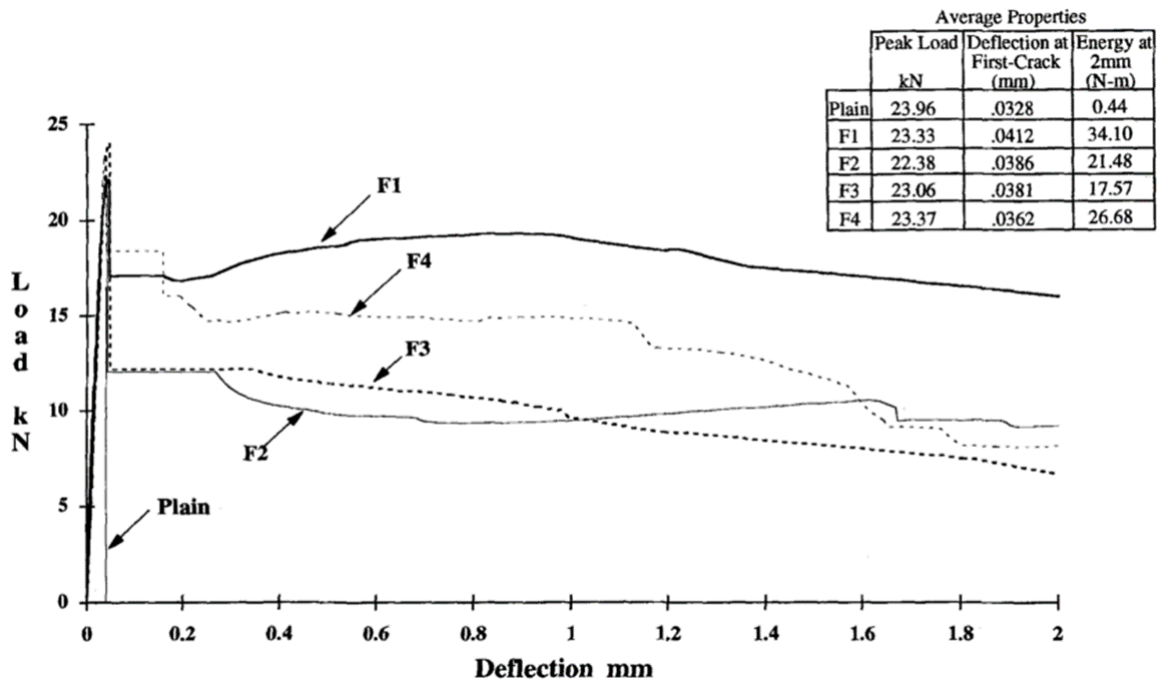
Fig. 2.12 Flexural load-deflections curves for plain concrete (PC), hooked end (F1), crimped (F2, F3) and twin cone (F4) fiber [174]

2.4   Applications of fibers reinforced concrete

The enhanced properties of concrete opens up new possibilities for engineers. The main advantages are the superior ductility, energy-absorbing characteristics, abrasion resistance and fatigue strength. SFRC is initially used as pavements in heavy-duty and container floors and airport runways due to savings in cost and superior performance during service. However, the growing confidence and experience has led to many new applications in precast, cast in-situ and shotcrete concrete.

Some investigations have indicated that steel fibers can be used instead of stirrups and even as supplementary shear reinforcement [82]. Steel fiber reinforcement can also be added to critical end zones of precast concrete beams and columns and in cast-in-place concrete to eliminate much of the secondary reinforcement. SFRC may also be an improved means of providing ductility to blast-resistant and seismic-resistant structures especially at their joints, owing to the ability of the fibers to resist deformation and undergo large rotations by permitting the development of plastic hinges under over-load conditions. In the following points are illustrated some applications of SFRC.

PAVEMENTS

Steel fibers have been used for a long time in construction of roads and also in floorings, particularly where heavy wear and tear is expected (ports, airports, industrial buildings...). Steel fiber reinforcement has been increasingly used in partial or total substitution of conventional reinforcement for concrete industrial pavements because steel fibers not only improve the flexural strength and the impact and fatigue resistance of concrete but also reduce shrinkage cracking. Furthermore, fibers provide a correct positioning of the reinforcement replacing the welded mesh [27]. These properties facilitate concrete casting and the durability of the pavements. Fibers would improve slightly the ultimate load but enhance remarkably the slab ductility [161].

There are studies that compare slabs reinforced with conventional reinforcement and SFRC [163]. Slabs reinforced with welded mesh exhibits higher peak loads because the greatest tensile stresses are at the bottom side of the slab, where the reinforcement is located. However, the tensile stresses are also present on the top surface, where often there are not reinforcing rebars. The uniform distribution of fibers solves this problem, preventing the formation of cracking through the whole volume. Some studies conclude that the fiber redistributes the stresses once the first crack appears. Therefore, the load can further increase until the collapse occurs due to fiber bridging. Another important conclusion is that along the external borders additional conventional reinforcement can be required for pavements [163].

BRIDGES

The brittle failure mode should be inhibited to improve the performance of bridges. In that way, they can remain a residual strength and be repaired. SFRC components present higher sectional capacity compared with plain concrete, due to the greater deformation capacity and they usually change the failure way, from shear failure into bending failure. Using fibers as reinforcement is being investigated as effective solution for high strain rate applications [139], such as earthquakes. Steel fiber is one of the most widely used reinforcements to improve mainly the performance of bridge piles [130, 202].

- **Decks:** The high ductility becomes SFRC a competitive alternative to build slabs [113, 105]. In areas where soil-structure interaction may create differential settlement, it may be a suitable solution [110]. It can be also used as an overlay of the primary structural support. Durability is an important aspect to be considered by the infrastructure managers. Deck cracking reduces chemical resistance of the structure. This negative aspect is critical in regions where salt is used to melt the snow. SFRC enables a reduced amount of conventional reinforcement, which is susceptible to be damaged by

corrosion [64]. The replacement of the reinforcement allow also to reduce the weight and the thickness of the deck [104, 88].

- **Piers:** Steel fibers are used to improve the brittle behavior of the piers. The addition of steel fibers also improves significantly shear strength and changes failure mechanism [85]. Fibers provide higher confining effect, which reduce the tensile strain and the spalling of concrete [60]. The cracking is distributed more uniformly, increasing the capacity to dissipate energy [60]. Therefore, the use of steel fibers allows higher stirrup spacing than the specimens reinforced with rebars [203].

WINDMILLS

The foundation and tower structures of offshore wind turbines that are installed to date are predominantly made of steel [140]. One of the advantages of steel structures is the relatively low weight while having a high stiffness. However, disadvantageous are the high fabrication costs of the steel segments and costly corrosion protection as. An economically promising alternative to tower structures made of steel is fiber reinforced concrete [140].

Production of taller, larger in diameter and more slender structural elements for the upcoming generations of the offshore wind turbines requires such material properties as high strength, durability, low maintenance, fatigue resistance, avoidance of resonance problems and resistance to the aggressive environmental impacts. In this respect, concrete has shown a promising potential and numerous benefits as a high performance structural material to be used offshore [78]. Owing the exceptional challenging aggressive environmental conditions existing offshore [122] and extra loads from combined wind, wave and current action, careful consideration should be given to alternative concrete mix designs.

SHOTCRETE COVERINGS

The residual strength and energy absorption capacity of fiber reinforced concrete make it really useful for sprayed concrete. It is widely used in lining of tunnels due to its energy absorption capacity when geological incidents occurs.

Although plain concrete provide also an acceptable support, SFRC provides much strength and, especially, toughness [42]. Another interesting point is the durability of this material in corrosion environments, which make it particularly attractive for applied in tunnelling industry [1]. Shotcrete reinforced with fibers represents a competitive material for use in ground stabilization.

Chapter 3

Mathematical overview

3.1 Introduction

The aim of this chapter is to introduce the formulation and governing equations used in FEM to model fracture. Firstly, a brief introduction about fracture mechanics is done and the fundamentals of the selected method (interface elements) are explained. A review of FEM is presented where the static equilibrium is analyzed. Lastly, the applied damage models are described.

3.2 Fracture mechanics of brittle materials

Crack prediction and their growth-path is important to determine the safety level of a structure. Fracture mechanics is the study of cracked solids subjected to an applied load. A solid exhibits discontinuities when the elastic range is exceeded. The formation of cracks may be a complex phenomena which depends on the microstructure of the solid, applied loading and other boundary conditions. For instance, concrete is a brittle material therefore, the crack velocity is high and little plastic strain may be involved before failure. By contrast, steel shows a ductile behavior which dissipated a large amount of energy and it is strongly deformed before failure. The literature treats three types of cracks from an engineering point of view and they are termed as mode I, II, and III [157]. They present three different cracking behavior a) Opening or tension mode b) Sliding mode c) Tearing mode and they are illustrated in Figure 3.1.

From the mechanical point of view, the discontinuities can be characterized as jumps in the displacement field (strong discontinuity) or in the strain field (weak discontinuities). The

(a) Mode I   (b) Mode II   (c) Mode III
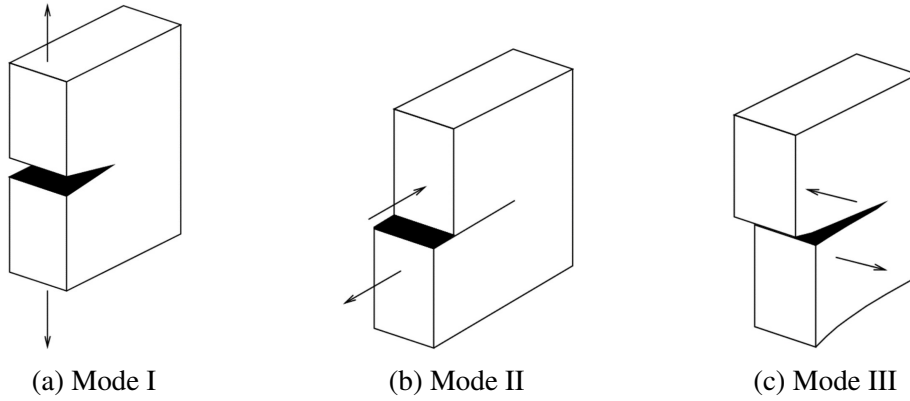
Fig. 3.1 Fracture modes for crack propagation

main difficulty arises in the determination of crack path, their kinking and splitting during their propagation.

The theory of elasticity does not define completely the singularities near crack tips. The presence of cracks can modify the local stress distribution becoming the elastic analysis insufficient. It is necessary to use principles of fracture mechanics to predict failure of solids containing cracks. There are available a large number of algorithms for modeling cracks in quasi-brittle materials. Each of them have their own limitations and advantages. Although interface elements are used to model fracture in this dissertation, XFEM and phase-field method are briefly presented in the following points.

3.2.1   Extended Finite Elements Method (XFEM)

The classical FEM approaches are computationally expensive for problems with rough discontinuities. A very fine mesh or a remeshing is required in regions where cracks are developed. Nevertheless, the XFEM overcomes this weakness allowing the developments of cracks within the element. In consequence, the mesh does not have to be conformed to the crack path, it is independent of the discontinuity, as is illustrated in Figure 3.2. This reduces the computational time and error associated with geometry mapping [169].

The numerical solution is approximated via a linear combination of functions, as the standard FEM, enriching the nodes around the tip of the crack with discontinuous functions. The enriched approximation for fracture mechanics is written in general form as [28]:

$$\hat{u}(x) = \sum_{i=0}^{N} N_i(x)u_i + \sum_{j=0}^{N_c} N_j(x)H(x)a_j + \sum_{k=0}^{N_f} N_k(x)\left(\sum_{\alpha=1}^{4} B_\alpha(x)b_k^\alpha\right) \tag{3.1}$$
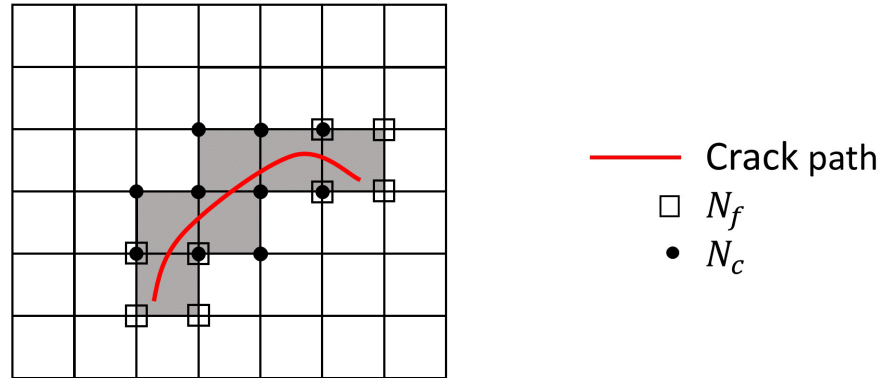
Fig. 3.2 Finite elements with discontinuities no aligned with a mesh

where a_j and b_k are nodal degrees of freedom corresponding to te Heavised function H(x) and the near tip functions, B_α. Nodes in set N_c are such that there support is split by the crack and nodes in set N_f belong to the elements that contain a crack tip.

The first term represent the classical finite element approximation, whereas the other terms represents the addition of a discontinuous enrichment. The enriched nodes are the ones that support is cut by the crack into two disjoint pieces (N_c and N_f). The second term represents the discontinuous jump of those elements which are completely cut by the crack through the Heaviside function. The third term introduce the asymptotic tip function which is applied to the nodes belonging to the element where the tips are.

Thus, XFEM has a great potential for many interested problems in the mechanics of materials [30, 92]. Deeper explanations and many applications are shown in [28, 169, 111, 51, 43, 162, 169].

3.2.2   Phase-field method

Fracture mechanics for quasi-brittle material is based on the work of *Griffith* [66], which enables to predict crack initiation, curvilinear cracks or crack kinking. These constraints are overcame by variational methods based on energy minimization [58]. This method is based on the fact that every point of the material has characteristic feature (toughness or energy to create a crack) that when it is exceeded propagation will take place. The crack path is defined minimizing the energetic state of all the possibilities or keeping the track of the previous step, when it is difficult to minimize.

The concept of Γ-convergence is applied to seek convergence of two fields: displacements and damage parameter [9, 156]. The damage parameter takes values from 0 to 1. The value 0 are in the crack and 1 in the boundary of the damage zone. The approximation regularizes a sharp crack by diffusive crack zones governed by the mentioned scalar parameter.

The variational-based phase-field approaches to fracture offer important new perspectives toward the theoretical and computational modeling of complex crack topologies. The method has been extended to capture complex features such as ductile fracture [6, 8], dynamic loading [32, 34], fracture in shells [7], nucleation [118], etc.

3.2.3   Interface finite element method

Interface elements are a simple tool to represent the fracture of brittle materials. Using standard elements made it easy to implement in any FEM code, which is one of the relevant point of this technique. The introduction of elements with very high aspect ratio to model concrete fracture was studied by *O.L. Manzoli et al* [100, 101].
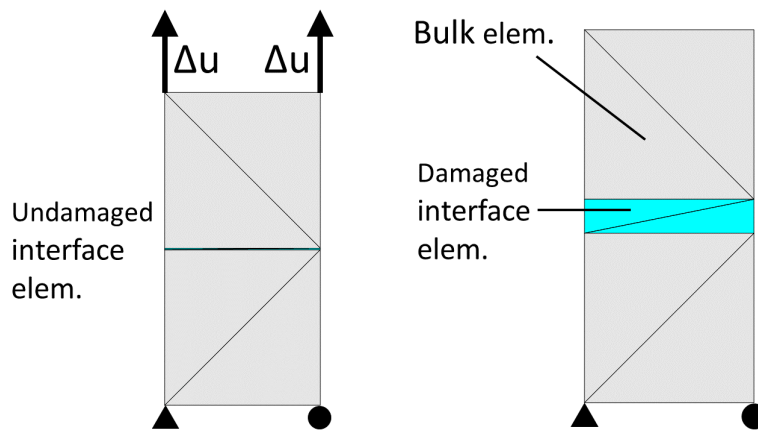
Fig. 3.3 Schematic diagram of interface elements model

The solid is discretized into finite elements including interface elements along the main potential crack paths as is shown in Figure 3.3. Therefore, the solid is idealized as a two-phase composite: bulk elements and interface elements. Bulk elements might be considered as elastic elements and interface elements behavior is governed by a softening law, which represents non-linear fracture. Therefore, crack opening is simulated by the degradation of interface elements. The damaged level of the elements is defined by a scalar value as in phase-field method.

Figure 3.4 shows the geometrical definitions of interface elements in 3D and 2D cases. As in this dissertation 2D modeling is applied, three node triangular element is considered to explain the mathemati fundamentals of the method. The triangular element is geometrically defined by the nodal coordinates, which are used to calculate the normal vector to the base, $\bar{n}$ and the height of the element.

Once the geometry is defined, the strain tensor ε is known based on the displacement field. The strain tensor can be discomposed into two tensors: $\tilde{\varepsilon}$ considers the strain values
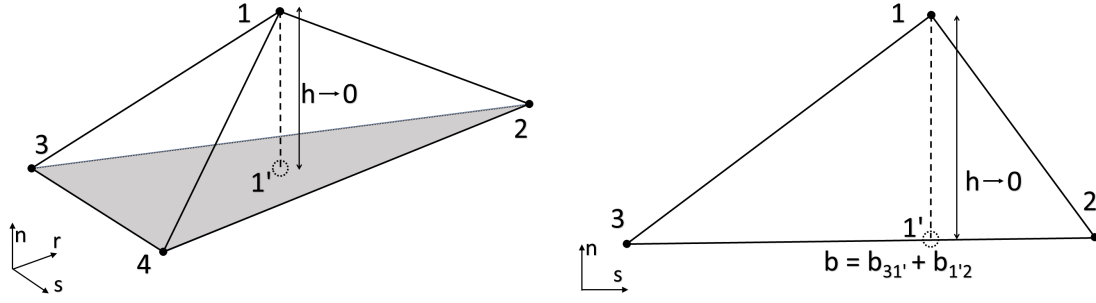
Fig. 3.4 3D and 2D interface element

depending on the height of the triangle and $\hat{\varepsilon}$ considers the strain values depending on the base of the triangle.

$$\varepsilon = \tilde{\varepsilon} + \hat{\varepsilon} \tag{3.2}$$

$$\tilde{\varepsilon} = \frac{1}{h} \begin{bmatrix} [\![u]\!]_n & \frac{1}{2}[\![u]\!]_s \\ \frac{1}{2}[\![u]\!]_s & 0 \end{bmatrix} \tag{3.3}$$

$$\hat{\varepsilon} = \frac{1}{b} \begin{bmatrix} 0 & \frac{1}{2}(u_n^{(2)} - u_n^{(3)}) \\ \frac{1}{2}(u_n^{(2)} - u_n^{(3)}) & u_s^{(2)} - u_s^{(3)} \end{bmatrix} \tag{3.4}$$

where u_n and u_s are the nodal displacements and $[\![u]\!]_s$ and $[\![u]\!]_n$ are the relative displacements between point (1) and its projection (1').

$$[\![u]\!]_s = u_s^{(1)} - u_s^{(1')} = u_s^{(1)} - \left[\frac{b_{31'}}{b} + \left(1 - \frac{b_{31'}}{b}\right)u_s^{(2)}\right] \tag{3.5}$$

$$[\![u]\!]_n = u_n^{(1)} - u_n^{(1')} = u_n^{(1)} - \left[\frac{b_{31'}}{b} + \left(1 - \frac{b_{31'}}{b}\right)u_n^{(2)}\right] \tag{3.6}$$

Interface elements can either be zero thickness with overlapping nodes or have a very small thickness ($h \to 0$). This condition indicates that $\tilde{\varepsilon}$ tends to infinite (unbounded), as might be deduced in Equation 3.3. Therefore, the strains are almost dependent on $\tilde{\varepsilon}$. The kinematics of the solution is conditioned mainly by the relative displacements between the node 1 and its projection 1' [101, 100]. Then, the corresponding stresses can be calculated by constitutive models despite the strain tensor is unbounded. The constitutive models are explained in the following chapter.

3.3   Mathematical formulation

The FEM formulation is introduced in this section. The method approximates the unknown function over the domain giving a solution to the structural problem. In order to carry out the review it is considered:

- Static equilibrium: The resultant forces at each node is zero.

- Linear elastic regime of the material is assumed.

- It is discretized by the standard Galerkin weighted residual method.

- 2D linear triangular elements are used.

Finally, FEM formulation of a boundary value problem results in a system of algebraic equations. Solving the system of equation the displacements and forces of every node are calculated.

3.3.1   Finite element model
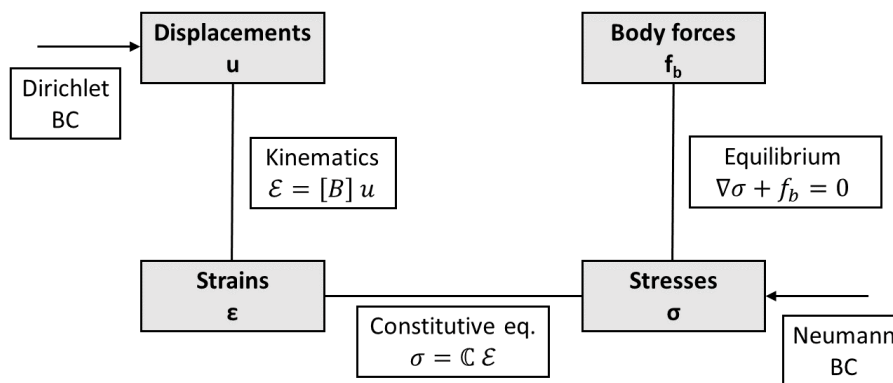
Fig. 3.5 Tonti's diagram of elasticity

The classical FEM is one of the main choices to solve problems in engineering and science. It is based on the replacement of continuous functions by piecewise approximations which make it more affordable from a mathematical and computational point of view. Figure 3.5 illustrates the scheme of the global problem, for simplicity linear elastic constitutive model

is used to describe the behavior of the material. The goal of the method is to know the strain/stress or load/displacement state based on the applied boundary conditions (BC).

The geometry of the continuum is considered to be formed by the assembly of infinitesimal domain with simple geometry termed finite element (triangle, tetrahedra, quadrilateral, hexahedra...). The problem to be solve is defined by imposing the boundary conditions (Dirichlet or Neumman) and establishing material properties (Constitutive models). The analysis is restricted to linear kinematics and to static equilibrium. These assumptions are graphically illustrated in Figure 3.5 and explained in the following points.

STATIC EQUILIBRIUM

The physical problem is governed by the structural equilibrium equation and Figure 3.6 shows a scheme of the continuum model. The strong form (differential equations) of the governing equation along with boundary conditions (Dirichlet and Neumann conditions) set the fundamentals that every point over the domain (Ω) must satisfy:

$$-\nabla \cdot \sigma - f_b = 0 \quad in \ \Omega \tag{3.7}$$

$$B.C. \begin{cases} u - u_0 = 0 & in \ \Gamma_D \\ \sigma \vec{n} - t_0 = 0 & in \ \Gamma_N \end{cases} \tag{3.8}$$
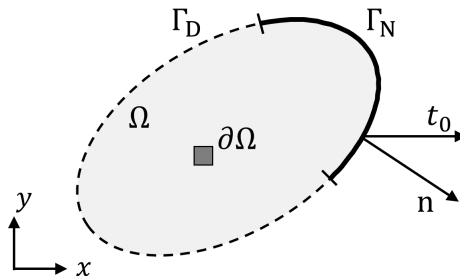
Fig. 3.6 2D continuum model

where σ is the stress tensor, $\nabla \cdot \sigma$ is the divergence of σ, f_b are the body forces, u are the displacement field, u_0 and t_0 are the given displacements and stresses, Γ_D and Γ_N are the Dirichlet and Neumann boundary conditions and $\vec{n}$ is the normal vector.

The strong equation can be transferred into an equivalent weak form by multiplication of an arbitrary weight function W. The order of the governing equation is reduced with the weak formulation making easier to solve the problem. Hence, the strong and the weak expressions

are equivalent. The weak equation over the domain can be rewritten in the weighted residual form as:

$$\int_\Omega W\,(\nabla \cdot \sigma + f_b)\,d\Omega = 0 \;\rightarrow\; W\int_\Omega f_b\,d\Omega = -W\int_\Omega \nabla \cdot \sigma\,d\Omega \tag{3.9}$$

Applying the property of the divergence:

$$\nabla \cdot (W\ \sigma) = \frac{\partial}{\partial x_j}\left(W_i\sigma_{ij}\right) = \frac{\partial W_i}{\partial x_j}\sigma_{ij} + \frac{\partial \sigma_{ij}}{\partial x_j}W_i = \sigma:\nabla W + W\ \nabla \cdot \sigma \tag{3.10}$$

$$W\ \nabla \cdot \sigma = \nabla \cdot (W\ \sigma) - \sigma:\nabla W \tag{3.11}$$

and substituting in Equation 3.9:

$$W\int_\Omega f_b\,d\Omega = -\int_\Omega \nabla \cdot (W\ \sigma)\,d\Omega + \int_\Omega \sigma:\nabla W\,d\Omega \tag{3.12}$$

Making use of the divergence theorem (Equation 3.14), which relates volume integrals to surface integrals of vector fields, the weak form may be written as:

$$\int_\Omega \nabla \cdot (W\ \sigma)\,d\Omega = \int_\Gamma W\sigma n\,d\Gamma \tag{3.13}$$

$$W\int_\Omega f_b\,d\Omega = -W\int_\Gamma \sigma n\,d\Gamma + \int_\Omega \sigma:\nabla W\,d\Omega \tag{3.14}$$

$$W\int_\Omega f_b\,d\Omega + W\int_\Gamma \sigma n\,d\Gamma = \int_\Omega \sigma:\nabla W\,d\Omega \tag{3.15}$$

The weak form of the equilibrium equation has three terms as it shown in Equation 3.15. The left-hand side of this equation is the internal virtual work and the right-hand side is referred to as the external virtual work.

GALERKIN FORMULATION

The numerical solution is approximated by an unknown function $\hat{u}$. The approximate solution must satisfy the boundary conditions and it is usually expressed as a linear combination of function. The same idea is also followed to build up the weight function. The Galerkin method consists in taking the weight function (W) as the shape functions (N_i) which gives:

$$u \cong \hat{u} = \sum_{i=1}^{n} N_i(x)\, a_i \tag{3.16}$$

$$W = \sum_{i=1}^{n} N_i(x)\, w_i \tag{3.17}$$

where $N_i(x)$ are the shape functions, a_i and w_i are the the unknown parameters and n is the number of nodes. Substituting the approximate solution into the weak form of the governing equation the continuity is reduced making easier to get a solution:

$$\int_{\Omega}\left(\sum_{i=1}^{n}N_i(x)\,w_i\right)f_b\,d\Omega = -\int_{\Gamma}\left(\sum_{i=1}^{n}N_i(x)\,w_i\right)\sigma n\,d\Gamma + \int_{\Omega}\sigma:\nabla\left(\sum_{i=1}^{n}N_i(x)\,w_i\right)d\Omega \tag{3.18}$$

Rearranging the equation, the discretized weak equation is defined as:

$$\sum_{i=1}^{n}w_i\int_{\Omega}\sigma\,\nabla N_i\,d\Omega = \sum_{i=1}^{n}w_i\left(\int_{\Omega}N_i\,f_b\,d\Omega + \int_{\Gamma}N_i\,t_0\,d\Gamma\right) \tag{3.19}$$

The above sum can be rewritten as a system of equalities for each element as:

$$\int_{\Omega}\sigma\,\nabla N\,d\Omega = \int_{\Omega}N\,f_b\,d\Omega + \int_{\Gamma}N\,t_0\,d\Gamma \tag{3.20}$$

LINEAR ELASTICITY

Once the discretized weak equation is defined for each element, the constitutive model must be introduced. In this case for simplicity, the linear elastic model is introduced as the law that governs the behavior of the material.

$$\sigma_{ij} = \mathbb{C}_{ijkl}:\varepsilon_{kl} \tag{3.21}$$

The infinitesimal deformations (ε_{kl}) of a continuum body is symmetric and it is given by displacement gradient as:

$$\varepsilon_{kl} = \frac{1}{2}\left[\nabla u + (\nabla u)^T\right] = \frac{1}{2}\left[u_k \otimes \nabla N_l + \nabla N_k \otimes u_l\right] \tag{3.22}$$

Substituting into the constitutive equation:

$$\begin{aligned}
\sigma_{ij} &= \frac{1}{2}\left[\mathbb{C}_{ijkl} : (u_k \otimes \nabla N_l + \nabla N_k \otimes u_l)\right] = \\
&= \frac{1}{2}\left[\mathbb{C}_{ijkl}\, u_k\, \nabla N_l + \mathbb{C}_{ijkl}\, \nabla N_k\, u_l\right] = \\
&= \frac{1}{2}\left[\mathbb{C}_{ijkl}\, u_k\, \nabla N_l + \mathbb{C}_{ijkl}\, u_k \nabla N_l\,\right] = \\
&= \mathbb{C}_{ijkl}\, u_k\, \nabla N_l
\end{aligned} \tag{3.23}$$

DISCRETIZATION

The shape functions interpolate the solution between the discrete values obtained at the nodes. Appropriate functions have to be used to get the desired accuracy level based on the characteristic of the solution. Low order polynomials are usually chosen as shape functions due to its simplicity and computational time. In this work linear shape functions and triangular element are used as illustrated Figure 3.7 and they are defined as:

$$N_i^{(e)}(x,y) = \frac{1}{2A^{(e)}}\left[a_i^{(e)} + b_i^{(e)}x + c_i^{(e)}y\right] \tag{3.24}$$

$$a_i^{(e)} = x_j^{(e)} y_k^{(e)} - x_k^{(e)} y_j^{(e)} \tag{3.25}$$

$$b_i^{(e)} = y_j^{(e)} - y_k^{(e)} \tag{3.26}$$

$$c_i^{(e)} = x_k^{(e)} - x_j^{(e)} \tag{3.27}$$
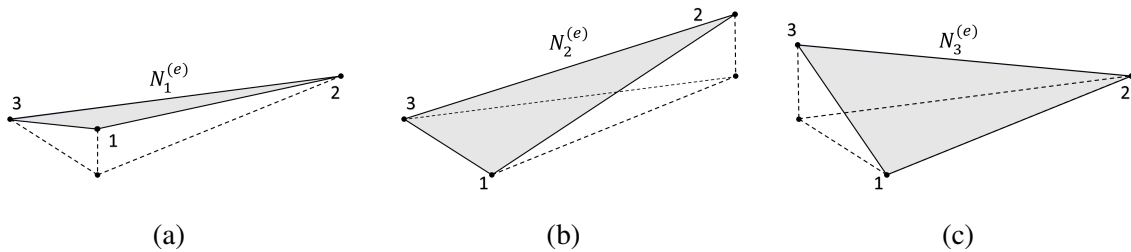
Fig. 3.7 Shape functions for linear triangle

These shape functions are defined based on the Cartesian coordinate system ($N_i^{(e)}(x,y)$). Nevertheless, the isoparametric element are used to standardize the procedure for every elements. Isoparametric elements increases the robustness of the FEM allowing to mesh irregular domains with unique elements. It is usual to define the triangle in terms of a normalized geometry and in a local coordinate system (α, β) as it is showed in Figure 3.8. The shape functions based in the local coordinate system are defined for each node as:

$$N_1 = 1 - \alpha - \beta \tag{3.28}$$

$$N_2 = \alpha \tag{3.29}$$

$$N_3 = \beta \tag{3.30}$$
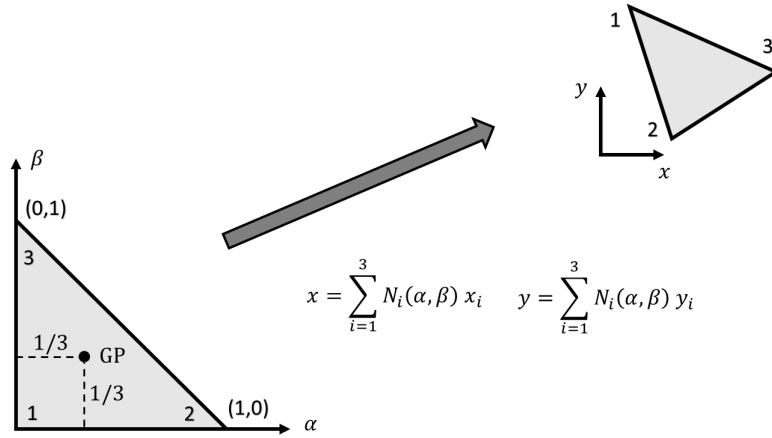
Fig. 3.8 Isoparametric mapping for linear triangle

The derivatives of the shape functions are defined through the Jacobian (J) and its inverse (J^{-1}), which allows to switch of coordinates system:

$$\nabla_{\alpha\beta} N = \begin{pmatrix} \frac{\partial N_i}{\partial \alpha} \\ \frac{\partial N_i}{\partial \beta} \end{pmatrix} = \begin{bmatrix} \frac{\partial x}{\partial \alpha} & \frac{\partial y}{\partial \alpha} \\ \frac{\partial x}{\partial \beta} & \frac{\partial y}{\partial \beta} \end{bmatrix} \begin{pmatrix} \frac{\partial N_i}{\partial x} \\ \frac{\partial N_i}{\partial y} \end{pmatrix} = J^{(e)} \begin{pmatrix} \frac{\partial N_i}{\partial x} \\ \frac{\partial N_i}{\partial y} \end{pmatrix} \tag{3.31}$$

$$\nabla_{xy} N = \begin{pmatrix} \frac{\partial N_i}{\partial x} \\ \frac{\partial N_i}{\partial y} \end{pmatrix} = \left[J^{(e)} \right]^{-1} \begin{pmatrix} \frac{\partial N_i}{\partial \alpha} \\ \frac{\partial N_i}{\partial \beta} \end{pmatrix} = \frac{1}{|J^{(e)}|} \begin{bmatrix} \frac{\partial y}{\partial \beta} & \frac{\partial y}{\partial \alpha} \\ \frac{\partial x}{\partial \beta} & \frac{\partial x}{\partial \alpha} \end{bmatrix} \begin{pmatrix} \frac{\partial N_i}{\partial \alpha} \\ \frac{\partial N_i}{\partial \beta} \end{pmatrix} \tag{3.32}$$

The determinant of the Jacobian matrix, besides being double of the area of a triangle, also relates the differential area in the two coordinate systems:

$$\partial x \partial y = |J^{(e)}| \, \partial\alpha\partial\beta \tag{3.33}$$

MATRIX FORM

The matrix form of the equilibrium equations for the whole mesh is constituted by a stiffness matrix, displacement vector and nodal force vector:

$$[\mathbf{K}]\{u\} = \{f\} \tag{3.34}$$

Returning to the weak form, the right side of the Equation 3.20 can be substituted by Equation 3.23:

$$
\begin{aligned}
\int_\Omega \sigma_{ij} \, \nabla N_j \, d\Omega &= \int_\Omega \mathbb{C}_{ijkl} \, u_k \, \nabla N_l \, \nabla N_j \, d\Omega = \\
&= \int_\Omega \mathbb{C}_{ijkl} \, \nabla N_l \, \nabla N_j \, u_k \, d\Omega = \int_\Omega \nabla N_j \, \mathbb{C}_{ijkl} \, \nabla N_l \; u_k \, d\Omega \quad \equiv \quad [\mathbf{K}]\{u\}
\end{aligned}
\tag{3.35}
$$

The global stiffness matrix ($\mathbf{K}$) is a function of the elastic properties of the solid element and is deduced from the previous equation as:

$$\mathbf{K_{ij}} = \int_\Omega \nabla N_j \, \mathbb{C}_{ijkl} \, \nabla N_l \, d\Omega = \int_\Omega \nabla N^T \, \mathbb{C} \, \nabla N \, d\Omega \tag{3.36}$$

After a transformation to isoparametric coordinates (α, β), the volume Ω is defined as a thickness (t_h) multiplied by an area ($\partial x \partial y$). The integral that yields the element stiffness matrix, becomes:

$$\partial\Omega = t_h \, \partial x \partial y = t_h \, |J^{(e)}| \, \partial\alpha\partial\beta = t_h \, |J^{(e)}| \, \partial\xi \tag{3.37}$$

$$\mathbf{K} = \int_\Omega \nabla N^T \, \mathbb{C} \, \nabla N \, d\Omega = t_h \int_\xi \nabla N^T \, \mathbb{C} \, \nabla N \, |J^{(e)}| \, d\xi \tag{3.38}$$

Numerical integration for each element of the domain subsequently results in:

$$k^{(e)} \cong \sum_{i=1}^{n_{GP}} w_{g,i} \, B_i^T \, \mathbb{C}^{(e)} \, B_i \, |J_i^{(e)}| \tag{3.39}$$

with $w_{g,i}$ the weight factor of integration point i, B is the strain-displacement matrix and n_{GP} the number of Gauss points in the element.

The global stiffness matrix is calculated assembling the stiffness matrix of each element. The global stiffness matrix must be symmetric because the element stiffness matrix is also symmetric. The global stiffness matrix, considering that in this research 2D model is proposed, is a square matrix with two times the number of nodes rows and columns.

$$\mathbf{K} = \sum_{1}^{e} k^{(e)} \tag{3.40}$$

The nodal load vector is defined from the the left-side of the Equation 3.20. It is a sum of body and surface forces. The body forces are defined as:

$$\int_{\Omega} N \, f_b \, d\Omega = t_h \int_{\Gamma} N \, f_b \, d\Gamma \tag{3.41}$$

If the body forces are uniformly distributed over the element, the total force acting over the element is split into equal parts between the three nodes of the triangle:

$$f_b^{(e)} = \frac{(A \, t_h)^{(e)}}{3} \begin{pmatrix} f_{bx} \\ f_{by} \end{pmatrix} \tag{3.42}$$

The surface forces are forces acting along the element side. In the case that the load is uniformly distributed along the element, the load is split in equal parts on the nodes. In all other cases, it is defined as:

$$\int_{\Gamma} N \, t_0 \, d\Gamma = t_h \int_{L} N \, t_0 \, dL \cong t_h \sum_{i=1}^{n_{GP}} w_{g,i} \, N_i^{(e)} \, t_0^{(e)} \, L^{(e)} = \frac{(LT_h)^{(e)}}{2} t_0^{(e)} \tag{3.43}$$

In this research, the discretization of the model was carried out through linear triangular elements and one Gauss Point was used to perform the numerical integration. Regarding the

stiffness matrix, sparsity was used to economize storage and computation time due to its high content of zeros.

3.3.2 Strong and weak discontinuity kinematics

Discontinuities are generated in solids when they are loaded beyond the elastic limit. The discontinuities, from a mechanical point of view, can be modeled as a strong or weak discontinuities. Figure 3.9 shows a body Ω crossed by a material discontinuity interface Γ_d and it is divided into two parts: Ω^+ and Ω^-. The normal vector to the discontinuity is defined as n. It is also defined the discontinuity band for weak approach $()\Omega_d)$.

(a) Weak discontinuity (b) Strong discontinuity
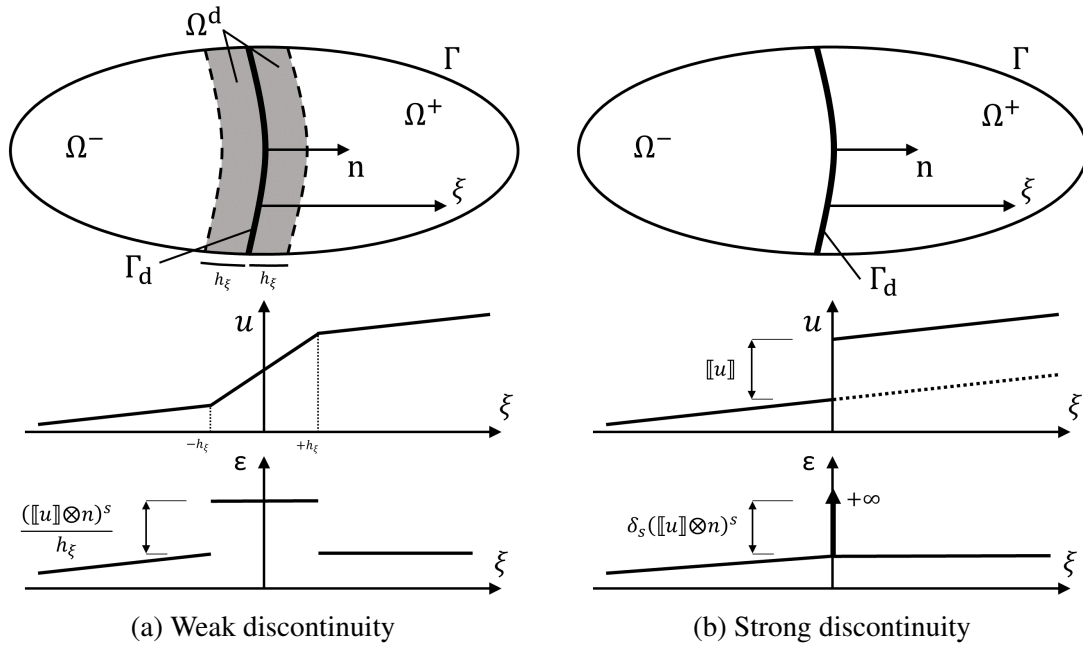
Fig. 3.9 Kinematic state of strong and weak discontinuity

The weak approach allows the direct application of continuum constitutive laws. The weak discontinuity are characterized by continuous displacement field and discontinuous strain field as is illustrated in Figure 3.9(a). The strain is localized in a narrow band Ω_d and it is applicable in problems that involve a considerable jump in the strain rate [29, 127].

The displacement field can be written as:

$$u = \bar{u} + H_s[\![u]\!] \tag{3.44}$$

where $\bar{u}$ is the continuous displacement field, $[\![u]\!]$ is the relative displacement and H_s is the Heaviside function centered on the discontinuity:

$$H_s = \begin{cases} 0 & \xi \in \Omega^- \\ 1 & \xi \in \Omega^+ \\ \dfrac{\xi - h_\xi^-}{h_\xi^+ - h_\xi^-} & \xi \in \Omega^d \end{cases} \tag{3.45}$$

The kinematic state of weak discontinuity is characterized by bounded and discontinuous strain field as can be shown in Figure 3.9(a). It is defined as:

$$\varepsilon = \nabla^s u = \nabla^s \bar{u} + H_s \nabla^s [\![u]\!] + \mu_s \frac{([\![u]\!] \otimes n)^s}{h_\xi} \tag{3.46}$$

where ∇^s is the symmetric gradient operator, $(\ )^s$ the symmetric part and μ_s is a collocation function placed on Ω_d ($\mu_s = 1$ if $\xi \in \Omega_d$ and $\mu_s = 1$ otherwise).

Strong discontinuities can be interpreted as the limit situation of the weak discontinuity, where the bandwidth tend to zero ($\Omega_d \to 0$) and strain field is unbounded as is illustrated in Figure 3.9(b). Consequently, the displacement field changes from ramp function to step function and the corresponding strain field can be computed as:

$$\varepsilon = \nabla^s u = \nabla^s \bar{u} + H_s \nabla^s [\![u]\!] + \delta_s ([\![u]\!] \otimes n)^s \tag{3.47}$$

where δ_s is the Dirac's delta function ($\delta_s = \infty$ if $\xi = 0$ and $\delta_s = 0$ otherwise) and introduce discontinuity in the strain field.

In contrast to the weak approach, the strong discontinuity kinematics is characterized by unbounded strain field along the discontinuity surface Γ_d. The strong approach is more suitable for elements that experienced jumps in the displacement field and highly localized failures [10, 123].

3.3.3 Continuum damage model

The damage of a solid is a synonym of stiffness degradation, what means a change in the elastic properties of the material. The damage phenomenon only affects to the elastic properties, while the plasticity describes the inelastic strain. The apparent simplicity of this model does not set the potential of the method back. It is widely used to represent the nonlinear behavior of metallic and geomaterials [65, 101, 39], such as concrete and steel.
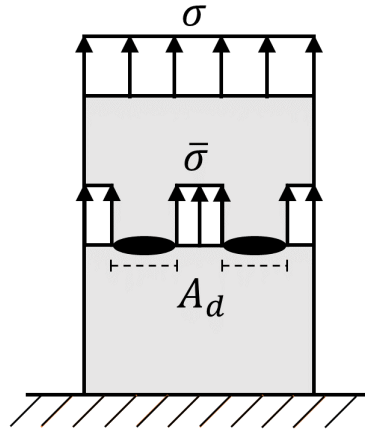
Fig. 3.10 Graphic representation of the damage

The continuous damage model characterize damage with a scalar variable, referencing as damage parameter d henceforth. This variable represents the deterioration level and evolves over the time. It ranges from 0 (undamaged) to 1 (completely damaged). The damage parameter decreases the effective area $\bar{A}$ ($\bar{A} = A - A_d$), which increase the effective stress $\bar{\sigma}$ ($\bar{\sigma} > \sigma$). The reduction of area is due to the formation of microvoids, which increase until cracks are formated. Figure 3.10 is a graphic illustration of a damage model.

$$\sum F = \sigma A - \bar{\sigma} \bar{A} = 0 \tag{3.48}$$

$$\sigma = \frac{\bar{A}}{A}\bar{\sigma} = \frac{A - A_d}{A}\bar{\sigma} = \left(1 - \frac{A_d}{A}\right)\bar{\sigma} = (1 - d)\bar{\sigma} \tag{3.49}$$

The strain generated by σ upon the damaged body can be associated to the deformation generated by $\bar{\sigma}$ to the undamaged model. Both stresses are related by the constitutive equation where $\mathbb{C}$ is the elastic tensor and $\mathbb{C}^d$ the damaged elastic tensor.

$$\sigma = (1 - d)\bar{\sigma} = (1 - d)\,\mathbb{C} : \varepsilon = \mathbb{C}^d : \varepsilon \tag{3.50}$$

Since the stresses must be bounded inside the elastic surface, the constitutive model must return stresses inside it ($\phi <= 0$). This condition is imposed by the damage criterion ϕ, which delimited the elastic domain and the degradation process:

$$\phi = \tau_e - r_t = \begin{cases} < 0 \; \textit{Elastic state} \\ = 0 \; \textit{On the damage surface} \\ > 0 \; \textit{Degradation process} \end{cases} \tag{3.51}$$

where τ_e is the equivalent strain and r_t is the strain-like internal variable. Equation 3.51 is stated in terms of strain, but it can be also proposed in terms of stress ($\phi = \sigma_e - q(r)$).

The damage law is defined in terms of internal variable (r). The strain-like internal variable must characterize the maximum strain reached along the loading/unloading history. The role of the strain-like internal variable can be understood easier in an unloading evolution. The strain decreases but the damage induces in the previous pseudo-time step must remain constant. Therefore, the evolution of damage cannot be defined by the strains at specific time step. There must be used a variable that consider the historical evolution: strain-like internal variable.

$$d(r) = 1 - \frac{q(r)}{r} \tag{3.52}$$

The constitutive model has to be complemented by the loading/unloading conditions given by Kuhn-Tucker's relations:

$$\dot{r} \geq 0 \; ; \; \phi \leq 0 \; ; \; \dot{r}\phi = 0 \tag{3.53}$$

and the persistency/consistency conditions:

$$\dot{r}\dot{\phi} = 0 \; if \; \phi = 0 \tag{3.54}$$

These conditions ensure that the internal variable cannot decrease and the loading point is always inside the elastic domain or on the boundary. Figure 3.11 shows a resume of the evolution of the damage surface.

Fig. 3.11 Resume of continuum damage models

Softening law for plain concrete

The adopted softening law must be able to simulate the degradation of concrete due to tensile stress. In this dissertation, an exponential softening law is assumed defined in terms of an internal variable (r):

$$q(r) = q_0 \, e^{S \, h \, (1 - r/q_0)} \tag{3.55}$$

where q_0 is the initial tensile strength (f_t), S is the softening parameter, h is the height of interface elements .

The softening parameter for the mode I is given as:

$$S = \frac{f_t^2}{G_f \, E_H} \tag{3.56}$$

where G_f is the fracture energy and E_H is Young's modulus of concrete.

Figure 3.12 shows the tension damage model of a simple case where a pair of interface triangular elements are introduced between bulk elements. The first part of the curve, until
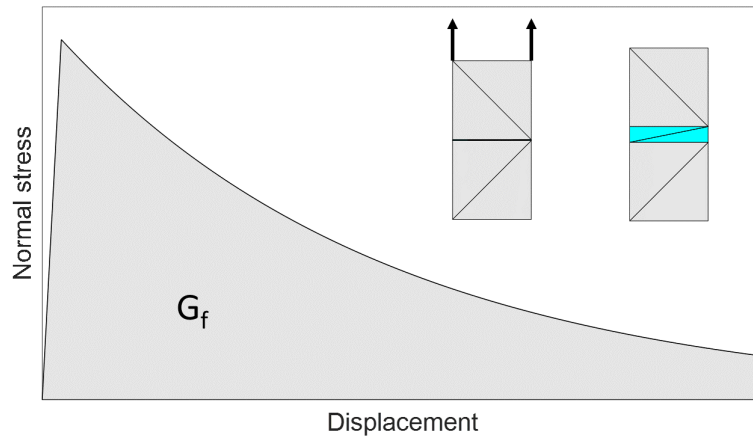
Fig. 3.12 Softening curve of a tensile damage model

the tensile strength is reached, is linear and then follows the predefined exponential curve. In the elastic domain there is not any damage and the interface element do not deformed significantly. Once the tensile strength is exceeded, the elements start damaging and the strain are more visible. The curve is defined by the maximum value of the stress (tensile strength, the enclosed area by the curve (fracture energy) and the slope of the elastic part (Young's modulus).

Bridging law

The bridging effect is divided into the contribution of matrix and fibers. The bridging effect of concrete is provided by the interlocking of aggregates and additional stitching effect is generated when fibers are added [89], which cross the crack. As in the previous case, an exponential softening law is adopted for plain concrete f_{con} and a hardening law f_{fib} to simulate the effect of adding fibers.

$$f = f_{con} + f_{fib} \tag{3.57}$$

The softening law of plain concrete depends on the crack opening displacement ω as it showed in Figure 3.13. The reference crack opening displacement ω_{ref} is assumed as the displacement when the crack is generated. After this point, the contribution of concrete decreases and fibers start acting.

$$\omega_{ref} = \frac{G_F}{f_{t(com)}} \tag{3.58}$$

$$f_{con}(\omega) = f_{t(com)} \, e^{\omega/\omega_{ref}} \tag{3.59}$$

$f_{t(com)}$ is the tensile strength of the mixture of fibers and concrete, which takes slightly greater values than the tensile strength of plain concrete.
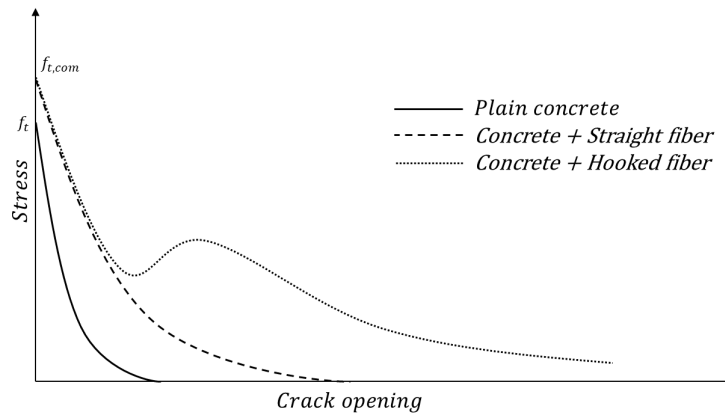
Fig. 3.13 Crack bridging curve for different fibers

Fibers effect is based on the contribution of the frictional strength and the hooking effect, in case of hooked fibers were added. The effect of fibers vanish while they are pulling out. In this case an homogeneous distribution is considered within a finite element, therefore, fibers are pulled out when half of its length L_f is displaced. The ultimate crack opening ω_u can be defined as:

$$\omega_u = \frac{L_f}{2} \tag{3.60}$$

The adopted bridging law is demonstrated that can be used to represent traction-separation laws for different fiber-concrete composites in [201], which ensures a wide applicability. It synthesizes the introduced concepts in a simple manner. The first term of the equation is associated with concrete. The second term introduces the frictional aspect during the pullout procedure. The last term is correlated with the anchorage effect that some fibers might have due to its shape, such as the hooked-end fibers. The bridging law is expressed as:

$$f(\alpha) = (f_{t,com} - t_1)\ e^{\frac{-\alpha}{\omega_{ref}}} + t_1 \frac{\omega_u - \alpha}{\omega_u} + t_2\ \alpha\ e^{C_1 - C_2 \alpha} \tag{3.61}$$

where t_1, t_2, c_1, and c_2 are coefficients for fitting the numerical solution [201].

Figure 3.13 shows the common curves of composites based on the typer of fibers. Furthermore, other parameters as fiber density, material, length etc. also affects the behavior of the composite. These aspects are considered by the parameters t_1, t_2, c_1, and c_2, which fit the numerical curve to the experimental curve. Figure 3.14 illustrates the effect of the four variables.
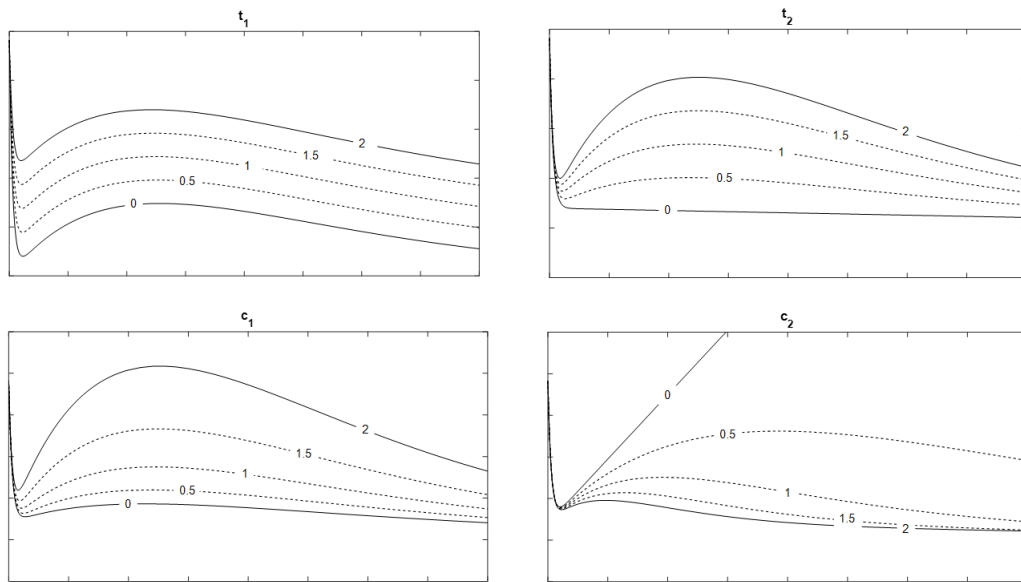
Fig. 3.14 Stress-crack opening displacement relation depending on t_1, t_2, c_1, and c_2

Chapter 4

Numerical implementation and validation

4.1 Introduction

The objective of this chapter is to present the constitutive model used to model the behavior of concrete, fibers and steel bars. Tensile damage models are used to model concrete fracture and bridging phenomena due to the addition of fibers. It is also showed the introduction of interface elements and steel bars in the standard mesh. The chapter concludes with examples of the applied constitutive models.

4.2 Implicit-Explicit algorithm

In this research, a combination of implicit and explicit integration schemes (IMPL-EX) are used to calculate the stress-strain state at every pseudo-time step. The combination of both schemes leads to formulations with constant pseudo-time step and non-singular stiffness matrix. It results in improvements in terms of robustness (explicit scheme) and computational cost (implicit scheme) [124].

Explicit integration schemes are characterized by being conditionally stable and robust, though it demands a high computational cost. This implies that load step length is limited and a large number of time steps are needed to solve the problem [124]. The error is associated to the pseudo-time step length.

Implicit integration schemes are unconditionally stable and facilitate larger time steps. Despite this advantage, the implicit methods can be extremely time-consuming when solving dynamic and nonlinear problems [124].

4.2.1 IMPL–EX algorithm for damage models

The IMPL–EX scheme for damage models is a combination of implicit and explicit integration schemes. At a certain pseudo-time step t_n, the stresses and strains are computed implicitly following the selected constitutive model. Then, internal variables are extrapolated for the next loading step, t_{n+1}, in terms of the implicit variables calculated at the previous time step. The internal variables are used to compute the tangent operator for the next time step.

<div align="center">

Table 4.1 IMPL–EX integration algorithm for damage models

</div>

INPUT: ε_n, r_n, d_n
1) Compute the effective stress: $\quad\bar{\sigma}_n = \mathbb{C}\,\varepsilon_n$
2) Damage criterion: $\phi_d = \tau_{\bar{\sigma}_n} - q(r_n)$ $\qquad\phi_d < 0 \to$ Elastic domain: $r_{n+1} = r_n$ $\qquad\phi_d = 0 \to$ On the damage surface: $r_{n+1} = r_n$ $\qquad\phi_d > 0 \to$ Damage: $r_{n+1} = \frac{q(r_n)}{1-d_n}$
3) Extrapolate the strain-like internal variable: $\quad r_{n+1}^{ex} = r_n + \frac{r_{n+1}-r_n}{t_n-t_{n-1}}\,(t_{n+1}-t_n)$
4) Update the damage variable: $\quad d_{n+1}^{ex} = 1 - \frac{q(r_{n+1}^{ex})}{r_{n+1}^{ex}}$
5) Compute the tangent operator: $\quad\mathbb{C}_{n+1}^{tan} = \left(1 - d_{n+1}^{ex}\right)\mathbb{C}$
OUTPUT: σ_n, r_{n+1}, d_{n+1}

Table 4.1 summarizes the general algorithm for damage models. The damage criterion is calculated comparing the effective stress $\bar{\sigma}_n$ and the softening law $q(r_n)$. This function allows to evaluate if the element is being damaged or is in the elastic range. Based on this criterion, the strain-like internal variable (r_{n+1}) is actualized, which controlled the size of the elastic surface. Finally, the tangent operator $\mathbb{C}_{n+1}^{tan}$ is computed after extrapolating the internal variable using backward difference scheme for the time derivative, which is truncated after the first derivative,

$$\begin{cases} r_{n+1} = r_n + \dot{r}_n\,\Delta t_{n+1} + \mathcal{O}(\Delta t^2) \\ r_n = r_{n-1} + \dot{r}_{n-1}\,\Delta t_n + \mathcal{O}(\Delta t^2) \end{cases} \tag{4.1}$$

$$r_{n+1} = r_n + \Delta r_n \frac{\Delta t_{n+1}}{\Delta t_n} + \mathcal{O}(\Delta t^2) \tag{4.2}$$

4.2.2 IMPL–EX algorithm for elastoplastic models

The IMPL–EX algorithm for elastoplastic computes stresses explicitly and implicitly in a representative time step t_n. The explicit stresses are used to fulfill the balance equation, while the implicit stresses are used as the updated stresses for the next time step t_{n+1}.

Table 4.2 IMPL–EX integration algorithm for elastoplasticity models

---

INPUT: ε_n, σ_{n-1}, $\Delta\lambda_{n-1}$

---

1) Compute the trial stress:
$\qquad \sigma_n^{trial} = \sigma_{n-1} + \mathbb{C}\,\Delta\varepsilon_n$

2) Yield criterion: $\phi_y = \phi^{trial}(\sigma_n^{trial}, \kappa_{n-1})$
$\qquad \phi_y < 0 \rightarrow$ Elastic domain: $\Delta\lambda_n = 0$
$\qquad \phi_y = 0 \rightarrow$ On the plastic surface: $\Delta\lambda_n > 0$
$\qquad \phi_y > 0 \rightarrow$ Plasticity: $\Delta\lambda_n > 0$

3) Implicit plastic strain:
$\qquad \Delta\varepsilon_n^P = \Delta\lambda_n \frac{\partial\phi^P(\sigma_n^{trial})}{\partial\sigma_n^{trial}}$

4) Explicit plastic strain:
$\qquad \Delta\lambda_n^{exp} = \Delta\lambda_{n-1}$
$\qquad \kappa_n = \int_0^t \dot{\kappa}\,dt$
$\qquad \Delta\varepsilon_n^{P,\,exp} = \Delta\lambda_n^{exp}\,\mathbb{C}\,\frac{\partial\phi^P(\sigma_n^{trial})}{\partial\sigma_n^{trial}}$

5) Implicit stress:
$\qquad \sigma_n = \sigma_n^{trial} - \mathbb{C}\,\Delta\varepsilon_n^P$

6) Explicit stress:
$\qquad \sigma_n = \sigma_n^{trial} - \mathbb{C}\,\Delta\varepsilon_n^{P,\,exp}$

7) Compute the tangent operator:
$\qquad \mathbb{C}_n^{tan} = \frac{\partial\sigma_n}{\partial\varepsilon_n}$

OUTPUT: σ_n, $\mathbb{C}_n^{tan}$, κ_n, $\Delta\lambda_n$

The algorithm for elastoplasticity is summarized in Table 4.2. The yielding conditions is evaluated at a certain time step t_n using the trial stress σ_n^{trial} and the hardening parameter κ_{n-1}. There is not any plastic strain if the yield function is $\phi^{trial} < 0$. In case plastic state takes place, implicit system of non-linear equation have to be solved usually with Newton-Raphson method. The variables to be calculated are stress state at t_n, plastic multiplier $\Delta\lambda_n$, hardening parameter κ_n and increment of plastic strain $\Delta\varepsilon_n^P$. The plastic multiplier

or consistency parameter $\Delta\lambda_n$ is a scalar calculated through the consistency/persistency condition $(\Delta\lambda_n \dot{\phi}^{trial} = 0)$ and it ensures that stress state lies on the yield surface during the plastic flow. The hardening parameter κ_n is the equivalent to the effective plastic strain for multiaxial loading and depends on the strain history. The plastic strain increment is computed through the plastic multiplier $\Delta\lambda_n$ and the potential function ϕ^P. If the same function is used as yield function and potential function, materials are considered to follow the associative flow rule of plasticity. Otherwise, non-associative flow-rule is followed. Once the strain and stress is actualized, the tangent operator can be defined and with the next loading step may be continued.

4.3 Implementation of interface elements

A technique based on the insertion of interface elements between regular elements of the mesh is used to capture the cracking phenomena in concrete. These interface elements must be able to describe the kinematics associated to discontinuities, so that the crack formation can develop along the boundaries of the bulk elements. The domain is discretized with an unstructured mesh to capture the crack paths accurately and to avoid being influenced by the mesh orientation. Afterward, the tensile damage model is introduced depending on the governing behavior of the material (plain concrete or fibers reinforced concrete). The IMPL-EX scheme is applied to find the stress strain relationship in both cases.

4.3.1 Inserting at interface elements into the mesh

The method proposed by *Manzoli et al*. [100] is based on the use of pairs of triangular finite elements with high aspect ratio. They are inserted between bulk elements of the conventional mesh. Concrete elements are discretized with triangular elements using the software Gmsh (open-source code) [62]. Then, intermediate elements are introduced to represent the crack propagation.

The developed procedure allows inserting intermediate elements locally on any standard element. Therefore, a loop through elements is needed. This process required few modifications of the meshing data. The main steps can be summarized as follows:

1. Figure 4.1(a) shows the generation of the standard mesh through Gmsh mesh generator [62], which supplied the nodal coordinates and connectivity matrix.

2. Introducing of the gaps between the elements according to the specified thickness in the region to be fragmented. These gaps are usually small, around the 1% of the
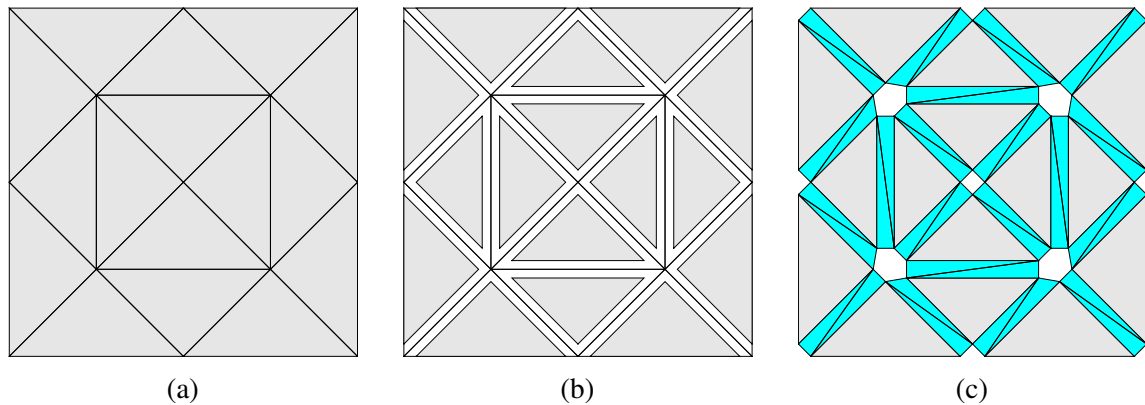
Fig. 4.1 Inserting interface elements into a standard mesh (a) Standard finite element mesh (b) Introduction of gaps (c) Insertion of interface finite element

size of the regular elements [101], and better results are obtained while the thickness is reduced. In the present work, the heigth of the elements is between 1×10^{-3} and 1×10^{-4} mm. It is worth noting that in Figure 4.1(b) the size of the gaps is increased in order to appreciate better.

The selected elements are shrunk shifting the edges by half of the gap. The common edges are duplicated and the number of nodes increases considerably. Therefore, the coordinates and connectivity matrix must be rearranged because new nodes are generated and some existing nodes disappears.

3. Insertion of intermediate elements. The gap between bulk element are filled with pairs of triangular elements (interface elements) as it is illustrated in Figure 4.1(c).

This technique can be easily implemented in standard FEM programs using conventional solid elements. The interface elements can be generated in specific regions where cracking might be foreseen, to reduce the required computational cost for the simulation.

4.3.2   Damage model for concrete: Brittle fracture

The tension damage model is an appropriate technique to describe the deterioration of concrete due to crack propagation. In this dissertation, the damage model proposed by *Manzoli et al.* [101] is applied to simulate the brittle behavior of plain concrete.

Figure 4.2 shows the flowchart of the implemented algorithm to simulate the tensile behavior, which follows the following steps:

$$[K_n]\,\{u_n\} = \{f_{ext}\}$$

Implicit stage
$$\varepsilon_n = B\,\{u_n\}$$
$$\bar{\sigma}_n = \mathbb{C}\,\varepsilon_n$$
$$\bar{\sigma}_{nn} = \bar{n}\,\bar{\sigma}_{nn}\,\bar{n}$$

No

$$\bar{\sigma}_{nn} - r_n > 0$$

Yes

$$t_n = t_n + \Delta t$$

No damaged
$$r_{n+1} = r_n$$
$$q_{n+1} = q_n$$
$$d_{n+1} = d_n$$

Damaged
$$r_{n+1} = \bar{\sigma}_{nn}$$
$$q_{n+1} = f_t\,e^{Sh\frac{f_t}{1-r_{n+1}}}$$
$$d_{n+1} = 1 - \frac{q_{n+1}}{r_{n+1}}$$

Explicit stage
$$r_{n+1}^{ex} = r_n + \frac{r_{n+1}-r_n}{t_n-t_{n-1}}\,(t_{n+1}-t_n)$$
$$q_{n+1}^{ex} = f_t\,e^{Sh\frac{f_t}{1-r_{n+1}^{ex}}}$$
$$d_{n+1}^{ex} = 1 - \frac{q_{n+1}^{ex}}{r_{n+1}^{ex}}$$
$$\mathbb{C}_{n+1}^{tan} = (1 - d_{n+1}^{ex})\,\mathbb{C}$$
$$k_e = k_e(\mathbb{C}_{n+1}^{tan})$$
$$K_{n+1}^{ex}\,\{u\}_{n+1} = \{f_{ext}\}_{n+1}$$
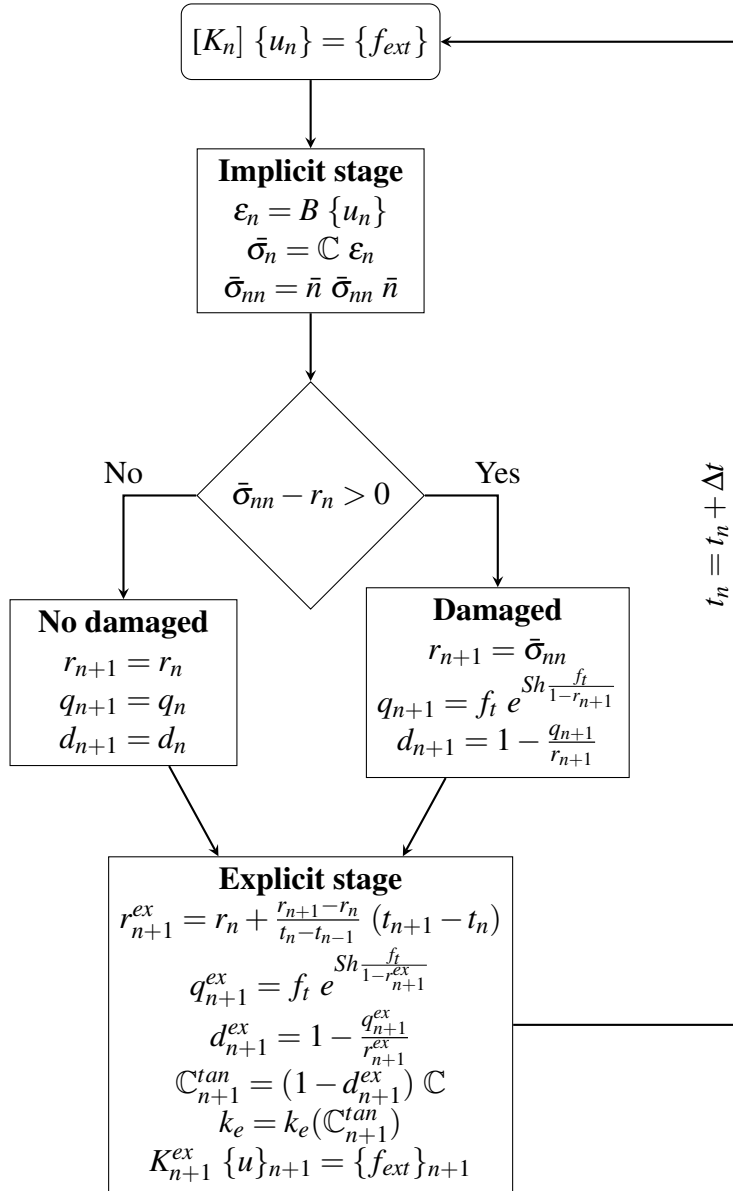
Fig. 4.2 Flowchart of the algorithm implemented for the interface element for plain concrete

1. **Initial state:** The internal variables, damage parameter and softening law must be
   initialized as:

$$r_n = f_t \tag{4.3}$$

$$q_n = f_t \tag{4.4}$$

$$d_n = 0 \tag{4.5}$$

and it is worth mentioning that used method is a strain driven algorithm.

2. **Implicit stage:** The effective stress $\bar{\sigma}_n$ of each element at t_n pseudo-time step is determined form the strain tensor ε_n and the elastic tensor $\mathbb{C}$. As the damage criterion is expressed in terms of the normal component of the effective stress $\bar{\sigma}_{nn}$, it is calculated as:

$$\bar{\sigma}_n = \mathbb{C}\, \varepsilon_n \tag{4.6}$$

$$\bar{\sigma}_{nn} = \bar{n}\, \bar{\sigma}_n\, \bar{n} \tag{4.7}$$

where $\bar{n}$ is the unit vector normal to the base of the triangle.

The damage criterion ϕ controls the size of the elastic surface, consequently it indicates whether the element is in the elastic range or it is being damaged. In that instance, internal variables have to be updated:

$$r_{n+1} = \bar{\sigma}_{nn} \tag{4.8}$$

$$q_{n+1} = f_t\, e^{Sh\frac{f_t}{1-r_{n+1}}} \tag{4.9}$$

$$d_{n+1} = 1 - \frac{q_{n+1}}{r_{n+1}} \tag{4.10}$$

S is the softening parameter, h is the height of the interface element, f_t is the tensile strength of concrete.

3. **Explicit stage:** The tangent operator $\mathbb{C}_{n+1}^{tan}$ is determined to calculate the stiffness matrix of every triangular element k_e. Once the stiffness matrix is assembled K_{n+1}^{ex}, the nodal displacement can be calculated for the next pseudo-time step. But firstly, the explicit extrapolation of the internal variables have to be carried out:

$$r_{n+1}^{ex} = r_n + \frac{r_{n+1} - r_n}{t_n - t_{n-1}}\, (t_{n+1} - t_n) \tag{4.11}$$

$$q_{n+1}^{ex} = f_t\, e^{Sh\frac{f_t}{1-r_{n+1}^{ex}}} \tag{4.12}$$

$$d_{n+1}^{ex} = 1 - \frac{q_{n+1}^{ex}}{r_{n+1}^{ex}} \tag{4.13}$$

Proceed with the next pseudo-time step until the loading stage finished.

4.3.3 Damage model for fibers: Bridging effect

The IMPL-EX integration scheme is implemented for the integration of the stress-strain relation. This method has been widely applied to damage models with positive results [100, 101]. Figure 4.3 illustrates the structure of the tensile-damage algorithm:

$$[K_n]\,\{u_n\} = \{f_{ext}\}$$

Implicit stage

$$\varepsilon_n = B\,\{u_n\}$$

$$\sigma_n = (1 - d_{n-1})\,\mathbb{C}\,\varepsilon_n$$

$$\tilde{\sigma} = \sqrt{\sigma_{nn}^2 + \left(\frac{\sigma_{nr}}{\beta}\right)^2 + \left(\frac{\sigma_{ns}}{\beta}\right)^2}$$

$$\tilde{u} = \sqrt{u_n^2 + \frac{u_r^2}{2\,\beta} + \frac{u_s^2}{2\,\beta}}$$

$$\alpha = max(\tilde{u}) - \tilde{u}_0$$

$$f_n(\alpha) = (f_{t,com} - t_1)\,e^{\frac{-\alpha}{\omega_{ref}}} + t_1 \frac{\omega_u - \alpha}{\omega_u} + t_2\,\alpha\,e^{C_1 - C_2\alpha}$$

$$\tilde{\sigma}_n - f_n > 0$$

No   Yes

$$t_n = t_n + \Delta t$$

No damaged

$$d_n = d_{n-1}$$
$$H_n = 0$$
$$\alpha_n = \alpha_{n-1}$$

Damaged

$$d_n = 1 - \frac{h\,f_n}{E_{com}\,(\alpha + \tilde{u}_0)}$$

$$H_n = \frac{f_n - f_{n-1}}{\alpha_n - \alpha_{n-1}}$$

$$\alpha_n = \alpha$$

Explicit stage

$$\alpha_{n+1}^{ex} = \alpha_n + \frac{t_{n+1} - t_n}{t_n - t_{n-1}}\,(\alpha_n - \alpha_{n-1})$$

$$f_{n+1}^{ex} = f_n + H_n(\alpha_{n+1}^{ex} - \alpha_n^{ex})$$

$$d_{n+1}^{ex} = 1 - \frac{h\,f_{n+1}^{ex}}{E_{com}\,(\alpha_{n+1}^{ex} + \tilde{u}_0)}$$

$$k_e^{ex(e)} = (1 - d_{n+1}^{ex})\,k_e$$

$$K_{n+1}^{ex}\,\{u\}_{n+1} = \{f_{ext}\}_{n+1}$$
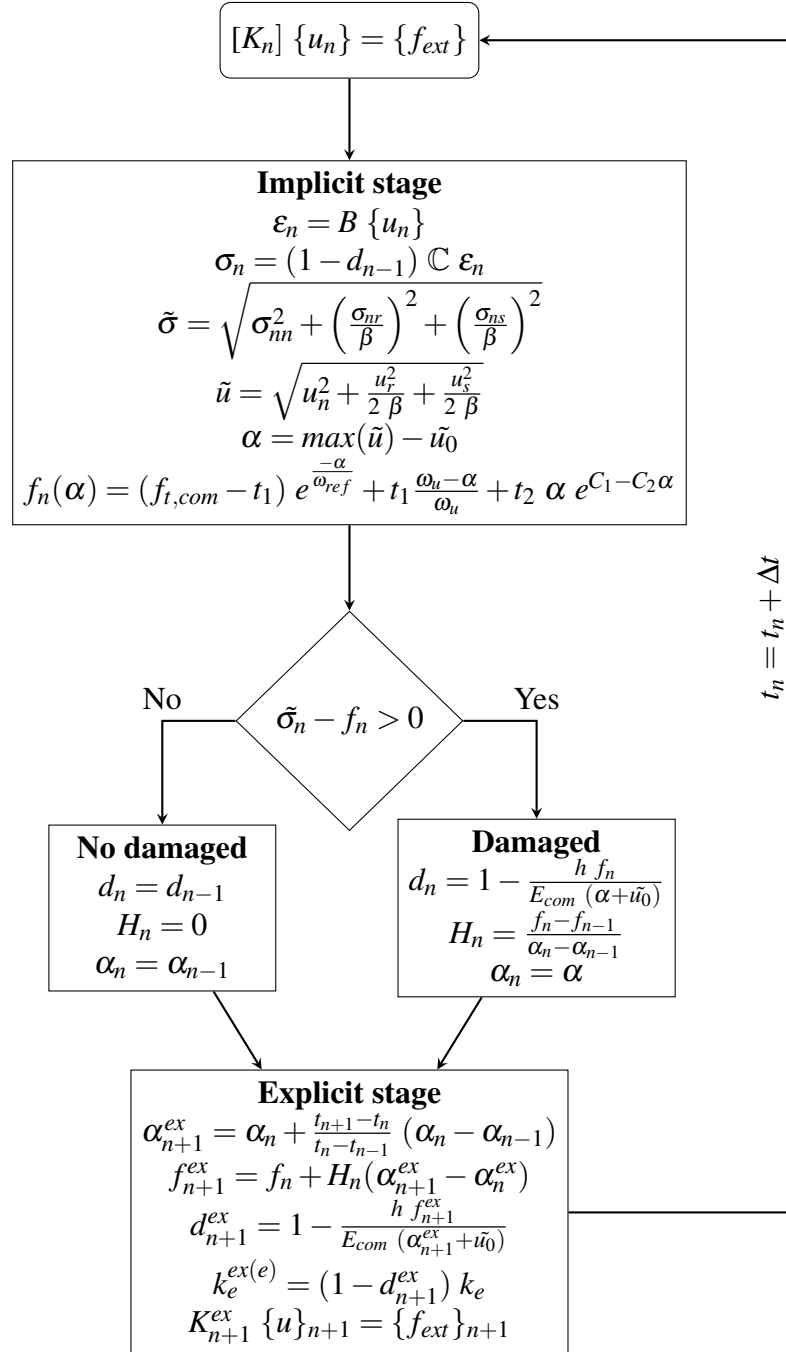
Fig. 4.3 Flowchart of the algorithm implemented for the interface element for fibers

1. **Initial state:** Prior to commencement, the internal variables and damage parameter must be initialized:

$$d_n = d_n^{ex} = 0 \tag{4.14}$$

$$\alpha_n = \alpha_n^{ex} = 0 \tag{4.15}$$

2. **Implicit stage:** For a given displacement vector, u_n, the corresponding strain tensor, ε_n, and effective stress tensor, σ_n are computed. Then, the equivalent stress $\tilde{\sigma}$ and displacement $\tilde{u}$ are calculated:

$$\tilde{\sigma} = \sqrt{\sigma_{nn}^2 + \left(\frac{\sigma_{nr}}{\beta}\right)^2 + \left(\frac{\sigma_{ns}}{\beta}\right)^2} \tag{4.16}$$

$$\tilde{u} = \sqrt{u_n^2 + \frac{u_r^2}{2\,\beta} + \frac{u_s^2}{2\,\beta}} \tag{4.17}$$

where σ_{nn}, σ_{nr} and σ_{ns} are the components of the stress of the base of the elements, $[\![u_n]\!]$, $[\![u_r]\!]$ and $[\![u_s]\!]$ are the the relative displacements of the base of the elements and β is the ratio between the tensile and shear strength (see Figure 3.4).

The strain-like internal variable α is defined as the maximum value of the separation during the loading history and $\tilde{u}_0$ corresponds to the displacement at the elastic limit.

$$\alpha = max(\tilde{u}) - \tilde{u}_0 \tag{4.18}$$

$$\tilde{u}_0 = \frac{h\,f_{t,com}}{E_{com}} \tag{4.19}$$

Substituting previous values in the bridging law the softening behavior is determined as:

$$f_n(\alpha) = (f_{t,com} - t_1)\,e^{\frac{-\alpha}{\omega_{ref}}} + t_1 \frac{\omega_u - \alpha}{\omega_u} + t_2\,\alpha\,e^{C_1 - C_2\alpha} \tag{4.20}$$

The damage criterion can be expressed in terms of effective stress and internal variable as:

$$\phi = \tilde{\sigma}_n - f_n(\alpha) < 0 \tag{4.21}$$

The previous inequality indicates that an elastic/unloading takes place when $\phi < 0$. Consequently, strain-like internal variable (α_n), softening modulus(H_n) and damage variable (d_n) are updated depending on whether the element is damaged.

$$\alpha_n = \alpha \tag{4.22}$$

$$H_n = \frac{f_n - f_{n-1}}{\alpha_n - \alpha_{n-1}} \tag{4.23}$$

$$d_n = 1 - \frac{h\, f_n}{E_{com}\,(\alpha_n + \tilde{u}_0)} \tag{4.24}$$

3. **Explicit stage:** The strain-like internal parameter calculated in the implicit step is used to determine the explicit extrapolation of the internal variable, α_{n+1}^{ex}, through the Taylor´s expansion. Subsequently, the explicit extrapolation of bridging stress f_{n+1}^{ex} and damage parameter d_{n+1}^{ex} can be calculated:

$$\alpha_{n+1}^{ex} = \alpha_n + \frac{t_{n+1} - t_n}{t_n - t_{n-1}}\,(\alpha_n - \alpha_{n-1}) \tag{4.25}$$

$$f_{n+1}^{ex} = f_n + H_n(\alpha_{n+1}^{ex} - \alpha_n^{ex}) \tag{4.26}$$

$$d_{n+1}^{ex} = 1 - \frac{h\, f_{n+1}^{ex}}{E_{com}\,(\alpha_{n+1}^{ex} + \tilde{u}_0)} \tag{4.27}$$

The explicit stiffness matrix for each element $k_{n+1}^{ex(e)}$ can be calculated at pseudo-time step t_{n+1} using the elastic stiffness matrix:

$$k_{n+1}^{ex(e)} = (1 - d_{n+1}^{ex})\, k_e \tag{4.28}$$

The linear system of equations can be built assembling the stiffness matrix of each element into the global stiffness matrix:

$$K^{ex}_{n+1} \{u\}_{n+1} = \{f_{ext}\}_{n+1} \qquad (4.29)$$

where K^{ex}_{n+1} is the global stiffness matrix, $\{u\}_{n+1}$ is the displacements at the next time step and $\{f_{ext}\}_{n+1}$ is the external force vector.

Proceed with the next pseudo-time step until the loading stage finished.

4.4   Reinforcement modeling

Longitudinal and shear reinforcement are modeled with discrete truss elements [167] and Menegotto-Pindo constitutive model is applied to them.

4.4.1   Reinforcement discretization

Reinforcing bars can be modeled as a smeared overlay or with truss elements. Considering the introduction of interface elements to capture the cracks, truss elements are selected as the best choice to avoid inducing preferential cracking paths and to allow discrete cracks crossing the reinforcement.

Figure 4.4 summarizes the idea behind the discretization scheme. It is worth pointing out the dimensions are distorted, so that, it facilitates the visualization. Firstly, the triangular elements have to be undersized to insert the interface elements. The number of interior nodes is increased due to the introduction of interface elements. Consequently, linear elements, which originally had one starting and end point, can be redefined in several ways. Nevertheless, it must be sought to have the highest number of nodes connected for reasons of numerical stability and restraining conditions [167].

In this context, the longitudinal (or flexural) reinforcements are divided into the sufficient number of truss elements that realizes the above-mentioned premise. This approach is intuitive as regards the structural meshes. However, it must be particularized for unstructured meshes to suit to the number of starting and end nodes.

Concerning the transversal (or shear) reinforcements, they can be simplified by two linear elements forming a cross. This streamlining optimizes the computational cost while it provides enough restraint to the model [167]. Figure 4.4 illustrates the different steps of the method.

<table>
<tr><td>(a)</td><td>(b)</td><td>(c)</td></tr>
</table>
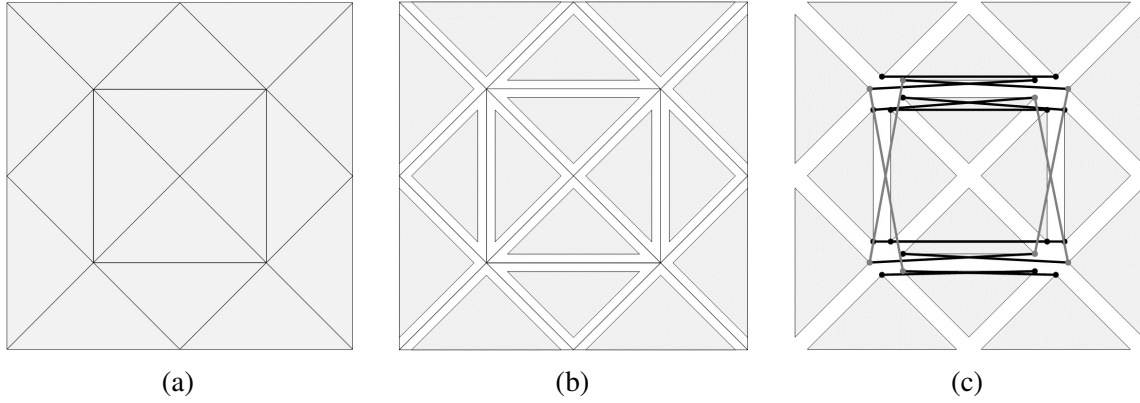
Fig. 4.4 Reinforcement discretization

4.4.2 Menegotto-Pinto model

The constitutive model selected to simulate the behavior of steel bars is Menegotto-Pinto plasticity model [138], which is widely used to simulate structural steel [20, 33, 131, 143]. It is a bilinear model where the first part is a line defined by the elastic modulus (E_0) and yield stress (σ_y) of the steel while the second line is defined by the slope or hardening modulus (E_1) as it is illustrated in Figure 4.5. The stress is calculated from normalized stress as,

$$\sigma^* = \frac{\sigma - \sigma_r}{\sigma_y - \sigma_r} \quad \rightarrow \quad \sigma = \sigma^* (\sigma_y - \sigma_r) + \sigma_r \tag{4.30}$$

$$\sigma^* = \frac{E_1}{E_0}\, \varepsilon^* + \frac{\left(1 - \frac{E_1}{E_0}\right) \varepsilon^*}{\left(1 + |\varepsilon^*|^{R_0}\right)^{1/R_0}} \tag{4.31}$$

$$\varepsilon^* = \frac{\varepsilon - \varepsilon_r}{\varepsilon_y - \varepsilon_r} \tag{4.32}$$

where ε^* and σ^* are the normalized strain and stress, ε_r and σ_r are the strain and stress at the last reversal time and R_0 is the curvature at the first loading step.

The transition curve between the two asymptotes is determined by the curvature (R):

$$R = R_0 - \frac{a_1\, \xi_n}{a_2 + \xi_n} \tag{4.33}$$

where a_1 and a_2 are experimentally determined parameters and ξ_n is the ratio of the maximum plastic strain over the initial yield strain.
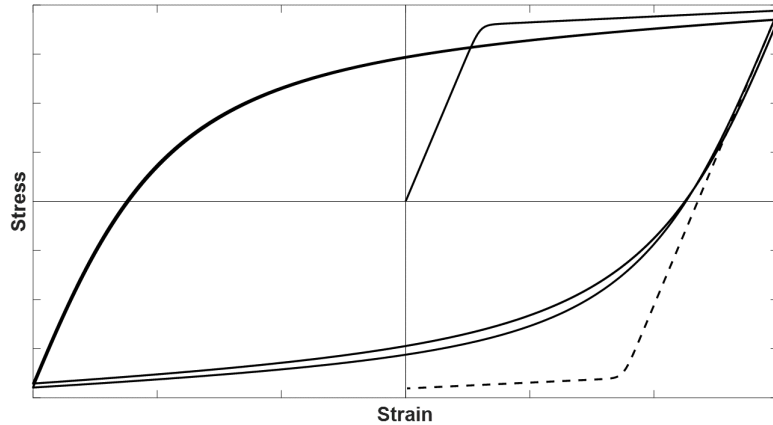
Fig. 4.5 Menegotto-Pinto uniaxial constitutive model for steel

The parameter R introduces the Bauschinger effect which improves significantly the accurateness of the results [79, 133, 198]. The microstructure of the material is modified when yielding stress is exceeded. This dislocation generates internal stresses that influences on the stres-strain behavior what is known as Bauschinger effect. Hence, the yield strength is lower for reversed loading direction when yielding limit is overtaken as it is showed in Figure 4.5.

The used model considered isotropic hardening by shifting the position of the yield asymptote. Although this research focused on static loading, the model allows to achieve an accurate representation of the hysteretic behavior. The line is moved parallel to the initial direction based on the maximum plastic strain and it is reported as [56]:

$$\sigma_{sh} = \sigma_{y,0} \, a_3 \left(\frac{\varepsilon_{max}}{\varepsilon_{y,0}} - a_4 \right) \tag{4.34}$$

where a_3 and a_4 are material experimentally determined parameters and ε_{max} is the maximum absolute strain at the instant of strain reversal.

Figure 4.6 illustrated the flowchart of the constitutive model. After initializing variables ($\sigma_r = \varepsilon_r = 0$), it is determined if the loading direction is the same as in the previous loading step. In case of changing the loading direction, the isotropic strain hardening is determined by computing the new isotropic line (σ_{sh}). Subsequently, the loading direction is identified (tensile or compression) and the coordinates of the intersection point of the two asymptotes are defined (σ_y, ε_y). Once these variables are defined, the stress state can be calculated (σ_n, ε_n). This procedure is repeated in every loading step.
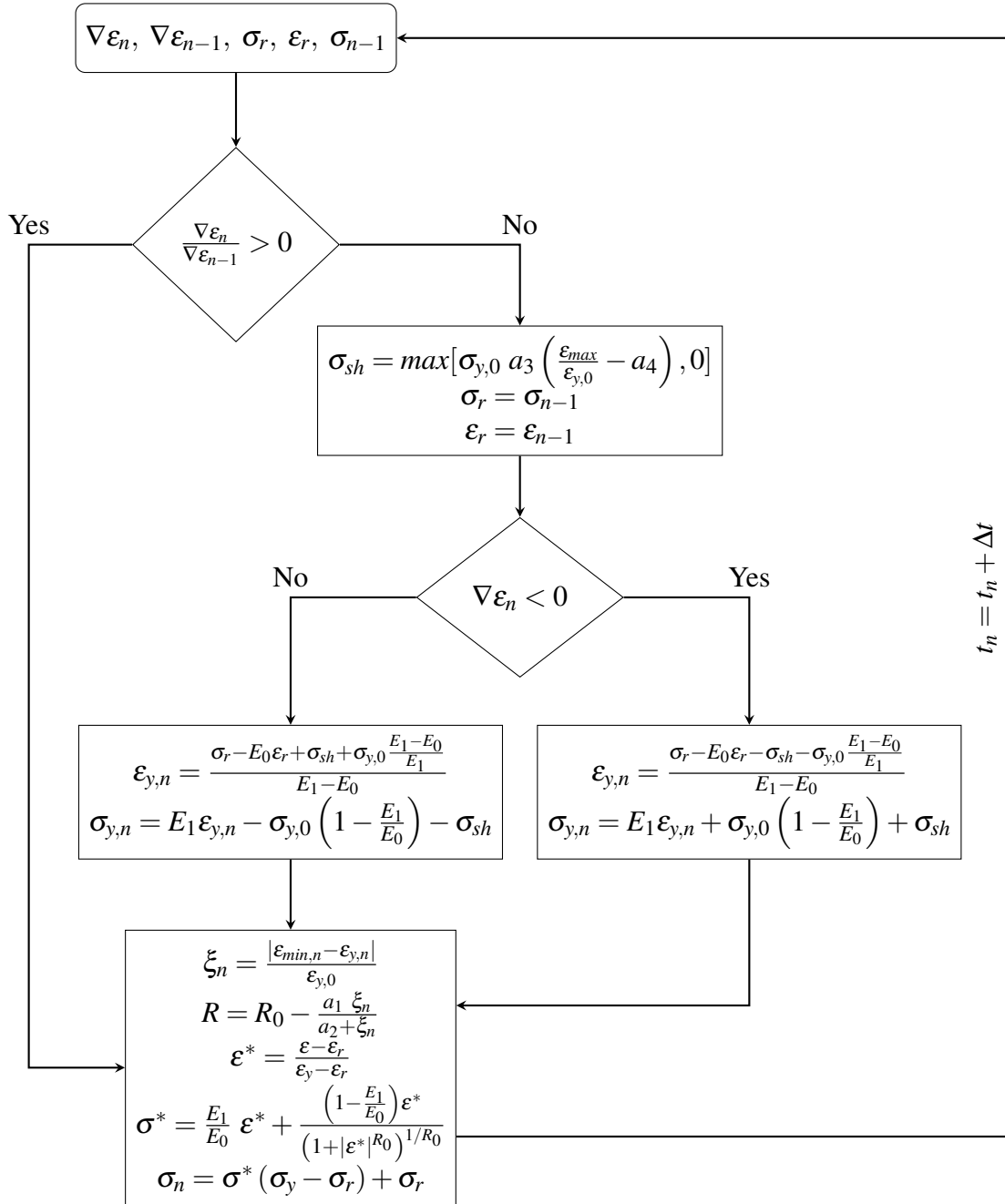
Fig. 4.6 Flowchart of the algorithm implemented for Menegotto-Pinto constitutive model

4.5   Validation examples

Experimental tests are reproduced in order to assess the ability of the proposed models to capture material failure phenomena in concrete elements with or without fibers. The traditional reinforcements is also modeled and validated. In order to reduce significantly the

computation time, a two-dimensional numerical models are implemented in the in-house code.

4.5.1   Interface element: Damage model for concrete

The capability of interface elements to model concrete brittleness is validated by means of a three-point bending beam subjected to a vertical load [101]. The geometrical dimensions of the beam are indicated in Figure 4.7(a). A weakness is introduced by a notch at its middle section to establish a starting point for the crack. The tensile damage model explained in Section 4.3.2 is applied to model concrete degradation and predict crack propagation. The required inputs to define material parameters are shown in Table 4.3. As the beams is not susceptible to buckling or torsion, plane stress condition is assumed.

Table 4.3 Material parameters used in the validation of brittle fracture

Bulk elements	
Young's modulus	38.5×10^3 MPa
Poisson's ratio	0.24
Interface elements	
Young's modulus	38.5×10^3 MPa
Poisson's ratio	0
Tensile strength	3.6 MPa
Fracture energy	0.05 N/mm
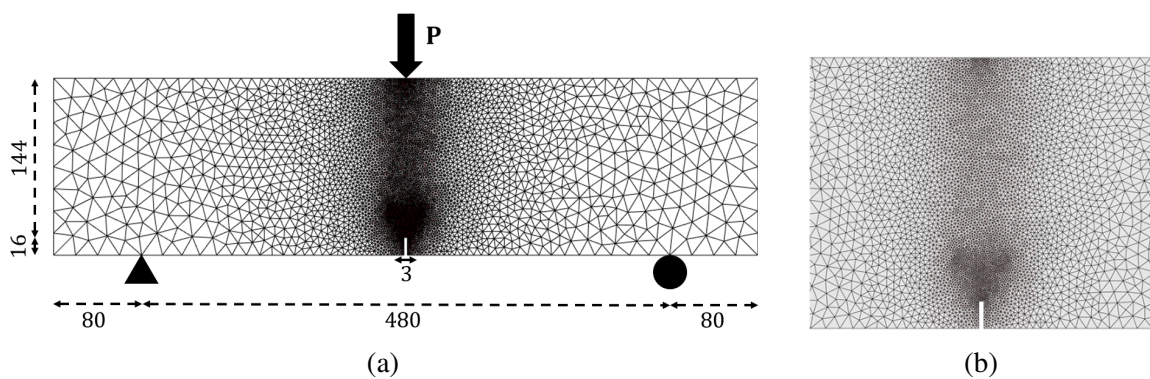
Fig. 4.7 Three point bending beam (a) Geometry and boundary conditions (b) Refined mesh

As regards the mesh, linear triangular 2D elements are used to define the unstructured grid. Figure 4.7(b) shows the refinement in the central area where the cracks are expected

due to the existence of the notch, thus increasing fidelity there. In the central area element height of 1 mm is adopted and the rest of the beam is meshed with elements of 15 mm of height. Different interface elements are introduced between the bulk elements, the height of the introduced interface elements are 0.001 and 0.01 mm. In principle, the accuracy of the solution is not influenced by the element size as the load step size do.
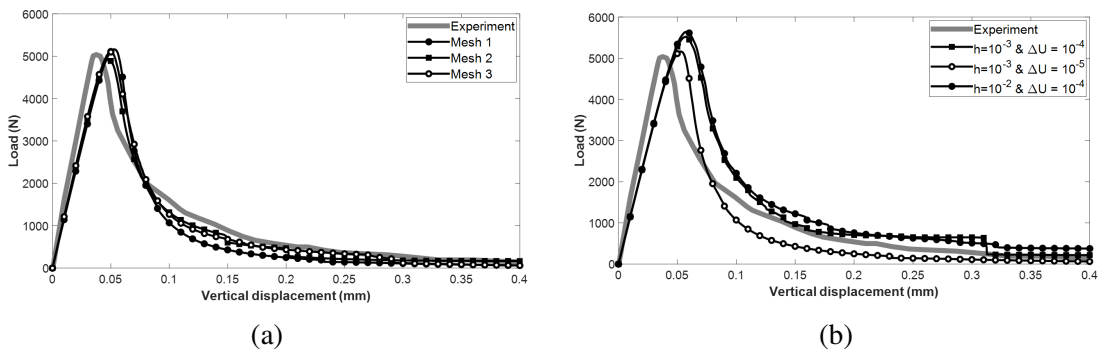
Fig. 4.8 Load/displacement curve obtained with (a) Different mesh (b) Different interface height and pseudo-step

Figure 4.8 shows the experimental and predicted structural responses. The load/displacement evolutions are compared to demonstrate the ability of the model. In Figure 4.8(a) are simulated three meshes with different refinement in the center area of the beam. The used element size are 1 mm, 2 mm and 3 mm for Mesh 1, Mesh 2 and Mesh 3 respectively. The best results are calculated with Mesh 1 but it is observed that the three meshes fit very well with the experimental results.

Figure 4.8(b) shows the role that plays the pseudo-time step size and the height of the intermediate elements on the accuracy of the results. Three simulations are carried out with the same mesh and different interface height and pseudo-time step length. Interface degradation is better approximated with smaller interface height. Nevertheless, the used IMPL/EX algorithm is more sensible to pseudo-step length.

Crack growth can be modeled through interface elements. Figure 4.9 illustrates the development of the crack and damage level (0-1) of each element at different loading steps. As concrete is a brittle material, the crack spreads with hardly plastic deformation. Interface elements damage increases from 0 (undamaged) to 1 (damaged) in few loading steps. The damaged elements are located close to the crack due to the nature of the material, the damage are not spread along the beam.
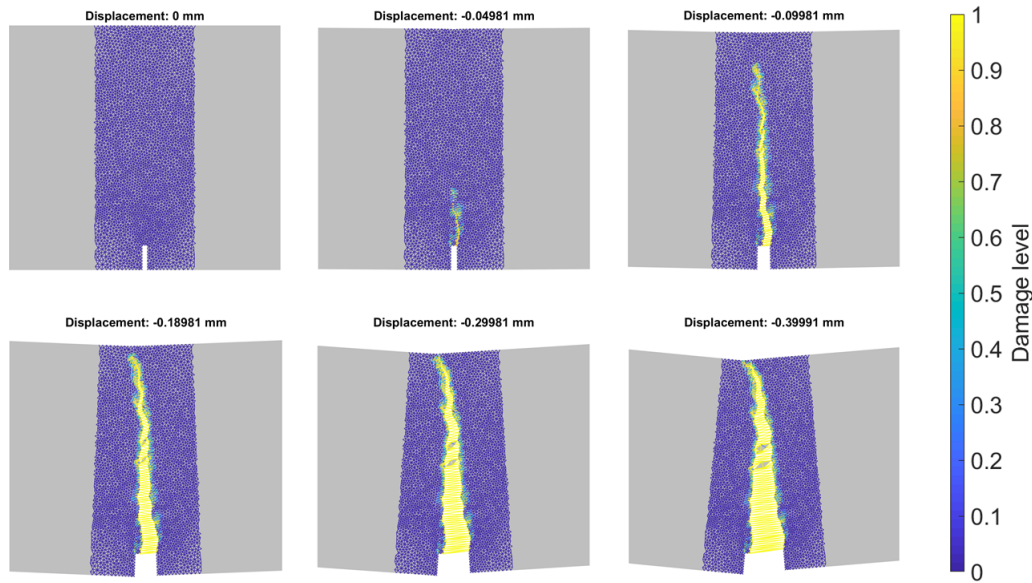
Fig. 4.9 Crack growth simulation and damage level of interface elements

4.5.2   Interface element: SFRC (Bridging effect)

The scope of interface element to simulate the bridging effect due to the addition of steel fibers is studied in this point. In order to carry out this analysis, three-point notched beam is simulated [201]. The notched beam is loaded up to failure to evaluate the bridging effect of the fibers. It is worth noting that the bridging effect is evident after the concrete is cracked. Instead of showing a softening behavior after the cracking, SFRC elements shows a hardening behavior which depends on the characteristic of fibers.
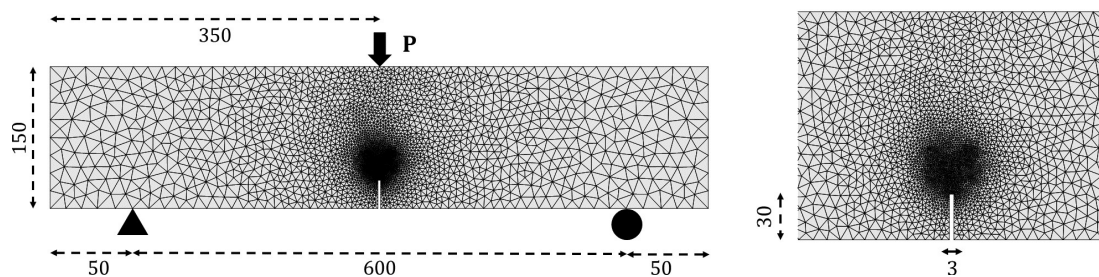
Fig. 4.10 SFRC beam geometry

The geometry of the model is defined in Figure 4.10. The length of the notched beams is 700 mm and the span is 600 mm. The cross section of the beam is square of 150 mm. The notch is located in the center of the span to facilitate the crack development. The height of the notch is 30 mm and the initial opening is 3 mm.

Table 4.4 Material parameters used in the validation of SFRC

Bulk elements	
Young's modulus	41.61×10^3 MPa
Poisson's ratio	0.2
Tensile strength	4.75 MPa
Tensile fracture energy	0.13 N/mm
Interface elements	
Young's modulus	210×10^3 MPa
Poisson's ratio	0
Tensile strength	1,100 MPa
Fiber length	60 mm
Fiber diameter	0.75 mm
Volume content	7.69×10^{-3}
Shape	Hooked-end

The beam is meshed with triangular elements of 20 mm, while near the notch 1 mm elements are used to capture the fracture. Intermediate element of 0.001 mm are inserted in the middle part of the beam, where the development of cracks is foreseen. As regards boundary conditions, the vertical and horizontal displacement are restricted in the left support, while the vertical displacement is only restricted in the right support.

The damage model explained in Section 4.3.3 is implemented in the FEM to simulate the bridging effect. The inputs required by the constitutive models are reported in Table 4.4. The bulk elements are assumed as linear elastic elements. The introduced Young's modulus is calculated based on the elastic modulus of the concrete and the fibers. The inputs of the interface elements are mainly determined by the fibers. In this case hooked-end fibers are added to increase the toughness.

Figure 4.11 compares the results of the simulation with the experimental data. The shaded area indicates the experimentation results range, while the continuous line represents the results obtained by the simulation.

The numerical results of plain concrete is printed in dotted line, in such way it is made visible the effect of the fibers. Until the cracking takes place in the first peak, the behavior of plain concrete and SFRC are very similar due to the slight impact of the fibers on the Young's modulus. However, the value of the maximum peak, which mainly depends on the tensile strength, varies slightly. The steel fiber increases the tensile strength from 4.75 Mpa to 4.83 MPa.
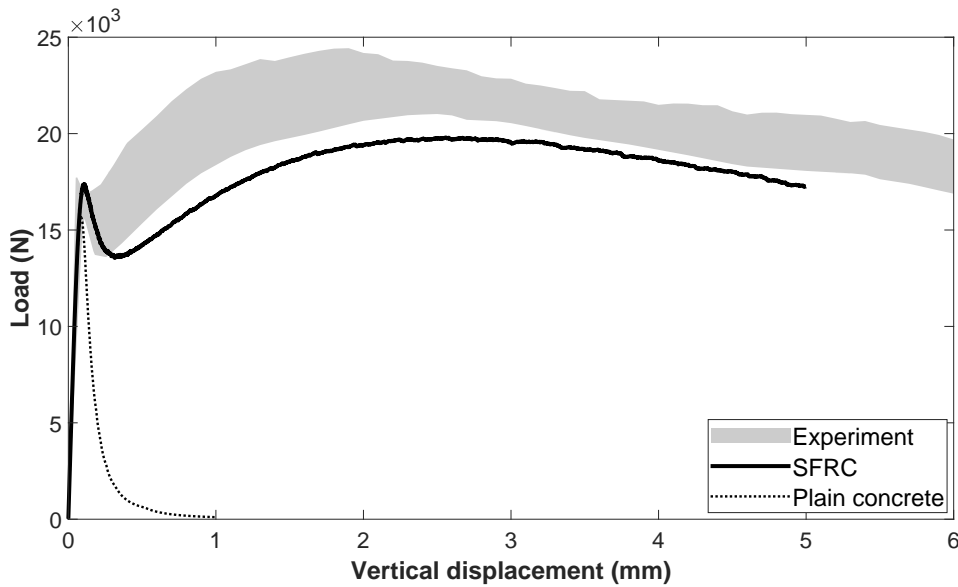
Fig. 4.11 SFRC beam Load/displacement curve

After the crack is generated, the effect of the fibers are more evident. Plain concrete simulation shows a completely softening behavior, while SFRC experiences a hardening behavior. This behavior depends on the properties of the fibers and the amount of them. After the first peak, there is a drop where the crack is generated and the fibers starts working. The stresses are transfered through the fibers until they are broken or pulled off.

The numerical model is able to capture the ductility gained by the addition of fibers. Despite the curve is not within the experimental range, it can be considered that the numerical model simulate satisfactorily the real behavior. Therefore, it can be assumed that the constitutive model is well implemented in FEM code.

4.5.3 Reinforced concrete: Reinforcement bars

The three-point bending beam reported by *Ruiz et al.* [147] is modeled to validate the model for steel reinforcement bars. The dimensions of the beam are 1350 x 300 x 50 mm and the detailed set up is shown in Figure 4.12. The beam is meshed with triangular elements of 10 mm and it is remeshed in the central zone with elements of 5 mm. The beam is modeled as a 2D plane-stress problem, while the reinforcement bars are considered 1D element and perfectly bonded. Four steel bars of diameter 2.5 mm each reinforces the beam longitudinally.

Three types of material are assumed in the model and the material parameters are reported in Table 4.5. Linear-elastic model is implemented to model bulk elements. In the central zone, which is subjected to the largest value of bending moment, interface elements are introduces. They are modeled through a damage model for plain concrete. In this beam is not added any
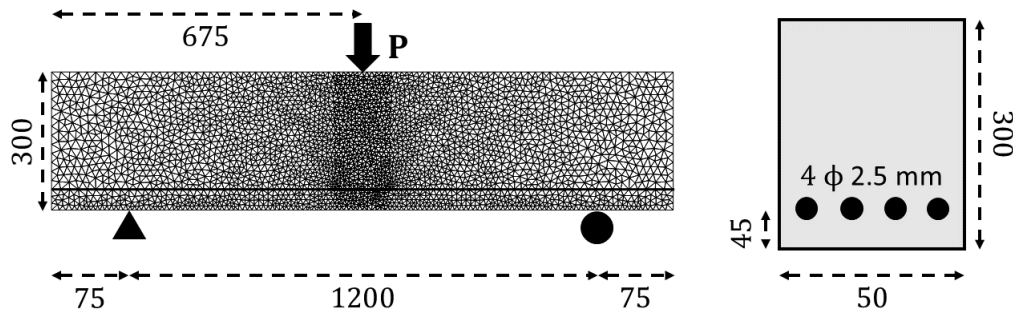
Fig. 4.12 Reinforced concrete geometry and cross section

Table 4.5 Material parameters used in the validation of brittle fracture

Bulk elements	
Young's modulus	29×10^3 MPa
Poisson's ratio	0.2
Interface elements	
Young's modulus	29×10^3 MPa
Poisson's ratio	0
Tensile strength	3.8 MPa
Fracture energy	0.0625 N/mm
Reinforcement	
Young's modulus	162×10^3 MPa
Tensile strength	587 MPa
Section	19.63 mm^2
Strain hardening ratio	0
R_0	20
a_1, a_2, a_3 and a_4	0, 0, 18.5 and 0.15

fiber. The bar is discretized as it is explained in Section 4.4.1 and the Menegotto-Pinto model is applied to model the behavior of the steel.

Figure 4.13 compares the experimental results determined in [147] with the calculated numerical results (reinforced concrete and plain concrete). The numerical curves bears a very close resemblance to the real behavior during the prepeak stage. At the end of this stage
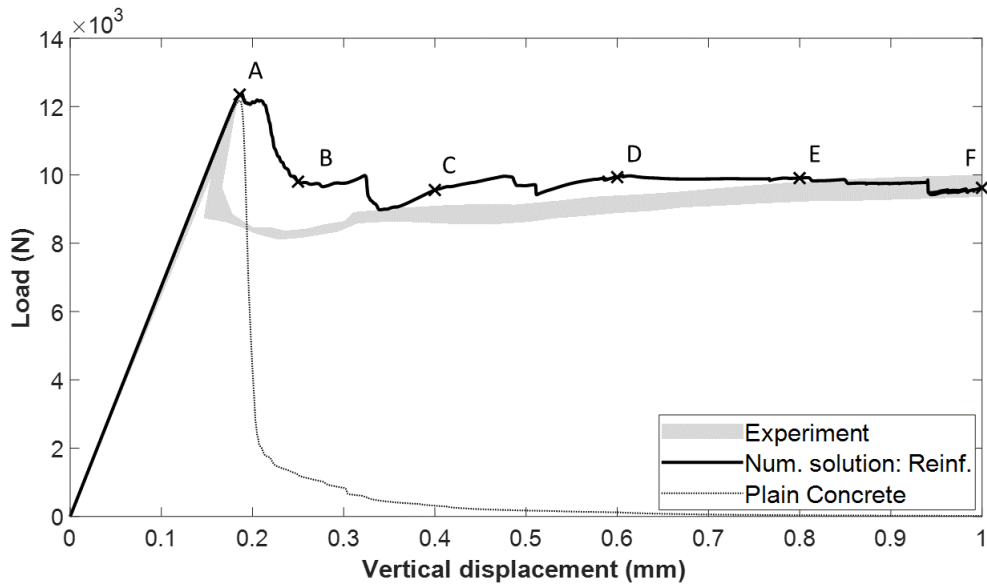
Fig. 4.13 Reinforced concrete beam load/displacement curve

(Point A), the crack is generated as can be shown in Figure 4.14. Despite there is a slight difference with the experimentation, the load drop just after the generation of the crack can also be assumed as captured by the numerical model. Beyond this point the experimental range and the numerical curve are again quite close. In this branch the concrete is degraded and the slope of the structural curve depends strongly on the reinforcement.
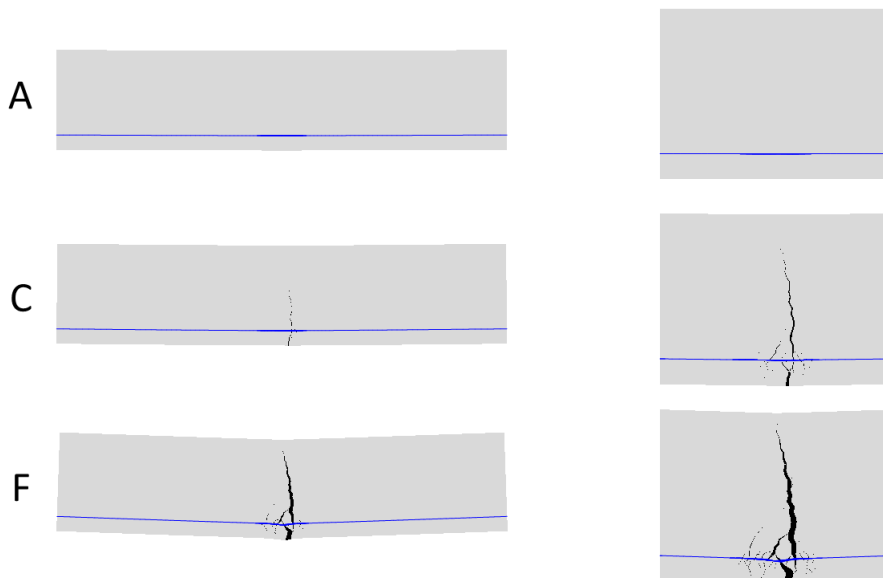
Fig. 4.14 Crack development at stages A, C and F
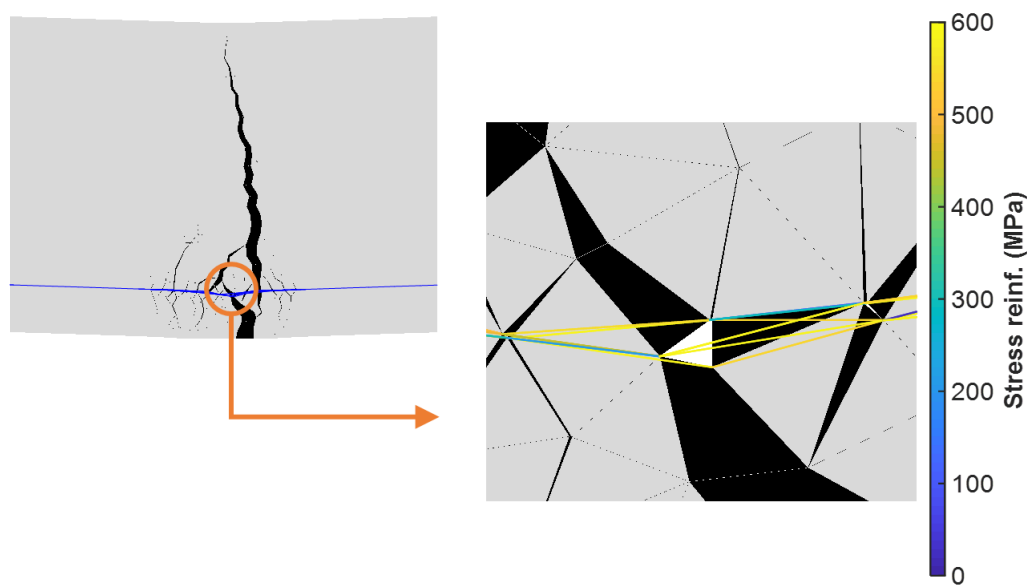
Fig. 4.15 Reinforcement bars discretization (Point F)

After Point A the beam is loaded up to failure occurs and the development of the crack is more visible as it is reported in Figure 4.14. The crack is developed in the central zone of the beam where interface elements are introduced to capture the damage of the procedure. In this zone, it is also discretized the steel bar as it is reported in [167]. Figure 4.15 gives an overview of the framework that shapes the reinforcement bars while the crack is developed. The black color elements are the interface elements and they model the crack. The linear elements of different colors are the steel bars and it can be seen how they have been strained. In this zone the bars are divided into elements with smaller cross-section to allow the crack crossing the steel bars. The numerical model enables also to know the stress state of the bars. This aspect requires an indepth study due to the selected discretization method applied. The stress state of the divided bars, which in the reality are just one element, are different and it results in bars with different stress state.

Figure 4.16 shows the evolution of the damage level of the interface elements throughout the chosen stages (see Figure 4.13). The crack development differs markedly from plain concrete beams to reinforced concrete beams. In the case of plain concrete elements, all the damage is localized in a narrow band and one main crack is developed (see Figure 4.9). However, Figure 4.16 reports the propagation of the main crack as well as the development of an orthogonal microcracks in the concrete surrounding the reinforcement bar. Therefore, the damage developed in two planes during the loading. Initially the damage is mainly developed in a narrow band as it is plain concrete. Afterwards, the advance direction of the damage is

more evident around the bar. The developed microcracks between the bar and concrete bulk causes the debonding of the reinforcement.
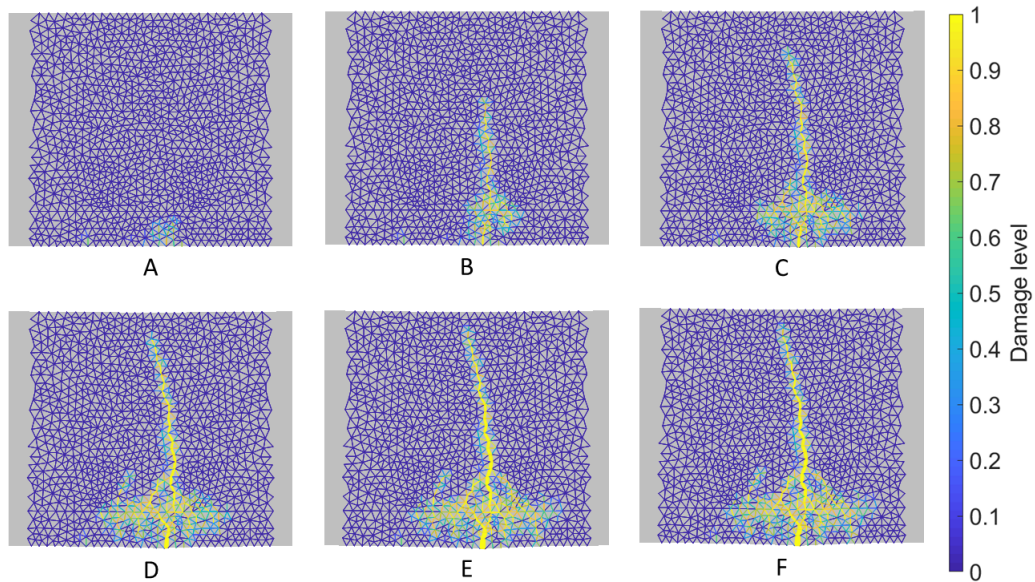
Fig. 4.16 Reinforced concrete beam damage development at different stages

4.6   Conclusions

In this chapter the implemented numerical model is presented and its suitability to simulate different structural elements are studied. The constitutive models (damage and elastoplastic models) are presented and its implementation in the developed in-house code is studied through flowcharts. Furthermore, the inputs needed by the numerical models are identified. This predetermines the testing to be carried out to characterize mechanically the material. The inputs required by the constitutive models for each material are:

- **Concrete:** Young's modulus, Poisson's ratio, tensile strength and fracture energy.

- **Steel fibers:** Young's modulus, tensile strength, fiber content and fiber geometry (length, diameter and shape).

- **Steel bars:** Young's modulus, tensile strength, and cross-section.

Interface elements are used to model the degradation of the concrete and the bridging effect due to the addition of the steel fibers. The introduction of these high aspect ratio elements requires changing the discretization of the reinforcements bar. Both points are

implemented in the in-house code. The finite element model is validated through bibliograph-ical results, which enables to consider the numerical tool as valid to model plain concrete, SFRC and reinforced concrete.

Chapter 5

Materials and experimentation

5.1 Introduction

This chapter focuses on the studied concrete mixes and the tests carried out to evaluate the performance of the material. Concrete dosage and the fiber content of studied four mixes are presented in the first part of the chapter. Regarding testing, the used methodologies are described and the measured parameters are presented. These measurements were the baseline to determine properties of the material to evaluate the performance of each mix in the next chapter and feed up the numerical algorithm.

5.2 Materials and fresh properties

In this research self-compacting, pumpable and EAFS made concrete were designed. The term self-compacting implies that concrete flows under its own weight and does not require external vibration. Pumpable means that concrete flows maintaining sufficient resistance to segregation. Nevertheless, the main innovation was the use of EAFS as aggregate to improve concrete properties. The subsequent points explains in more detail the characteristic of the constituents and the properties of fresh concrete.

5.2.1 Constituent materials of concrete

The research group has undertaken a thorough study on the mix proportions and the particularities of the EAFS concrete in the last years [12, 59, 151]. Based on the previous experience of the group four mixes were studied. An overall description of the used constituents to make concrete is provided in the following points.

CEMENTS

In the present study two commercial cements were employed to make the different mixes. In both cases Portland cement was partially replaced with blast furnace slag, which required adjusting the mix design. This replacement is due to environmental reasons and resource utilization.

- **CEM II/B-S 42.5R: Portland-slag cement.** It is a cement produced by fine grinding of clinker and granulated blast-furnace slag (30%). The value of 42.5 MPa refer to the minimal mortar strength at 28 days.

- **CEM III/B 32.5N: Blastfurnace cement.** It is a cement produced by fine grinding of clinker and granulated blast-furnace slag (70%). The cement strength was 32.5 MPa at 28 days.

AGGREGATES

Although limestones were used, the distinguishing factor of the applied concrete was the addition of EAFS as substitution of natural aggregate. The EAFS aggregates were obtained crushing slags produced at a certain stage of steelmaking in an electric arc furnace. They were characterized its angularity, density, chemical basicity and roughness and abrasion resistance [135]. Two different grading were adopted for EAFS aggregates 4-12 mm (medium aggregate) and < 4 mm (fine aggregate). EAFS contains basically no fine particles and they were mostly gravel and sand sized. The specific mass of EAFS aggregates were higher than that of the natural aggregates as a consequence of the iron content. This characteristic gives rise to aggregate segregation problems, which complicate achieving the desired conditions (pumpable and self compacting). This problem was solved by the addition of fine limestone aggregates and admixtures.

Limestone fine aggregate were added to fill up voids between the aggregate particles and increase the cohesiveness of the paste [151]. The addition of limestone aggregate also improved the general performance of concrete [41]. The used limestones came from a quarry of the north of Spain. It is composed of a 95% of calcite and its specific density was 2,670 kg/m^3 [153, 151].

In sum, the provided aggregates were EAFS with specific density equal to 3,420 kg/m^3 and water absorption equal to 1.12%. They were divided in two fractions 4-12 mm and <4 mm, which were mixed with limestones (<1.2 mm) in order to produce the correct gradation [151]. Figure 5.1 illustrates the granulometric curves of the used aggregates. More details of the used aggregate can be found in [153, 151, 152]

Fig. 5.1 Grading curves of aggregates

ADMIXTURES

The development of higher performance and self-compacting concretes has been possible thanks to the use of admixture. They have become an integral part of modern concrete. This kind of admixture decrease water content while improves the mechanical properties and workability of concrete [207].

However, not all admixtures are compatible with every cement or fine aggregate [2]. The role of superplasticizers is dispersing cement grains, which can cause flowability problems, anomalous rheological behavior or just, not achieving the desired properties [35]. Cement-admixture compatibility is the result of both materials and depends on factors such as mineralogical composition of aggregates, fineness, chemical and structural composition of admixtures etc [35, 40, 115].

In this study a polycarboxylate-based admixture was used to reduce the w/c ratio. The used admixtures was provide by CHRYSO for 2T, 2S and 2M mixtures and its compatibility was studied in [151]. In the instance of 3M mixes, admixtures from the company BASF were applied.

WATER

Tap-water was used and thw w/c ratios of concrete were established experimentally [151]. The values of w/c ratio for 2T, 2M, 2S and 3M were 0.51, 0.54, 0.56 and 0.45, respectively.

5.2.2 Steel and synthetic fibers

The absence of vibration of self-compacting concrete allow adding fibers without influencing its random placement. In the present study, fibers were used to improve mainly fracture toughness, thus they may have also affected negatively the flow and segregation of the fresh mixtures [52, 94]. In this study, two types of fibers were used synthetic fibers and steel fibers. The geometry and material properties of the fibers are defined in Table 5.1.

Table 5.1 Concrete mix proportion (Kg/m^3)

	Steel fibers	Synthetic fibers
Type	hooked-end	dimpled-surface
Length (mm)	35	35
Diameter (mm)	0.55	0.93
Tensile strength (MPa)	1,200	> 400
Young's modulus (GPa)	210	> 6
Number of fibers per kg	15,300	32,895
Density (kg/m^3)	7,900	910

Synthetic fibers were made of polyolefin, which were designed to resemble the postcracking behavior of concrete with low contents of steel fibers [70]. The main advantage over steel fibers is its performance in fresh state. Nevertheless, the weak point are the law Young's modulus, in this study it was 35 times lower; and the low frictional resistance [5]. In this study, 4.5 kg/m^3 were added in the mixture containing synthetic fibers, about 0.5% of the total volume.

Approximately 0.5% of volume was added of in mixes with hooked-end steel fibers. The hooked-end shape improves the bonding features (a kind of anchoring effect) and increased material stiffness. Steel fibers improve the behavior beyond the elastic state and the toughness, reducing crack width and spreading the damage along the structural element.

5.2.3 Designed concrete mixes

The performance of four mixtures were analyzed in this research. Table 5.2 detailed the dosage of each mix. The main difference between the mixtures were the type of cement and the addition of fibers. In order to facilitate the monitoring and identification of the mixes, the adopted nomenclature was:

- **2T:** CEM-II, without fibers and self-compacting.

- **2M:** CEM-II, with steel fibers and self-compacting.

- **2S:** CEM-II, with synthetic fibers and self-compacting.

- **3M:** CEM-III, with steel fibers and pumpable.

Table 5.2 Concrete mix proportion (Kg/m^3)

	2T	2M	2S	3M
CEM II/B-S 42.5R	330	330	330	-
CEM III/B 32.5N	-	-	-	350
EAFS: ϕ = 4-12 mm	750	750	750	930
EAFS: ϕ < 4 mm	550	550	550	690
Limestone: ϕ < 1.2 mm	950	950	950	650
Water	170	180	185	160
Admixture	5.3	5.3	5.3	4.9
Steel fibers	-	40	-	30
Synthetic fibers	-	-	4.5	-

5.2.4 Fresh state characterization

Concrete can be considered self-compacting or pumpable when, in fresh state, it meets the required flowability, viscosity, segregation resistance and passing ability. These conditions were defined by the type of application or performance such as concrete element geometry, placing equipments, confinement conditions, etc. Table 5.3 presents fresh state properties of the mixes.

(a) Self-compacting concrete (b) Pumpable concrete

Fig. 5.2 Abrams cone test

Slump-flow test was carried out by Abrams cone to evaluate the flowability as it is illustrated in Figure 5.2. The two diameters of the spread, perpendicular to each other,

Table 5.3 Mixes fresh state characterization

	2T	2M	2S	3M
Spread (mm)	720 (SF2)	650 (SF1)	620 (SF1)	-
Slump (mm)	-	-	-	175 (S4)
Fresh density kg/m^3	2,710	2,670	2,600	2,710
Occluded air (%)	2.2	2.0	1.9	3.6

were measured and the average of both measurements was used to evaluate the flowability according to EFNARC [171]. Mixes with fibers (2M and 2S) were classified according to their diameters as SF1 (550-650 mm), while 2T was cataloged as SF2 (660-750 mm). Although fiber content affect the flowability, it was possible to achieve self-compacting conditions.

Pumpability was also evaluated using Abrams cone, but in this case the slump was measured. Pumpability is related to concepts as consistency or segregation resistance and it is strongly conditioned by the placing method and coarse aggregate. The friction inside the pipe, when concrete is being pushed, can cause segregation problems. Coarse aggregate graze pipe walls while fine aggregates lubricate the walls. Hence a special attention must be paid to the grading curve. In this research 3M was designed as pumpable mix and it was classified as class S4 (160-210 mm) according to the Spanish Structural Concrete Code (EHE-08).

Air content is another factor that affect the cohesiveness and consistency of concrete. Low entrapped air content provide better flowability conditions [154]. As it was expected, 3M entrained higher volumes of air and the other mixes results were low enough to be considered as acceptable.

These results were completed with a visual inspection during the test, which gave information about the segregation conditions. It was not seen any anomaly therefrom had not be rejected.

The values of the density were on the order of 2,700 kg/m^3 for all the mixes. They were heavier than a conventional concrete, whose density is on the order of 2,400 kg/m^3, owing to the greater weight of EAFS.

5.3   Methodology and measurements

The tests were carried out at the Laboratory of Large Civil Engineering Structures of the University of Burgos (E.P.S. campus La Milanera). The following points present an approach of the tests and how they were conducted.

5.3.1   Compression test

The compression test was carried out following the norm UNE-EN 12390-3:2009 [177]. Compressive strength was measured by breaking cylindrical specimens and cubes in a compression-testing machine at different ages, as the ones showed in Figure 5.3. The compressive strength and the elastic modulus were calculated for each specimen. Compressive strength was calculated from the failure load divided by the cross-sectional area and the elastic modulus was determined as it is explained in UNE-EN 12390-13 [176].

(a) Cube: 100 x 100 x 100 mm   (b) Cylinder: ϕ100 x 200 mm

Fig. 5.3 Compressive strength test specimens

The compression test consisted of applying an initial compressive load up to 30% of the failure load. Afterwards, the sample was loaded constantly at range of 0.6 ± 0.2 MPa/s until failure. Table 5.4 presents the compressive strength at different ages (7 days, 28 days, 90 days and 1 year). The tested specimens were cubes with an edge length of 100 mm and cylinders with diameters of 100 mm and lengths of 200 mm. There was not any correction factor applied to convert the cube strength result into an equivalent cylinder result.

Similarly, the elastic modulus were calculated using the same test. The tests were preloaded up to 5% of failure load to ensure the alignment and stability of the sample. Thereafter, the elastic modulus was calculated based on stress difference and strain difference.

Table 5.4 Compression test results (MPa)

Type	7 days	28 days	90 days	1 year	Young's modulus
2T	48.16	65.69	78.18	76.89	40,917
	46.02	59.04	72.44	76.59	39,540
		54.24			40,059
2M	38.47	53.91	61.05[1]	72.48	36,082
	37.48	51.41	66.21[1]	65.01	33,143
		53.94			34,938
2S	33.34	45.65	60.59[1]	62.39	30,505
	33.18	45.36	53.09[1]	58.52	32,175
		47.24			32,101
3M	19.90	28.81	32.90	38.96	26,304
	20.10	27.28	34.51	37.26	26,212
	20.48	26.12	32.34		25,624

[1] Cube: 100x100x100 mm.

This time, the difference was calculated between 5% and 30% of the failure load as it is indicated in Table 5.4.

$$E_{sec} = \frac{\Delta\sigma}{\Delta\varepsilon} = \frac{\sigma_{30\%} - \sigma_{5\%}}{\varepsilon_{30\%} - \varepsilon_{5\%}} \qquad (5.1)$$

5.3.2 Indirect tensile test

Indirect tensile testing of concrete, also known as Brazilian test, is a well-known and common method for determining indirectly the tensile strength. The test was carried out in accordance with UNE-EN 12390-6:2010 [178] and the tensile strength was calculated using Equation 5.2, also explained in [178].

$$f_t = \frac{2P_{max}}{\pi\phi L} \qquad (5.2)$$

where, P_{max} is the maximum loading, ϕ is the diameter of the cylinder and L is the length of the cylinder.

The samples were subjected to compressive loads as it is shown in Figure 5.4. Before starting the testing, the sample was loaded up to 20% of the ultimate load to center it.Then, the load was increased until failure at a constant rate between 0.04-0.06 MPa/s. The failure

Fig. 5.4 Indirect tensile test

initiates at the center of the core and propagates outward along the loading direction. The tensile stress was defined as the perpendicular stress to the loaded diameter at the center of the cylinder. Tensile strength was calculated with the applied force at the time of failure (P_{max}) and the sample dimensions (ϕ: Diameter, L: Length).

In this research, three samples were tested for each mixture of concrete. The dimensions of the cylindrical specimens were ϕ 150 x 300 mm. Table 5.5 lists the maximum load measured for each specimen.

Table 5.5 Tensile strength determined through Brazilian test (MPa)

	2T	2M	2S	3M
Sample 1	4.93	5.36	3.94	3.78
Sample 2	4.68	5.03	4.44	3.23
Sample 3	5.70	4.12	4.66	3.05

5.3.3   Uniaxial tensile test

Direct tensile test were done to evaluate the tensile strength and the tensile elastic modulus of concrete. There is hardly any norm to follow during the test because concrete tensile capacity was almost always dismissed. *K. Wille et al.* [194] made a review of different types of specimens to study the direct tensile strength and suggested possible dimensions of a dog-bone sample. In this research, a dog-bone mold was designed based on this dimensions and the characteristic of the jaws of the laboratory. The tested specimens had a length of 164.1 mm and a cross section of 30 x 30 mm. Figure 5.5 illustrates in more detail the size of the designed specimen and the mold printed in a 3D printer.
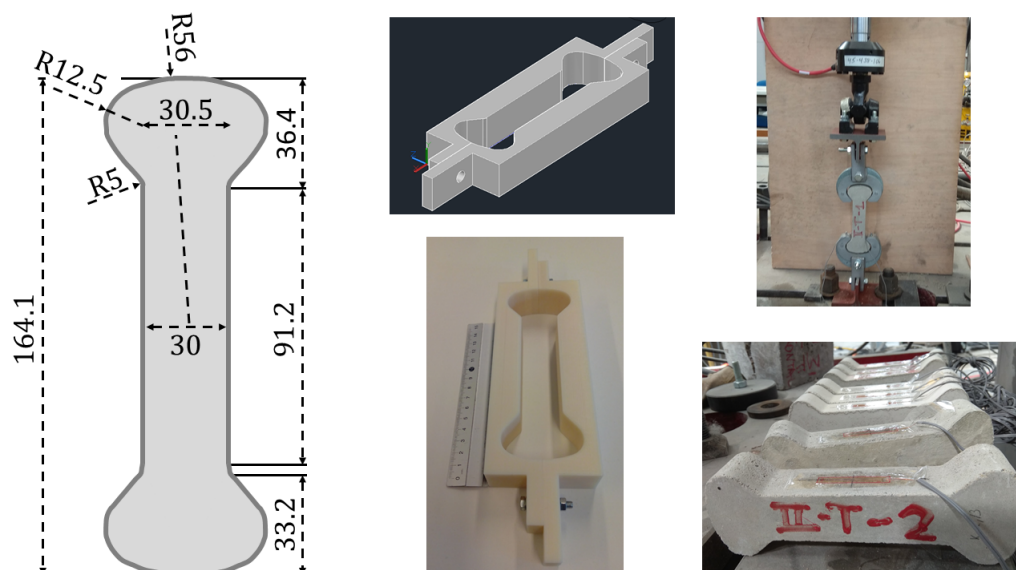
Fig. 5.5 Dog-bone design and set up

Three samples were tested for each mixture of concrete as shows in Figure 5.5. The samples were preloaded in 6 cycles of loading/unloading to ensure the alignment and calculate the Elastic modulus. The loading rate was 0.05 kN/seg up to load of 0.5, 0.75, 1, 1.5, 2, and 3 kN respectively. Afterwards, they were loaded up to complete failure.

The failure mode of mixtures without fibers showed a brittle behavior when they were loaded to beyond its ultimate tensile strength. Mixtures with fibers, specially the ones with steel fibers, showed a ductile behavior; firstly, collapsed concrete and then, the fibers.

Load and displacements were measured using strain gages on two sides. Table 5.6 summarizes tensile strength and Young's modulus of each sample. On of the samples of the mix 2T was rejected due to its abnormal behavior.

Table 5.6 Direct tensile test results: Tensile strength (MPa) and Modulus of elasticity (GPa)

		2T	2M	2S	3M
Sample 1	Tensile strength	4.37	3.79	3.74	2.96
	Young's modulus	39.2	35.0	35.2	32.2
Sample 2	Tensile strength	4.13	4.19	4.02	3.23
	Young's modulus	37.8	40.5	35.7	32.4
Sample 3	Tensile strength	2.55*	3.34	3.22	3.25
	Young's modulus	37.7*	38.2	35.6	32.2

* Rejected samples.

5.3.4 Flexural strength test

Four-point flexural test was carried out within the framework of UNE-EN 83509 and UNE-EN 83510 [182, 183]. The tested specimens size dimension was 400 x 100 x 100 mm. The span was 300 mm and the distance between the loading rollers was 100 mm as suggests the cited norm. The beams were loaded with constant rate between 0.8-1.2 MPa/min through two loading rollers as it is illustrated in Figure 5.6. They were loaded up to the complete failure.

Fig. 5.6 Flexural test setup and failure

(a) 2T

(b) 2M

(c) 2S

(d) 3M
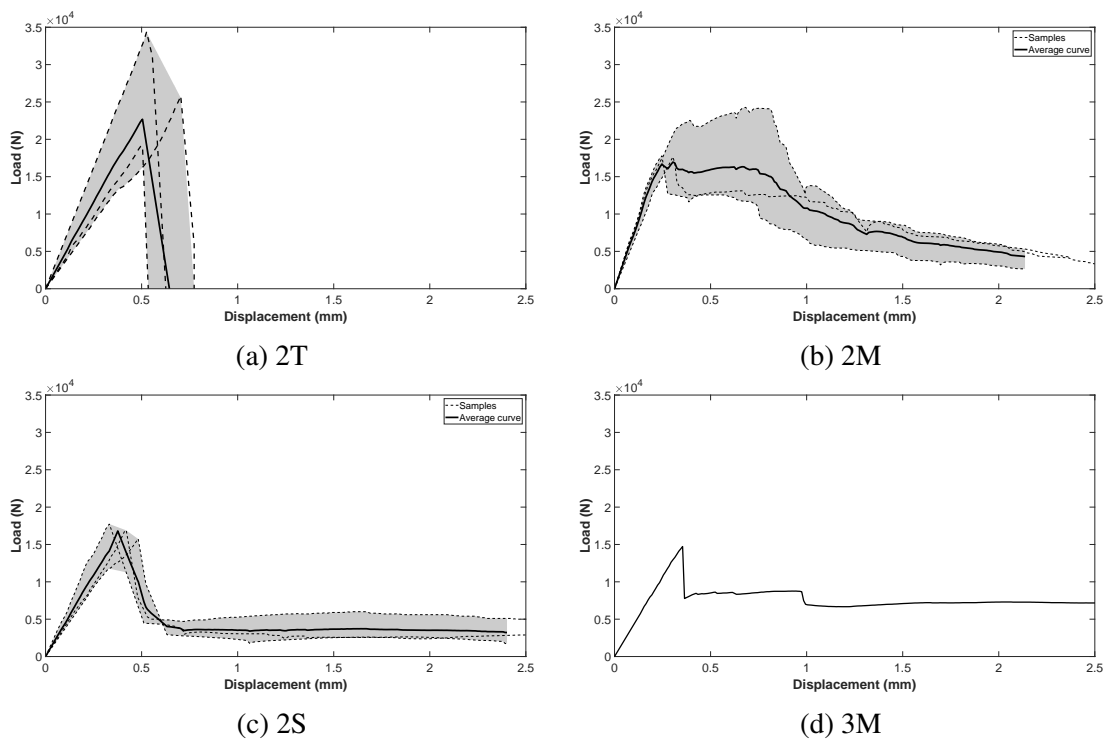
Fig. 5.7 Flexural test results of the different mixtures

Three samples were tested for each mixture with the exception of 3M mixture, where only one specimen was tested. Figure 5.7 shows the load/displacement curves of the samples. A representative curve was also drawn based on the tested samples results. The shaded area enclosed by the curves states the range of the behavior of the specimens. This test is used to evaluate the ductility of the mixtures. Flexural strength, first crack strength, toughness and fracture energy were defined from these tests as in [182, 183] is explained.

5.3.5   Notched beam test
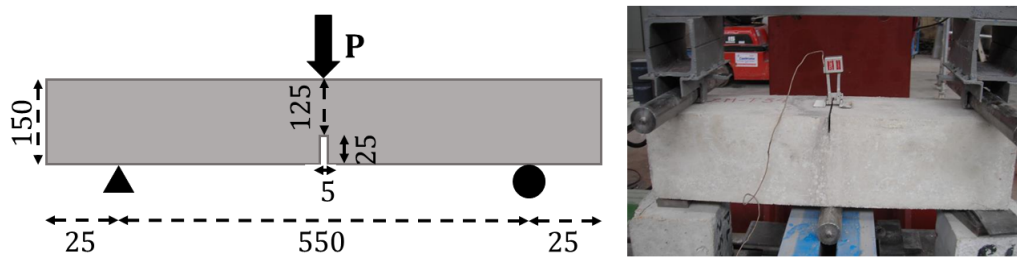
Fig. 5.8 Notched beam set up

(a) 2T

(b) 2M

(c) 2S

(d) 3M
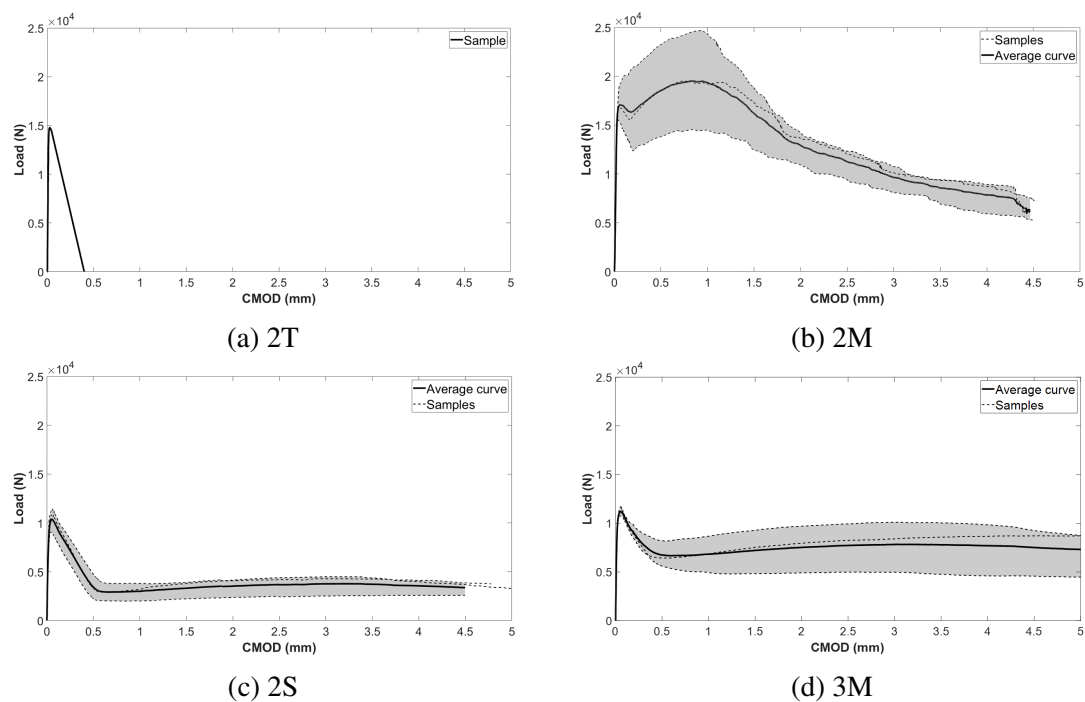
Fig. 5.9 Load-CMOD curve of tested notched beams

Three-point beams were carried out based on UNE-EN 14651 [180] to evaluate mainly the residual stress. The beams were 150 x 150 x 600 mm and the notch was done at the center

of the beam. The notch crossed transversally the beams and its height and width were 25 mm and 5 mm respectively. The span was 550 mm and it was loaded constantly in a middle point. Figure 5.8 shows the set up of the test. Three samples were tested for each mixture, with the exception of plain concrete mixture (2T).

In these test, CMOD (Crack mouth opening displacement) was measured while the beam was loaded as it is shown in Figure 5.9. The loading velocity was defined by the development the CMOD. The opening speed of the notch was 0.05 mm/min up to a displacement of 1 mm and the 0.2 mm/min up to failure. The test was considered completed when a CMOD of 4 mm was overcome. Based on the measured data, limit of proportionality (LOP) and residual strengths were determined. In this instance fracture energy was also estimated, despite the deflection was not measured. The vertical displacement was estimated based on CMOD through the equation given in [180].

5.3.6   Water penetration under pressure test
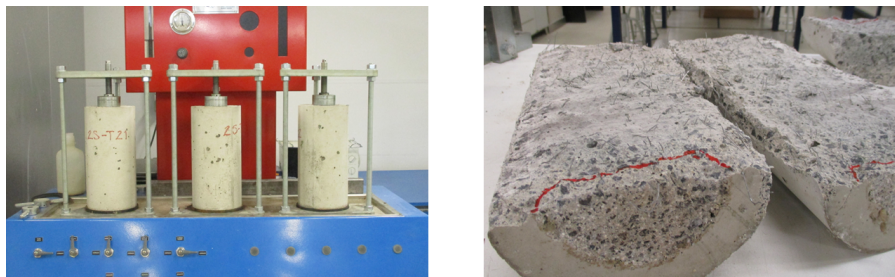
Fig. 5.10 Water penetration under pressure test set up and results

Table 5.7 Water penetration under pressure test results

		2T	2M	2S	3M
Area (mm^2)	Sample 1	891	1,034	1,827	4,580
	Sample 2	1,234	1,596	1,071	4,358
	Sample 3	961	1,380	1,018	5,880
Maximum depth (mm)	Sample 1	10.5	14	25	45
	Sample 2	22.5	24.5	18	39
	Sample 3	14.5	17	16	51
Average depth (mm)	Sample 1	8.6	9.8	15.0	30.1
	Sample 2	11.4	13.1	10.1	29.4
	Sample 3	8.9	12.5	11.1	37.2

The analysis of water penetration was conducted following the standards specified in UNE-EN 12390-8:2009 [179] to examine permeability. Cylinders of ϕ150 x 300 mm were subjected to water pressure of 500 ± 50 kPa. It was applied to the cross side of the samples for 72 ± 2 hours. The specimens then were split into two longitudinal parts as it is showed in Figure 5.10. Three samples were then tested for each mixture.

As soon as the split face was dried and the penetration front was visible, penetration area, maximum depth and main depth were measured. Table 5.7 lists the mentioned items, which are useful to study the internal structure of concrete (connectivity of pores and permeability).

5.3.7 Mercury intrusion porosimetry test (MIP)

Concrete, as cement-based material, is a porous material. The microscopic scale of these become more complicate the study of the internal structure. MIP is one of the usually used method to analyze pore structure and Figure 5.11 shows the set uo of the test. It provides information about the connectivity of the pores and microscopy (total porosity and size distribution).
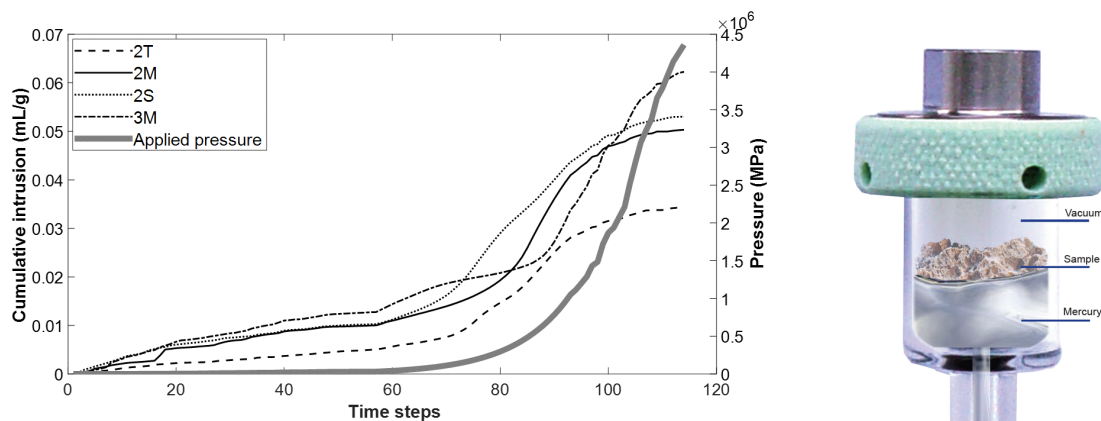
Fig. 5.11 Pressure and cumulative intrusion development during MIP test and the set up

Mercury was forced into the pores and size distribution was defined from the volume induced at each pressure increment. Figure 5.11 shows the evolution of the applied pressure and the cumulative intrusion of each mixture during the test. One sample of each mixture was tested and the size of them was 5 cm^3. The total porosity was defined by the total volume introduced in the specimen. The size distribution (diameter) was determined from the volume placed at each pressure step. This technique is based on the Equation 5.3 proposed by Washburn [192].

$$d_{pore} = \frac{-4\gamma_{Hg}\cos\Phi}{P} \qquad (5.3)$$

where d_{pore} is the pore diameter, γ_{Hg} is the surface tension of mercury (484 x 10^{-3} N/mm), Φ_{Hg} is the contact angle between mercury and pore wall (141°) and P is the applied pressure.

5.3.8   Impact strength test

It is a test for determining the impact energy absorbed in fracturing a test specimen at high velocity. The test consists on repeating impacts against a specimen of concrete following the norm UNE-EN 83514:2005 [184] as it shows Figure 5.12. A 4.54 kg steel ball was dropped repeatedly onto a 63±1.5 mm thick by 150 mm in diameter concrete samples from a height of 457±2 mm. The number of blows required to cause the first visible crack on the top and to cause ultimate failure were counted. The test was used to compare the relative performance of different mixtures.

Fig. 5.12 Impact strength test

Seven samples were tested for each mixture to have representative results. The number of blows to first visible crack as well as to failure are listed in Table 5.8. Samples which were outside the range of the mean number of impacts ±30% were rejected and a new mean was calculated with the remaining samples.

5.3.9   Water absorption by capillary test

The test was performed according to UNE-EN 83982 [185]. The specimens were placed on a plate correctly leveled. Then the container was filled with water up to a level of 5±1 mm. The

Table 5.8 Number of impacts to get first crack and collapse

Type		Samples						
		1	**2**	**3**	**4**	**5**	**6**	**7**
2T	**First crack**	10	13	14	13	30*	5*	6*
	Collapse	18	16	15	15	32*	16	11*
2M	**First crack**	29	48*	18*	24	15*	38*	10*
	Collapse	100	134*	107	91	56*	99	53*
2S	**First crack**	9	10	6	15*	9	3*	3*
	Collapse	86	79	139*	70	35*	45*	42*
3M	**First crack**	17*	5	2*	5	6	3*	6
	Collapse	64*	39	32	35	52	31	52

* Rejected samples.

fluid level was maintained at a constant height throughout the experiment, even adding water if it was necessary. At regular intervals, the mass of the specimens were measured using a balance to measure the penetrated water by capillary. The amount of fluid absorbed was then calculated comparing with the weight of the dry samples. This test method is strongly conditioned by the environment conditions. Thus, the samples were covered throughout the test to avoid that the results were affected by temperature and humidity changes. Figure 5.13 shows the setting of the test.
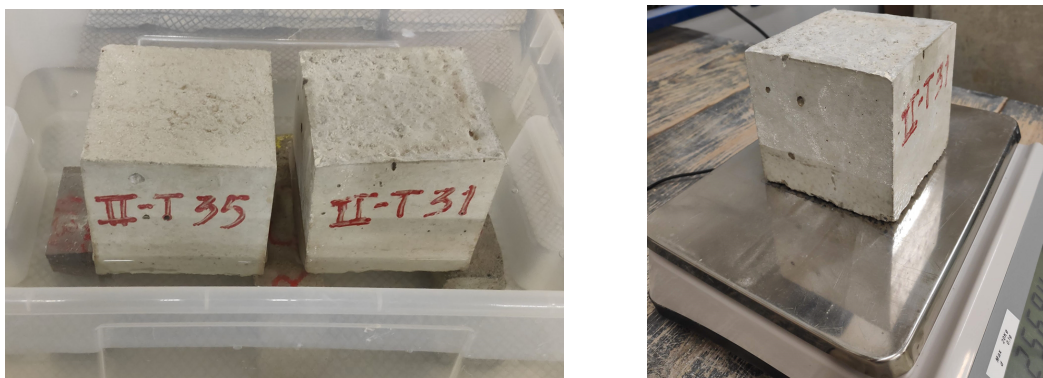
Fig. 5.13 Water absorption test

Two cubes of 100 x 100 x 100 mm of each mixture were tested. There was not much variability between the samples in all cases. In view of that fact, Figure 5.14 illustrated the mean curves of the development of the relative absorbed weights. The test was considered as completed when there were not absorption of water in two consecutive measurements. These

data fed the Equation 5.4 to calculate water absorption coefficient (K), the effective porosity (ε_{ef}) and resistance to water penetration (r_p),

$$r_p = \frac{t_n}{h^2} \tag{5.4a}$$

$$\varepsilon_{ef} = \frac{Q_n - Q_0}{A \, h \, \delta_w} \tag{5.4b}$$

$$K = \frac{\delta_w \, \varepsilon_{ef}}{10 \, r_p^{0.5}} \tag{5.4c}$$

where δ_w is water density, Q_n is the weight of the saturated sample, Q_0 is the weight of the dried sample, A is the section, h is the height of the specimen and t_n is the saturation time.
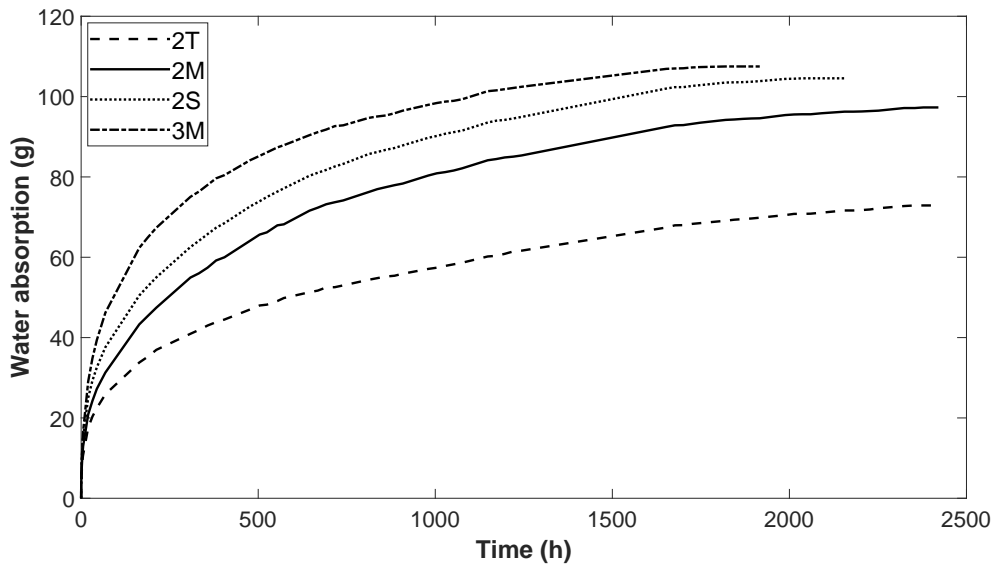
Fig. 5.14 Increase of mass during the capillary water absorption test

5.3.10 Drying shrinkage of concrete test

Shrinkage test was carried out through 285 x 70 x 70 mm prismatic specimens and three prisms were casted for each type of concrete. A uniaxial method was carried out fixing one end of the specimen and measuring the displacements in the free end according to UNE-EN 83318 [186]. The amount of drying shrinkage depends on the environmental conditions, for this reason it is important keeping the same environmental conditions in the testing room. The mentioned norm suggests a chamber temperature of $20 \pm 2\,°C$ and humidity of 50%.

The length change was measured in each specimen due to the shrinkage caused by the loss of water. The behavior of the three specimens were almost the same, Figure 5.15 shows the average curves of the evolution of the length along the time.
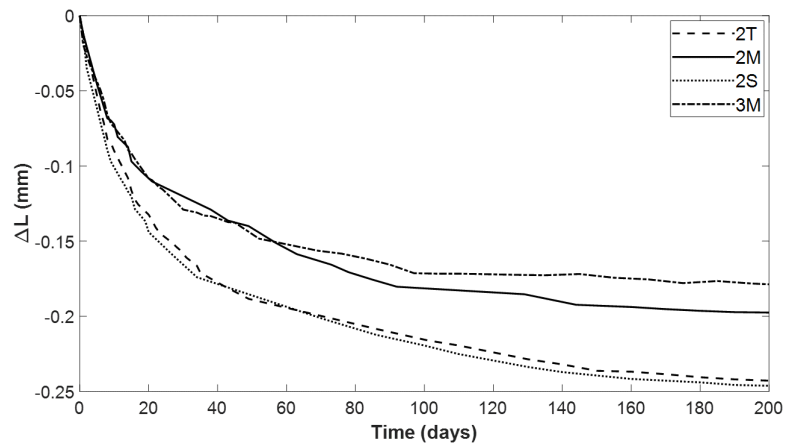
Fig. 5.15 Length change during shrinkage test

Chapter 6

Test results and discussion

6.1 Introduction

This section presents the results from the test carried out at the Laboratory of Large Civil Engineering Structures of the UBU. The main objectives of the tests were studying the behavior of different types of mixtures (2T, 2M, 2S and 3M), which were presented in Section 5.2, and defining the inputs to feed the numerical tool.

6.2 Hardened concrete test results

In this section the measured variables during the test are analyzed and interpreted. The results are compared between them and with other authors conclusions. Inputs to feed the numerical tool are also defined.

6.2.1 Compression test of concrete

Concrete is distinguished by having a great compressive strength. This feature is used in most of its applications, thus the determination of it is well-known and normalized. The compression test was carried out following the norm UNE-EN 12390-3:2009 [177] for compression tests and UNE-EN 12390-13 [176] for the elastic modulus. Table 6.1 shows the mean values and the standard deviation, in parentheses, of each property.

The addition of steel fibers has hardly any effect on the compressive strength, as other authors has also concluded [31, 191, 59]. The evolution of this property with the age, measured in terms of the ratio between f_{c7} and f_{c28}, is similar (72-78%) for all cases. In all cases, the scatter of results decreased with the time, being the ratio between f_{c90} and f_{c365}

Table 6.1 Compressive strength, elastic modulus and Poisson's ratio

	2T	2M	2S	3M
Age	**Compressive strength (MPa)**			
7 days	47.09 (1.5)	38.16 (0.4)	33.26 (0.1)	20.16 (0.3)
28 days	59.66 (5.7)	53.09 (1.5)	46.08 (1.0)	27.40 (1.3)
90 days	75.31 (4.1)	63.63 (3.6)	56.84 (5.3)	33.25 (1.0)
1 year	76.74 (0.2)	68.75 (5.3)	60.45 (2.7)	38.11 (1.2)
Modulus of elasticity (GPa)				
90 days	40.1 (0.7)	34.7 (1.5)	31.6 (0.9)	26.05 (0.5)
Poisson's ratio				
	0.23	0.22	0.22	0.19

87-98%. Analysing the effect of different cements, the compressive strength of 3M are about the half of the 2M for all ages.
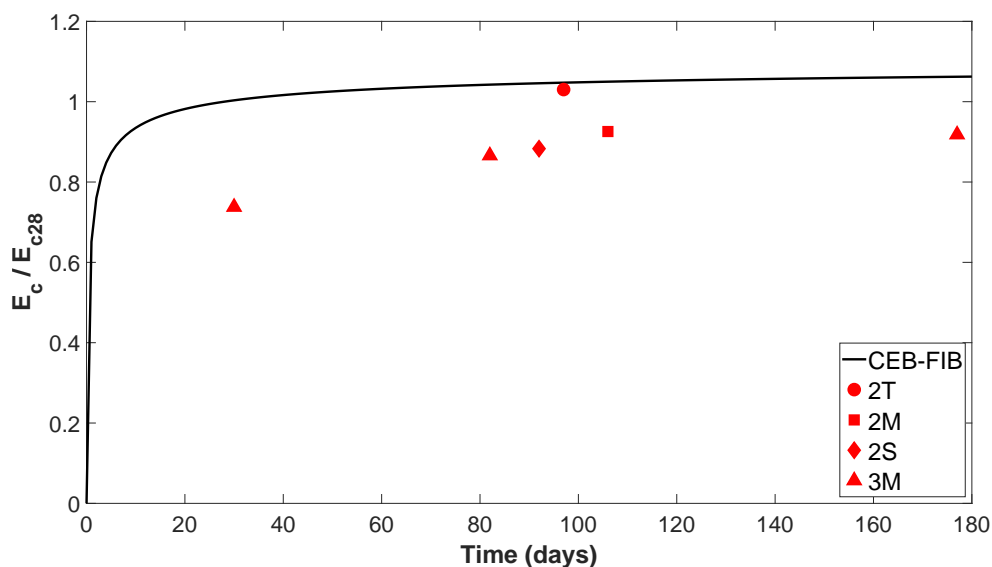

Fig. 6.1 Development of elastic modulus with time

Focusing on the modulus of elasticity, Figure 6.1, the evolution of the elastic modulus is studied through the Equation 6.1a suggested by CEB-FIB [37]. The first days Young's modulus varied notoriously tending to slow down over time. Despite plain concrete set

shows a remarkable agreement with the curve, the mixtures with fibers tend to be slightly overestimated.

$$E_{ci}(t) = \beta_E(t)\, E_{28} \tag{6.1a}$$

$$\beta_E(t) = [\beta_{cc}(t)]^{0.5} \tag{6.1b}$$

$$\beta_{cc}(t) = e^{s\,[1-(\frac{28}{t})^{0.5}]} \tag{6.1c}$$

where,

$E_{ci}(t)$ Modulus of elasticity (MPa) at an age t in days

$\beta_E(t)$ Coefficient which depends on the age of concrete, t in days

E_{28} Modulus of elasticity (MPa) at an age of 28 days (Equation 6.3)

$\beta_{cc}(t)$ Coefficient to describe the development with time

s   Coefficient which depends on the strength class of cement [37]

In regard to the relationship between compressive strength (f_c) and elastic modulus, this last one is usually estimated using linear or exponential equations depending on compressive strength [31, 191]. For normal strength concrete, the American Concrete Code (ACI-318) and CEB-FIB expresses Equation 6.2 and Equation 6.3 respectively.

$$E_{28} = 4700\sqrt{f_c} \tag{6.2}$$

$$E_{28} = 21.5 \times 10^3 \left(\frac{f_c}{10}\right)^{1/3} \tag{6.3}$$

In Figure 6.2, the theoretical curves, calculated with Equation 6.2 and 6.3, were compared with the experimental results. All the mixtures were close to the curves, despite the addition of fibers. This makes sense because fibers have negligible effect on the compressive strength and the elastic modulus was poorly affected. Moreover, it was also noted that the relationship between the mentioned variables were valid for different type of cements.
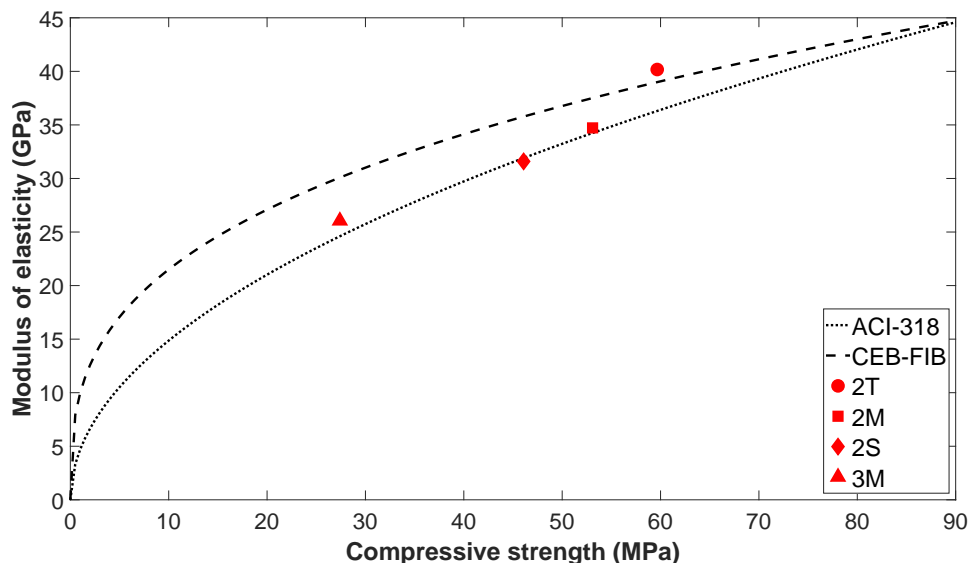
Fig. 6.2 Relationship between elastic modulus and compressive strength at 28 days

6.2.2   Indirect tensile test

Determining this property was not an easy task through direct methods. They induced secondary stresses during the testing that result in an uneven tensile strength. For this reason, indirect tensile test or "Brazilian test" were widely used for its simplicity and easiness. This test were carried out following UNE-EN 12390-6:2010 [178] and the results are shown in Table 6.2.

Table 6.2 Indirect tensile strength (MPa)

	2T	2M	2S	3M
Mean (std)	5.11 (0.5)	4.84 (0.6)	4.35 (0.4)	3.36 (0.4)

Engineers usually assessed this property through the relationship between compressive and tensile strength, which is approximately ten times less than the compressive strength [26]. In Figure 6.3 empirical curves for plain concrete suggested by CEB-FIB, Equation 6.4 and ACI-318, Equation 6.5, were drawn together with the Equation 6.6 for SFRC [195]. In any case the ratio of the strengths decreased with increasing compressive strength and was

close to the 10%. Hence, the increase in the tensile strength occurred at a much smaller rate compared to the increase of compressive strength.

$$f_t = 0.3 \ f_c^{2/3} \qquad\qquad\qquad\qquad f_c < 50 MPa \qquad\qquad (6.4a)$$

$$f_t = 2.12 \ \ln[1 + 0.1(f_c + 8)] \qquad\qquad f_c > 50 MPa \qquad\qquad (6.4b)$$

$$f_t = 0.56 \ f_c^{0.5} \qquad\qquad\qquad\qquad\qquad\qquad (6.5)$$

$$f_t = 0.21 \ f_c^{0.83} \qquad\qquad\qquad\qquad\qquad\qquad (6.6)$$

Focusing on the performed experimentation, there were not significant differences between the experimental results and the proposed empirical curves. All mixes were consistent with the proposed equations ranging the ratio between 8-12%, which agreed with the value expected.
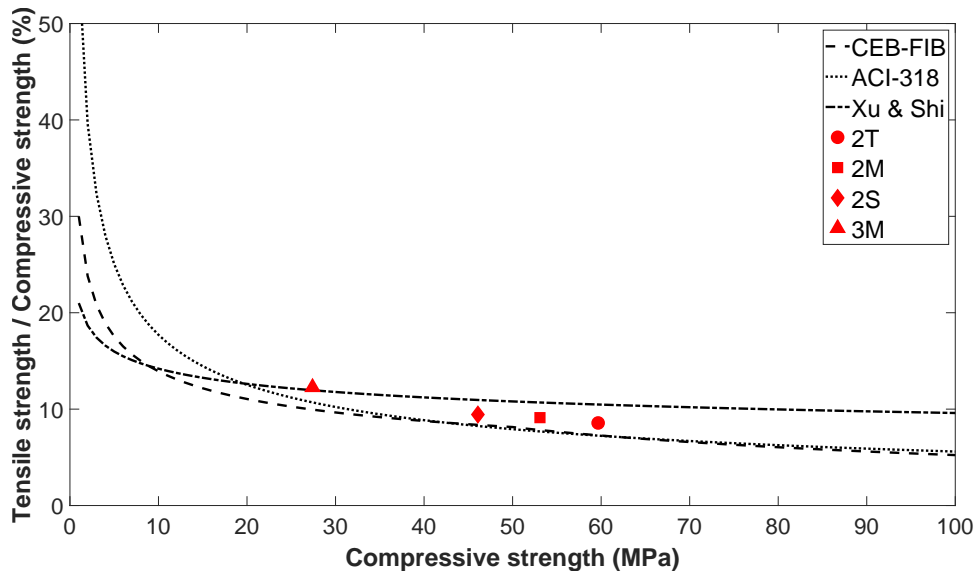

Fig. 6.3 Relationship between tensile strength and compressive strength

6.2.3 Uniaxial tensile test

Direct tensile tests are not widely used for concrete and there is a lack of guidance to carried out this kind of test [194]. In this research, direct tension test were performed using small

size dog-bone shaped specimens as were described in Section 5.3.3. They were subjected to direct monotonic tensile loading to define the tensile properties.

Table 6.3 Direct tensile test: Tensile strength (MPa) and modulus of elasticity (GPa)

		2T	2M	2S	3M
Mean (std)	Tensile strength	4.25 (0.17)	3.77 (0.4)	3.66 (0.4)	3.14 (0.2)
	Young's modulus	38.5 (1.0)	37.9 (2.8)	35.5 (0.3)	32.3 (0.1)

The direct tensile test method showed lower tensile stress (Table 6.3) than the Brazilian test (Table 6.2) as previous studies suggested [158]. The values of uniaxial tensile strength were 17%, 22%, 16% and 7% lower than the indirect tensile strength for 2T, 2M, 2S and 3M mixtures respectively.

(a) 2T

(b) 2M

(c) 2S

(d) 3M
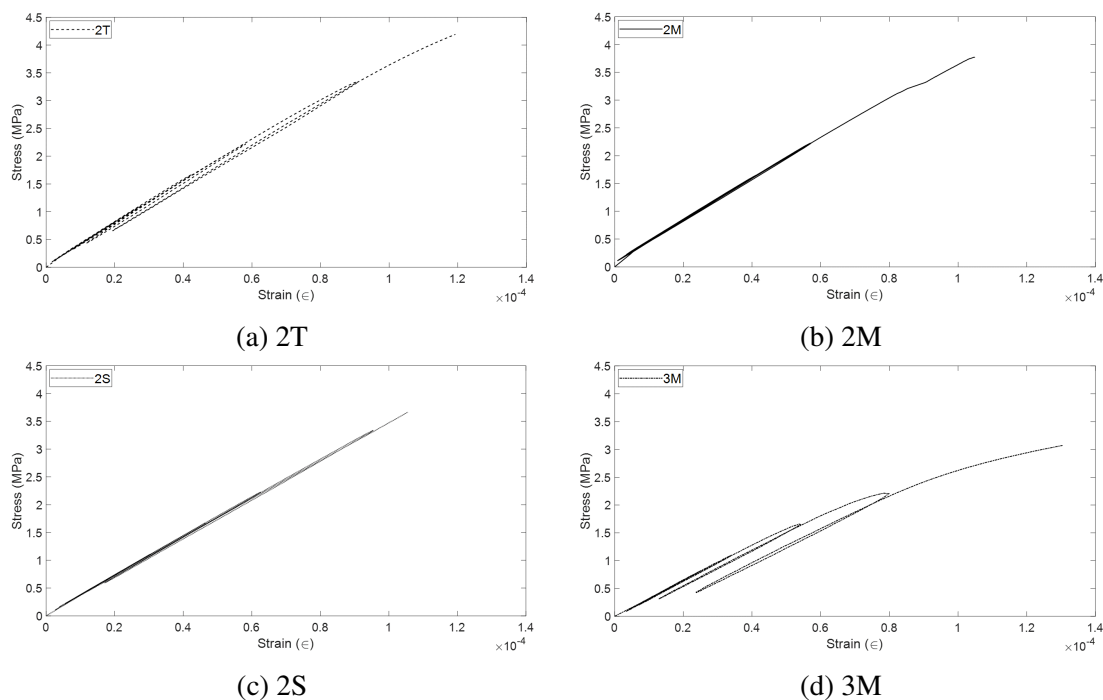
Fig. 6.4 Strain-stress curve of uniaxial tensile test

They also showed higher variability in the measured modulus of elasticity Table 6.3, which increases the uncertainty especially when it is intended to be used in structural members. The tensile Young's modulus tended to be slightly greater than compressive Young's modulus for mixtures with fibers as was suggested in previous studies [158, 199]. It is worth mentioning that dog-bone tests were carried out at the age of 160 days, while the compressive tests were tested 90 days after casting. Mixtures with fibers, 2M, 2S and 3M,

showed a difference of 9%, 12% and 23%. In line with previous results, 3M mixture showed less strength than 2M mixture in Figure 6.4. It can also be seen the difference between the elastic modulus, which is lower for 3M mixture, as was expected.

Although the results are quite rational further research is needed due to the existence of size effect that affects the results [187]. Other interesting properties, such as fracture energy, might be defined scaling fiber and aggregate size. Another point to take into account is the number of fibers that cross the crack. Some of the specimens were broken on section where there were hardly any fiber crossing it, as illustrated in Figure 6.5, which suggested that the fiber distribution was not uniform. An in-depth knowledge of fiber scaling may also improve fiber distribution avoiding this kind of problems.

Fig. 6.5 Fibers crossing the cracking section

X-RAY COMPUTED TOMOGRAPHY

Taking advantage of the reduced size of the specimens, X-ray computed tomographies (XCT) were done to study the microstructure of the dog bones (except for 3M). Table 6.4 illustrates the volume distribution of steel content (steel inclusions and fibers), EAFS, matrix and air (air and synthetic fibers).

Table 6.4 Volume distribution in dog-bones samples

Volume (%)	2T	2M	2S
Steel inclusions & fibers	0.5	1.3	0.4
EAFS	40.2	39.1	36.5
Matrix	58.0	57.9	60.7
Air & Synthetic fibers	1.3	1.7	2.4

There were few samples to find a correlation between strength properties and volumetric distribution. Despite this drawback, it can be deducted that samples with more steel content shows superior tensile strength. It also confirms that the content of fibers is close to 1%, if it is compared the steel content with other samples. Specimens with fibers showed higher porosity as it will be reported in the following points. This point might be the cause of the loss of stiffness, despite the addition of steel fibers. Furthermore, the unusual tensile strength reported in Table 6.3 by samples with synthetic fibers, may be justified by the greater volume of matrix.
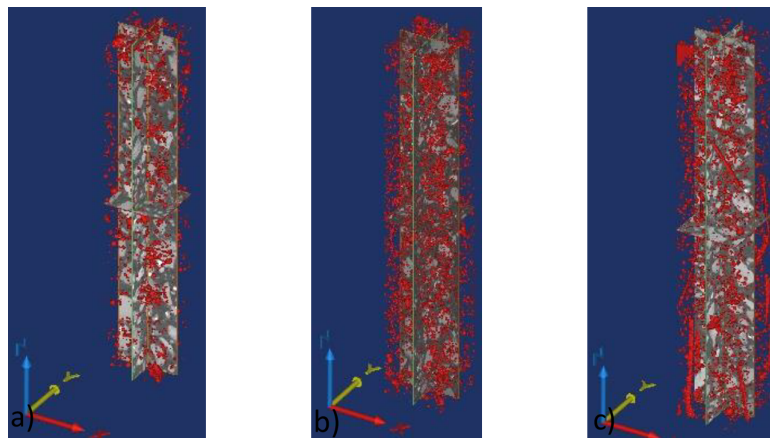
Fig. 6.6 XCT images for visualizing synthetic fibers and air voids
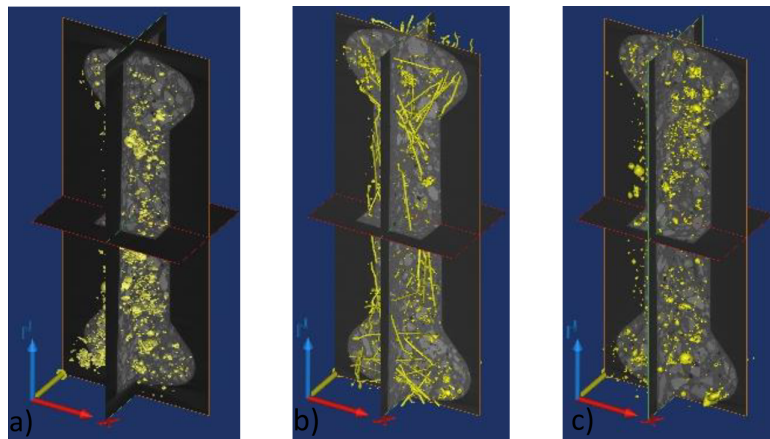
Fig. 6.7 XCT images for visualizing steel fibers and inclusions

The X-ray attenuation of the synthetic fibers is similar to the air voids as it is showed in Figure 6.6. The software was unable to separate air voids from fibers due to its pixel intensity. This hider the identification of fibers through imaging treatment. Moreover, the low flexibility of the fibers difficult distinguishing the shape and size of the fiber due to the curved

and bent fibers. Although it was an initial approach to study the orientation and distribution of fibers, in future studies this problem might be solved filtering the length of the identified objects. The fiber have one length much longer than the other (ellipsoid) while, air voids are more spherical.

Regarding steel fibers, they are easier to identify as it can be deducted form Figure 6.7. It also shows that fibers are distributed non-homogeneously due to the disproportionate size of the fibers compared with the neck of the specimen. Most of the fibers are located in the head of the bones which are out of the testing section (middle section). The steel inclusions (yellow spots) are steel particles which are within the aggregates, owing to they are waste from steel industry.

6.2.4 Flexural strength test

The flexural test was performed under a four-point loading arrangement based on UNE-EN 83509 and UNE-EN 83510 [182, 183]. The results of the test are presented in Table 6.5 and Figure 6.8.

Table 6.5 Flexural strength test results

	2T	2M	2S	3M
Flexural strength (MPa)	7.93 (2.3)	5.97 (1.1)	5.04 (0.3)	4.43
First crack strength (MPa)	7.59 (2.1)	4.89 (1.4)	4.13 (0.5)	4.23
Toughness (Nmm)	8,611	21,376	11,719	15,148
Fracture energy, G_F (N/mm)	0.749	2.153	1.19	1.533

Figure 6.8 shows the load-deflection curve and the enclosed area by the curve. Comparing plain and fibrous concrete, it is clear that they show different post-peak behavior. Once plain concrete was cracked, stresses were concentrated at crack tips causing a fast propagation until the fracture (brittle failure). Nevertheless, specimens with fibers were cracked but not totally fractured maintaining the ability to carry load after the peak, as can be seen in Figure 6.9. Fibers crossed the crack and transferred the load due to the bridging effect. This reduced the crack growth rate and improved the strength and toughness of concrete.

Toughness or energy absorption is defined as the area under the load-deflection curve Figure 6.8 and it was calculated according to UNE-EN 83510 [183]. Despite the fact that plain concrete is a brittle material, the area under the curve was calculated to have a reference to be compared with. Steel fibers remarkably improved this property, which was duplicated from plain concrete as is showed in Table 6.5. Although synthetic fibers also increased it, the enhancements were not as significant as for steel fibers. The improvement of this kind
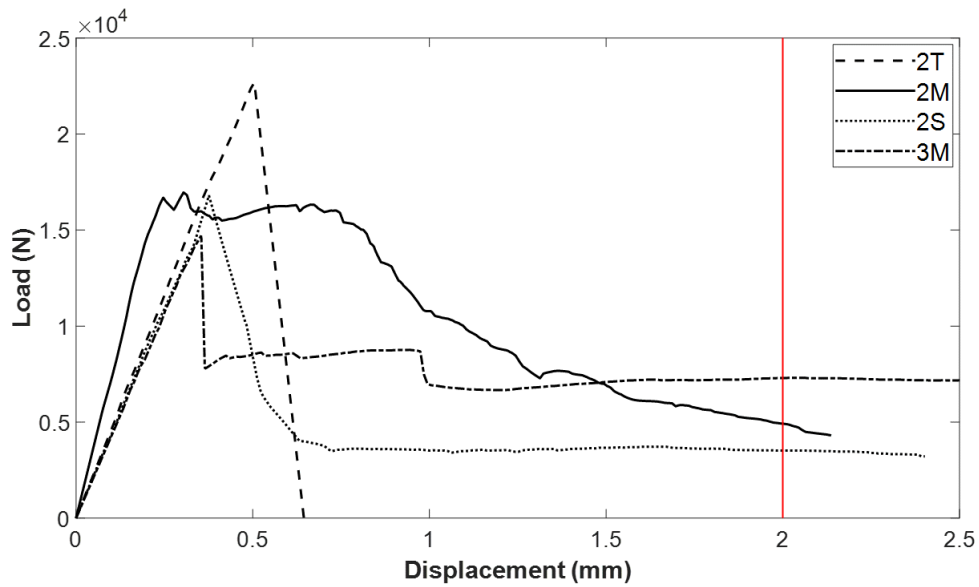
Fig. 6.8 Average load-deflection curves determined through flexural test

of fibers was about 35% while for steel fibers was 150%. The difference in post-cracking toughness is due to the energy needed to pull out fibers.

(a) Plain concrete   (b) Steel fiber RC   (c) Synthetic fiber RC
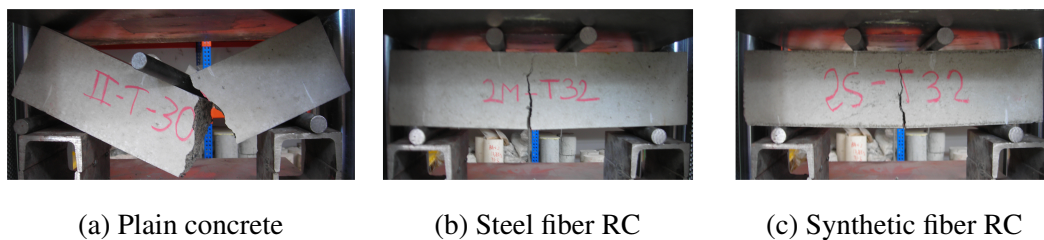
Fig. 6.9 Modes of failure of flexural beams

Flexural strength of fibrous mixtures almost concur with tensile strength calculated through Brazilian test and direct test. However, there was a significant difference with the values of plain concrete, which did not have any correlation with other tests.

Another parameter studied in Table 6.5 was fracture energy (G_F). Fracture energy is the energy needed to create a crack of unit area. It is defined as the area under the load–deflection curve per unit fractured surface area. It was assumed that the beam failed at 2 mm (span

length/150) following [183]. The most widely used fracture mechanics models for analyzing concrete structures is the model proposed by *Hilleborg* [72]:

$$G_F = \frac{W_0 + mg\delta_{end}}{A_{lig}} \tag{6.7a}$$

$$G_F = \frac{W_0 - 0.5mg\delta_{end}}{A_{lig}} \tag{6.7b}$$

where W_0 is the area under the load–deflection curve, m is the mass of the specimen between the supports, g is gravity, δ_{end} is the end deflection and A_{lig} is the fracture area. Equation (6.7a) is valid if the loading direction match with the weight vector. However, the weight factor is neglected if the beam is loaded normal to the self weight vector. Another case is when the beam is loaded opposing the weight vector. In that case, Equation (6.7b) is used to take account of the weight factor [170]. It is worth noting that self weight term may be quite significant when young concrete or large specimens are being tested.

A considerable increase was obtained in fracture energy by adding fibers, in particular in specimens with steel fibers. As seen in Figure 6.8, the sharp fall at mixture 3M show that it might be increased its performance by adding steel fibers, the mixture accepts a largest quantity of fibers.

6.2.5   Notched beam test

Three-point bending beam method was employed to measure the flexural toughness, which is extremely important for the safety and durability of structures. The evaluation method based on UNE-EN 14651 [180] was followed to evaluate the residual stress listed on the Table 6.6.

Table 6.6 Toughness, first-crack strength and post-cracking behavior of the mixes

Property		2T	2M	2S	3M
Limit of proportionality, LOP (MPa)		5.2	5.98	3.66	3.94
Residual strength (MPa)	F_{RJ1}	-	6.52	1.21	2.37
	F_{RJ2}	-	5.70	1.17	2.54
	F_{RJ3}	-	3.96	1.29	2.72
	F_{RJ4}	-	3.01	1.31	2.74
Fracture energy, G_F (N/mm)		0.137	2.235	0.598	1.165
Fracture energy (CMOD), $G_{F,CMOD}$ (N/mm)		0.162	2.637	0.707	1.378

One of the main test parameter is the limit of proportionality (LOP), that is the stress at the load-CMOD curve at which the shape of the curve first becomes nonlinear. According

to UNE-EN 14651 [180], the first crack point corresponds to the maximum load recorded in the range between 0 and 0.05 mm of CMOD. It approximately corresponds to the onset of cracking in concrete matrix. Beyond this point, the fibers become more active to reduce the crack opening. In Figure 6.10 can be observed that the peak loads of the SFRC beams were slightly different from those of plain concrete. Mixtures with synthetic fibers showed lower values than plain concrete. This difference might have been due to surrounding factors during the making procedure which increase the air content in the mixture [68]. Nevertheless, the main differences between mixtures were at the postpeak behavior, where mixtures with fibers, especially SFRC ones, showed a ductile behavior.
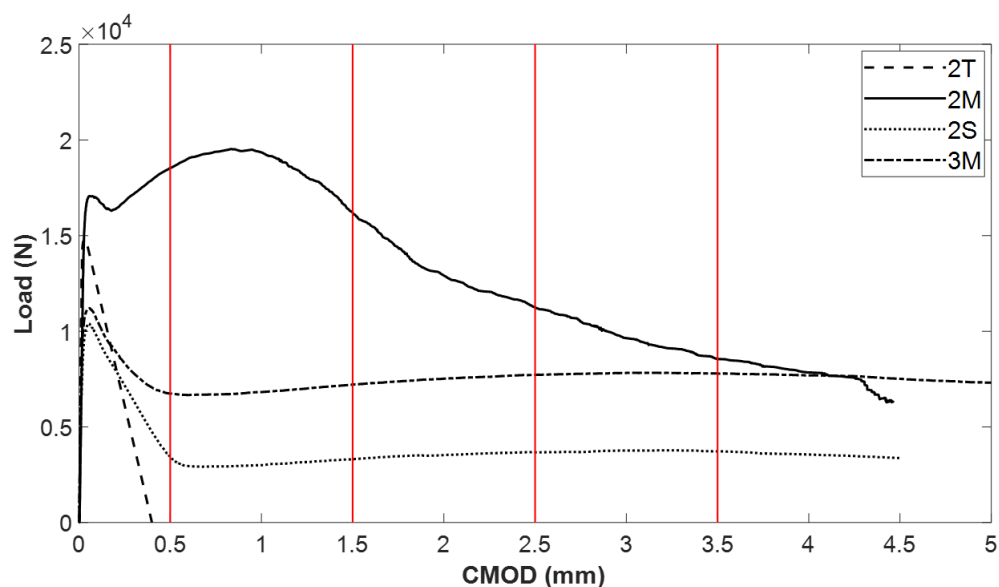
Fig. 6.10 Average curves of the notched test

Residual stress (F_{RJ1}, F_{RJ2}, F_{RJ3} and F_{RJ4}) are another parameter that defines the shape of the postpeak curve. The values of residual stress were calculated according to UNE-EN 14651 [180] and they are listed in Table 6.6. In the case of plain concrete a brittle failure occurred, while SFRC specimens showed a more ductile behavior. This difference can be physically seen in Figure 6.12, where fibers on the fracture surface bridged the cracks and linked the two parts of the element. However, the beam was completely fractured in Figure 6.12(a) due to the absence of fibers. In fact, the first crack point of the fibrous specimens might be joined to the crack of concrete matrix.

Figure 6.11 shows the different residual stress for different mixtures. The residual stress did not exist for plain concrete because beams failed immediately after the first crack. SFRC showed higher residual stress F_{RJ1}, F_{RJ2}, F_{RJ3} and F_{RJ4} than for synthetic fibers. Steel fibers increased by 3-6 times synthetic strength and the effect became particularly relevant just

Fig. 6.11 Toughness index comparison

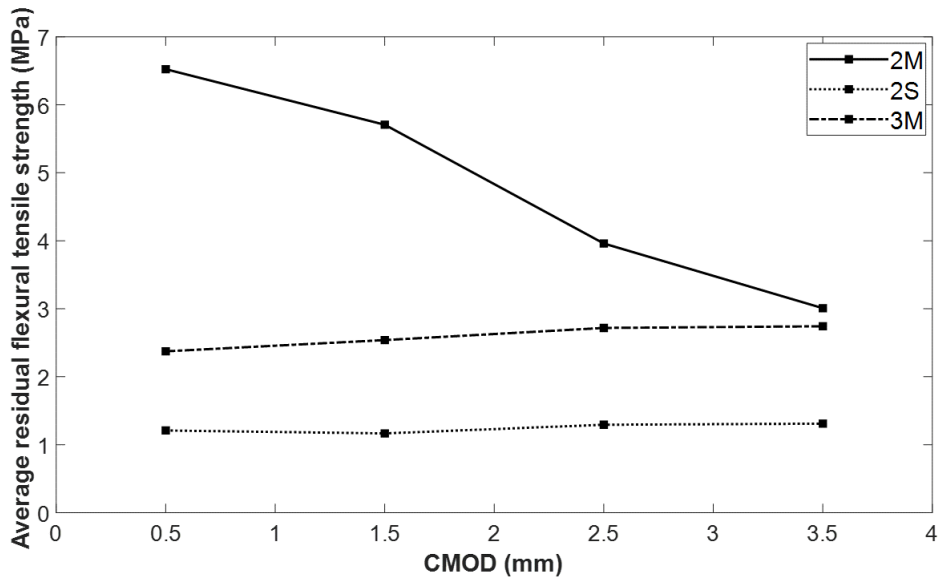after the peak stress. In the case of steel fibers could have continued loading after the first crack. This behavior mainly depends on the dosage of fibers [190, 22].

$$\delta = 0.85 \, CMOD + 0.04 \qquad (6.8)$$

Previous research [75, 53, 48, 25] have studied the relationship between the load-deflection and load-CMOD diagrams of bending beams. In fact, the UNE-EN 14651 [180] provides a linear relation between mid-span deflection and CMOD by means of Equation 6.8. Using this relation fracture energy has been calculated based on both diagrams, G_F and $G_{F,CMOD}$. According to *Barros et al.* [23] only the fracture energy dissipated up to a deflection of 3 mm is interesting from the design point of view. In this research the fracture energy was evaluated referring to CMOD of 3.5 mm; which, in accordance with Equation 6.8, was the same deflection.

A considerable increase was obtained in the fracture energy by adding fibers, especially with steel ones Table 6.6. The factor representing the difference between fracture energies, G_F and $G_{F,CMOD}$, was around 15% for all the mixtures. Compared to the fracture energy calculated through the flexural test (unnotched beams), Table 6.5, there were some slight differences. These differences, as *Hillerborg* [72] showed, might have been due to fracture energy parameter is size-dependent. Another aspect that influence in the result is the notch/depth ratio. Fracture energy increase with an increase in depth of beam [53, 144].

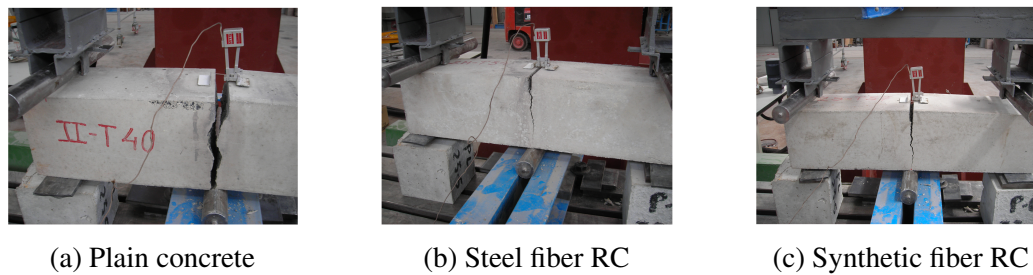(a) Plain concrete   (b) Steel fiber RC   (c) Synthetic fiber RC

Fig. 6.12 Modes of failure of notched beams

Therefore, it can be considered that the result in both test are consistent despite of the existing small differences.

6.2.6   Impact strength test

The impact resistance was evaluated in terms of first crack and failure impact energy as it is indicated in UNE-EN 83514:2005 [184]. The obtained mean values and standard deviation of blows are presented in Table 6.7.

Table 6.7 Results from impact test

	2T	2M	2S	3M
Nos. of hits until first crack	12.5 (1.7)	26.5 (3.5)	8.5 (1.7)	5.5 (0.6)
Nos. of hits until breakage	16.0 (1.2)	99.3 (6.6)	78.3 (8.0)	40.2 (9.6)

The number of hits for causing the first crack increased significantly for samples with metallic fibers compared to plain concrete and mixtures with synthetic fibers. In line with the previous test, the mixture 3M showed the worst results. However, it should be noted that 3M in accordance with 2M and 2S, showed a significant variation in the number of blows for causing the first crack and ultimate failure, 86%, 73% and 89% respectively. Nevertheless plain concrete presented similar values of first crack and ultimate failure (22%). Fiber reinforced concrete mixes were found to be more rate sensitive than respective unreinforced mixtures, especially for ultimate failure. Therefore, impact resistance was increased substantially with the addition of randomly distributed fibers as other authors had also suggested [116, 112, 14].

6.2.7   Water penetration under pressure test

Concrete is a porous material and this implies that through the pores network aggressive substances dissolved in water can penetrate inwards. The analysis of water penetration

intend to show the internal structure of concrete (porosity) through the penetration level of water under pressure. These concepts are closely related to the durability of the material. Water penetration testing was carried out to examine permeability and to enable comparisons between different mixtures. The tests were conducted following the standards specified in UNE-EN 12390-8:2009 [179]. Table 6.8 illustrates the results calculated based on the measured variables in the test. The average depth and area of the water front were calculated as the mean and standard deviation of three samples. Nevertheless, the maximum depth was defined as the maximum depth of the three samples.

Table 6.8 Depth of water penetration under pressure

	2T	2M	2S	3M
Area (mm^2)	1,031 (178)	1,337 (283)	1,305 (452)	4,939 (822)
Maximum depth (mm)	16 (6.1)	19 (5.4)	20 (4.7)	45 (6.0)
Average depth (mm)	10 (4.5)	12 (4.8)	12 (5.1)	32 (12.8)

The results summarized in Table 6.8 shows that penetration area were 28% larger in specimens with fibers and the variability was also higher. This last point emphasize even more the importance of mixing well concrete with fibers. Water penetration depth in mixtures with fibers increased by 20% over plain concrete. Although maximum depths followed the same trend, the differences were less remarkable. This might be explained by the fact that water permeability depends on pore size distribution and connectivity of pores, among other factors. Somehow, fibers played the role of connecting pores and conducting the water in [107].

Regarding the mixtures, 2T, 2M, 2S and 3M had acceptable values compared for instance, with the Spanish Structural Concrete Code (EHE-08). It requires that the maximum and average depth cannot exceed 50 mm and 30 mm respectively and they amply met both conditions. One of the sample of the 3M composite exceeded slightly the norm, thus, it might require improvements in its dosage. The penetration area was almost four times the size of 2M mixtures, which underlined also the need of improving the dosage.

6.2.8   Mercury intrusion porosimetry (MIP) test

Mercury intrusion porosimetry (MIP) is a method for characterizing the porosity of concrete matrix. This method yields significant parameters that define the pore structure, such as pore radius and size distribution. Table 6.9 illustrates the results of the test for different mixtures.

MIP results do, however, provided two useful curves: the cumulative curve and size distribution curve. The cumulative curve, Figure 6.13(a), measures the permeation capacity.

Table 6.9 Pore size distribution of concretes

	Porosity (%)	Pore size distribution (%)			
		<0.02 μm	0.02-0.05 μm	0.05-0.2 μm	>0.2 μm
2T	9.5	11.4	26.5	36.0	26.1
2M	12.3	10.5	29.4	30.2	30.0
2S	13.4	10.7	20.7	32.5	36.1
3M	14.7	32.5	29.6	6.8	31.1
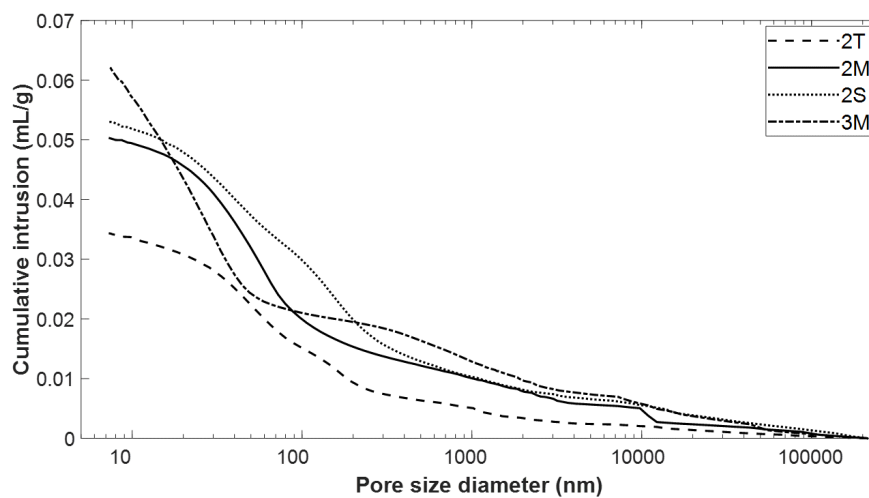
(a) Cumulative intrusion
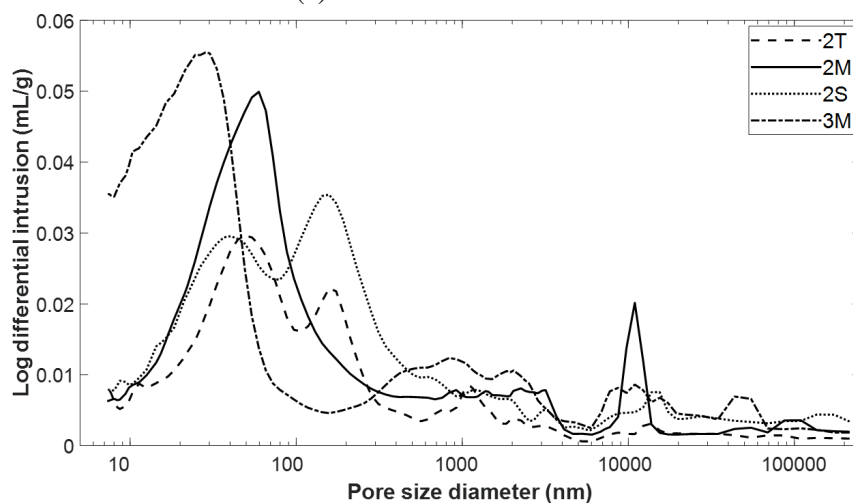
(b) Pore size distribution

Fig. 6.13 Mercury intrusion porosimetry curves

The total pore space is defined by the volume of mercury introduced into the samples and it is an indication of the total porosity.

On the other hand, Figure 6.13(b) details the pore size distribution. The exhibited initial peak corresponds to the size of pore necks connecting a pore network, disappearing as pores become blocked with hydration product. The presence of another sharply peak in the differential curve of 2T indicates the intrusion of mercury throughout the specimen through a pore network. The average pore diameter were 48.3, 49.5, 55.7 and 27.1 nm for 2T, 2M, 2S and 3M mixtures.

According to Table 6.9, the total porosity of the different mixes ranges between 9 and 15%. These results agree with previous findings [125]. The total porosity was slightly smaller for 2T, 2M, and 2S mixtures than for 3M mixture, which indicated that mixtures made with mix of CEM-II were more compact. This observation is aligned with the properties related to the strength and performance of concrete studied previously. Porosity also plays an important role in the long-term durability of concrete [125]. Consequently, mixtures composed of CEM-II, especially the mix without fibers, would show a better resistance against chemical agents.

The addition of fibers increased slightly the porosity from 9.5% to 12.3% and 13,4%. This might be explained by the fact that fibers might provide stiffness to the internal structure and tends to preserve the internal structure of fresh state [189]. Therefore, fibers enables to maintain unchangeable the internal structure of the mixes with fibers. On the other hand, the pore size distribution did not seem to be strongly affected by the incorporation of fibers as other researcher had also suggested [125].

6.2.9   Water absorption by capillary test

Capillary absorption represents the main mechanisms for water to transport inside concrete. The empty capillary pores start to fill with water due to capillary suction, when concrete comes into contact with water. The porosity allows aggressive agents to reach the reinforcement. Therefore, it is a parameter considered as a measure of the durability of a material. The UNE-EN 83982 [185] was adopted to evaluate the capillary absorption, which is based on the Fagerlund method.

Figure 6.14 shows the amount of fluid absorbed normalized by the cross-section area of the specimen exposed to the fluid along the time. In accordance with Section 6.2.7, mixtures with fibers had absorbed more water and it was also confirmed that the mixture 3M had the worst performance.

In Table 6.10 are listed the average values of resistance to water penetration (r_p), the effective porosity (ε_e) and water absorption coefficient (K_a). These parameters were used to evaluate numerically the behavior of each mixture. Absorption coefficient is a characteristic of concrete to transport into material and it is used to evaluate the durability of the material.
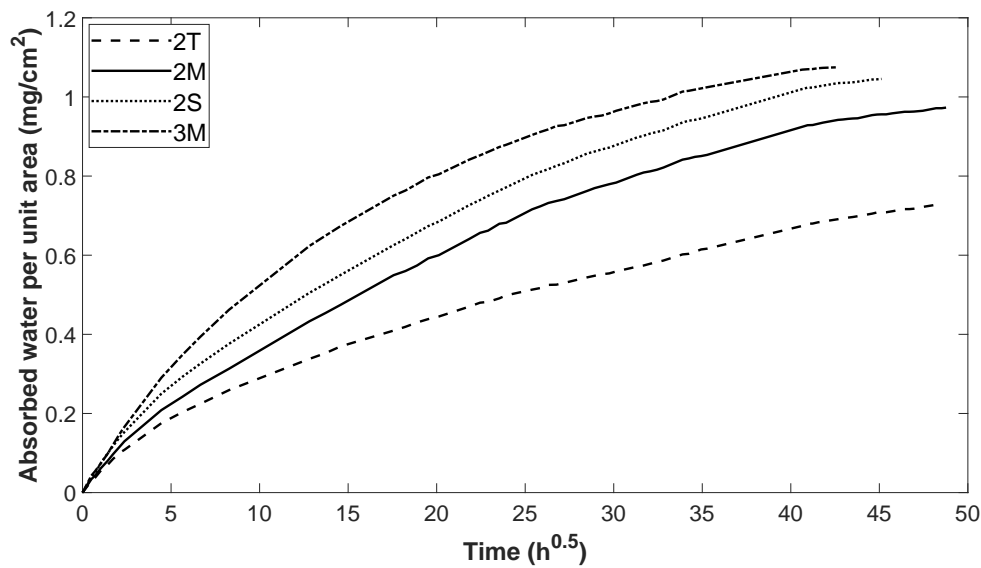
Fig. 6.14 Capillary suction curves for specimens

Table 6.10 Water absorption test results

	2T	2M	2S	3M
r_p (min/cm^2)	1,412.4	1,427.1	1,221.6	1,092.2
ε_{ef} (%)	7.3	9.7	10.5	10.8
K_a (kg/$m^2 min^{0.5}$)	1.94x10^{-3}	2.58x10^{-3}	2.99x10^{-3}	3.25x10^{-3}

The absorption coefficient corroborated that mixtures without fibers had displayed better conditions that mixes with fibers. The test also confirmed, in accordance with MIP test, that test 3M showed the worst performance. Thus, it might be concluded with regard to durability mixes with fibers or made with CEM-III were more susceptible to be degrade over time.

6.2.10 Drying shrinkage test

The performance of the mixtures in terms of long-term shrinkage is analyzed in this section. This property is related to durability due to the cracking could accelerate deterioration and promote steel corrosion. It is worth mentioning that aggregate density and modulus of elasticity affect directly to the shrinkage [117]. Hence, concrete made of EAFS, which had a higher density and elasticity than natural aggregates, results in lower shrinkage values.

The main motivation of the performed measurements was to compare the results obtained from different mixtures and focus on the effect of different cements and fibers. Figure 6.15 illustrates the average curves of each mixture. The same trend was monitored for mixes with steel fibers (2M and 3M), while 2T and 2S showed a more desirable behavior.
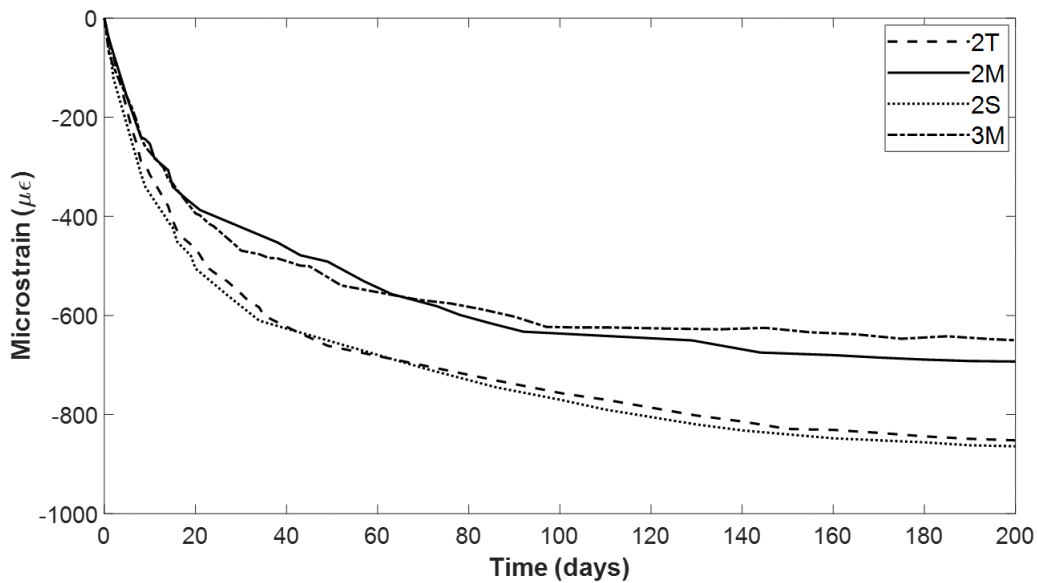
Fig. 6.15 Shrinkage strain results

Analyzing the results of mixes with CEM-II, the addition of steel fibers decreases considerably the drying shrinkage strain. The anchoring effect of steel fibers contributes significantly in the good performance of 2M [16, 17, 200]. The drying shrinkage strain is highly dependent on the modules of elasticity of fibers [200]. This would justify the worse performance of the mix 2S, which shows a similar behavior to 2T. The similitude of the curves is due to the difference between the w/c ratio. Obviously, the increase in water content is directly related to shrinkage [76]. The lower w/c ratio of the mix 2T resembles the behavior of 2T and 2S, despite the addition of the fibers.

The behavior of 3M is quite similar to 2M along the days, despite using CEM-III in the mix. The lower water content of the 3M might be the reason of the similarity. Mixes with granulated blast furnace slag also shows lower shrinkage, principally at early ages [45, 46, 86, 76].This factor may be another reason that justify the good performance of the mix 3M. It is also worth noting that the effect of fibers influences more than the type of the cement in this case. The mix 2T shows a worse performance than the mix 3M.

6.3 Summary of the properties

Table 6.11 summarizes the main properties of the four different mixes and the following points highlighted the main conclusions of the testing:

1. Considering 2T as a reference mix, concrete strength and stiffness decreased in fiber reinforced mixes due to the enlargement of the w/c ratio. Fibers had a negligible effect

on this mechanical properties. Nevertheless, the presence of ground granulated blast slag in 3M leaded to a significant loss of these mechanical properties.

2. Indirect tensile strength of fiber reinforced mixes are similar to plain concrete samples. The sample 3M showed remarkably low values.

3. Direct tensile test (Dog-bone test) reported lower values of tensile strength than the Brazilian test. Images obtained by XCT showed non-random distribution of the fibers in the shaft of the samples, which reduced the effectiveness of the fibers. Dog-bone test will need further research, such as scaling the length and cross-section of fibers, in order to get parameters related to tensile behavior and fracture energy.

4. Steel fibers improved remarkably the ductility of concrete and doubled the toughness of plain concrete. Nevertheless, synthetic fibers had not such a beneficial effect on the ductility.

5. Impact resistance was increased substantially with the addition of fibers, specially for mixes with steel fibers. The existence of ground granulated blast furnace slag did not result in any improvement in performance.

6. The total porosity was increased with the addition of fibers (2M and 2S) and mixes with ground granulated blast furnace slag (3M) showed even worse results. The performance of 2M and 2S significantly differed in the MIP, permeability and water penetration tests from 2T. Fibers connected pores facilitating the intrusion of chemical agents, which affects the long-term durability.

7. The long-term shrinkage strain was highly dependent on the elastic modulus of the fibers, which was showed through the results obtained from 2T, 2M and 2S. Although to a lesser degree, the w/c ratio and type of cements has also influenced in the behavior of the mixes.

Table 6.11 Mechanical properties of concrete mixes

Property		Concrete mix			
		2T	**2M**	**2S**	**3M**
Compressive strength (MPa)	7 days	47.09	38.16	33.26	20.16
	28 days	59.66	53.09	46.08	27.40
	90 days	75.31	63.63	56.84	33.25
	1 year	76.74	68.75	60.45	38.11
Young's modulus (GPa)	90 days	40.1	34.7	31.6	26.05
Poisson's ratio	90 days	0.23	0.22	0.22	0.19
Flexural strength (MPa)		7.93	5.97	5.04	4.43
Fracture energy (N/mm)		0.137	2.235	0.598	1.165
Indirect tensile strength (MPa)		5.11	4.84	4.35	3.36
Direct tensile strength (MPa)		4.25	3.77	3.66	3.14
Depth of water penetration under pressure	Area (mm^2)	1,031	1,337	1,305	4,939
	Max. depth (mm)	16	19	20	45
	Average depth (mm)	10	12	12	32
Porosity (%)		9.5	12.3	13.4	14.7
Absorption coeff. $\left(\frac{10^{-3}kg}{m^2 min^{0.5}} \right)$		1.94	2.58	2.99	3.25

Chapter 7

Evaluation and analysis of the numerical framework for the design of EAFS concrete

7.1 Introduction

In this chapter a framework for the design of concrete reinforced with fibers and manufactured with EAFS is presented and validated through four beams (2T, 2M, 2S and 3M). The objective of this framework is taking a step from material scale to structural scale. The presented characterization is based on the study carried out in the Chapters 5 and 6, while the applied numerical models are extensively explained in Chapter 3 and 4.

7.2 Designing framework

This dissertation was conceived to propose a methodology to design concrete structural elements reinforced with steel fibers. The limited regulatory framework covering this type of structural elements stifled the application of this material. International design guidelines, such as Model Code [38], or local norms, such as the Spanish Structural Concrete Code (EHE-08), show weakness that results in a limited application of this composite in structural elements. For this reason, the proposed methodology combines experimentation, which provides mechanical expertise of the material, and simulation, which extends the applicability to structural elements. Figure 7.1 illustrates the scheme of the methodology followed to design an structural elements.
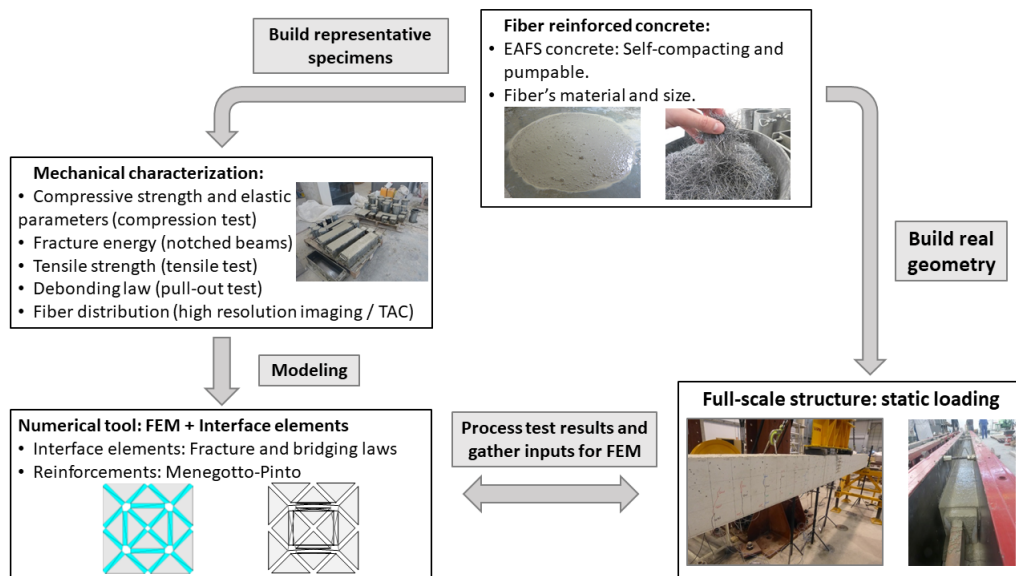
Fig. 7.1 Design methodology for steel fiber reinforced concrete made with EAFS

In this research work, the performance of steel fiber reinforced concrete was studied. The used concrete had the particularity that natural aggregates were substituted by EAFS. Despite many research works were carried out to study the properties of EAFS made concrete, it was not extensively applied to design structural elements [59, 151, 152, 159]. Using EAFS will not only improve the mechanical performance of concrete, it will also result in an environmental benefit. Concrete complied also self-compacting conditions, in spite of the weight of EAFS. Furthermore, Concrete was reinforced with steel fibers to improve its mechanical performance. Nevertheless, fiber addition increased the uncertainties due to the uncontrollability over their distribution of them within concrete elements.

Having identified the material, the properties of the material have to be determined through experimentation. One of the objective of the experimental part was increasing the confidence upon the mechanical performance of SFRC. The absence of a robust standard to design fibers reinforced concrete elements justifies the importance and the extent of the experimentation. A direct vision along with material properties bring a valuable understanding of the behavior of SFRC at the material level. Once the material constitutive model for SFRC is determined, it can be reliably applied to calculate structural elements.

The tests were planned to provide an overall properties of the composite and the inputs needed to feed the numerical tool. The general properties should asses the performance of the material in terms of durability, workability and mechanics. The specifications and results of the tests are explained and analyzed in Chapter 5 and 6, respectively. Furthermore, the requirements of the numerical model conditioned the testing campaign. The physical

model has to be defined in such way that provides enough inputs to feed the numerical model. Therefore, the simulation model has to be previously defined. The experimental tests and the defined parameters are summarized in the following points:

- **Compression test:** The compressive behavior is one of the main characteristics of concrete. The compressive performance is evaluated through the compressive strength at different ages and elastic properties (Young's modulus and Poisson parameter). The compression test is well-known and frequently carried out. The tests were carried out in accordance with UNE-EN 12390-3:2009 [177] and UNE-EN 12390-13 [176].

- **Indirect tensile test (Brazilian test):** A compression load is applied to a specimen and the tensile strength is defined by triaxiality. The test was carried out following the norm UNE-EN 12390-6:2010 [178].

- **Uniaxial tensile test (Dog-bone test):** Tensile strength and Young's modulus were defined through uniaxial methods. In the absence of a norm to follow, a dog-bone specimen was designed to carried out this test [194].

- **Flexural test:** Four-point flexural tests were carried out to asses the flexural strength, toughness and first crack strength. The test was conducted following the norm UNE-EN 83509 [182] and UNE-EN 83510 [183].

- **Notched beam test:** The notched beam test is used to evaluate the residual behavior of the material. The tests were carried out following UNE-EN 14651 [180] and the determined parameters were the fracture energy and the residual strength. Therefore, it is the main test that enables to asses the effect of the fibers.

- **Impact strength test:** The absorbed impact energy is rated following the specifications reported in UNE-EN 83514:2005 [184]. The number of hits until first crack and breakage are counted. It is a variable to compare the performance of the mixtures.

- **Water penetration under pressure test:** The permeability is evaluated applying water pressure to the specimen according to UNE-EN 12390-8:2009 [179]. Water penetration area, average depth and maximum depth were measured.

- **Mercury intrusion porosimetry:** The internal structure of concrete is assessed through MIP test. The pore size distribution and porosity are determined to evaluate the durability of the material.

- **Water absorption by capillary:** This test is also used to evaluate the durabiliy of the material. The absorved water is measured according to UNE-EN 83982 [185] and resistance to water penetration, effective porosity and water absorption coefficient are calculated.

- **Drying shrinkage test.** The performance of the mixtures in terms of long-term shrinkage is analyzed and this property is also related to durability.

FEM were used to simulate fiber reinforced concrete elements. The structural elements consists of concrete made with EAFS, steel or synthetic fibers and steel bars. A model based on interface elements were used to simulate the degradation of concrete and the bridging effect due to the fibers. Damage models were implemented to simulate the softening behavior of the material. The interface elements conditions the discretization of the steel bars (longitudinal and shear reinforcements) as it is explained in Chapter 4. An elastoplastic model (Menegotto-Pinto) was used to describe the behavior of the reinforcements.

Having defined the numerical model, the inputs that characterizes the physical model are also known. The inputs have to be defined directly or indirectly by means of the experiments. The inputs required by the constitutive models are:

- **Concrete:** Young's modulus, Poisson's ratio, tensile strength and fracture energy.

- **Steel/synthetic fibers:** Young's modulus, tensile strength, length, diameter, volume content, and shape.

- **Steel bars:** Young's modulus, tensile strength, and cross-section.

The experimental results also enable the numerical model to fit the behavior of the material (calibration). The notched beams were used to calibrate the bridging law due to the addition of fibers. Once the constitutive models are calibrated and describes correctly the behavior of the material, structural elements can be simulated.

As a preliminary step, the notched beams were simulated to calibrate and verify the numerical model. Afterwards, a real structural elements were tested to asses the applicability of the proposed method. In this research two beams were statically loaded to evaluate the performance of the proposed method. In the following sections both simulations are presented and analyzed detailedly.

7.3   Evaluation in small specimens

The tested notched beams were used as validation of the in-house FEM code, where the mechanical uncertainties were reduced significantly. These test allow to fit the numerical

results to the real behavior, in addition to giving information of the toughness and residual stresses. The validation of this results allow to address more complex structural elements.

The notched beams dimensions were 600 x 150 x 150 mm and they were loaded in the middle point of the beam until failure. Figure 7.2 illustrates the finite element model. The beam was meshed with standard element of 10 mm and around the notch the mesh was refined using elements of 1 mm of height.
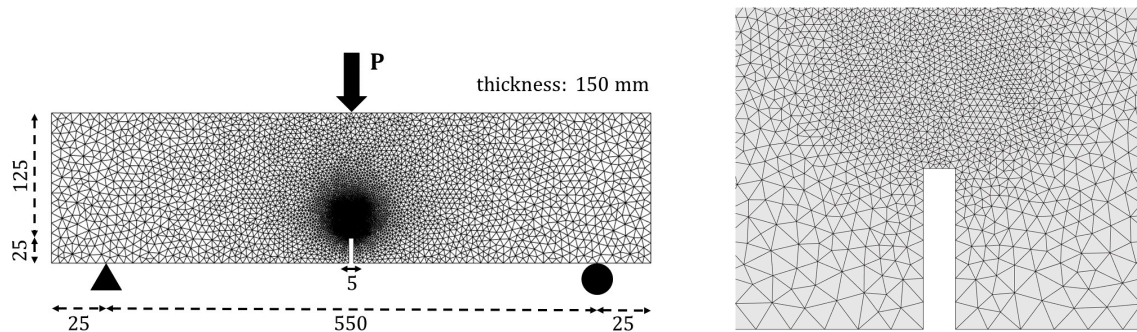

Fig. 7.2 Finite element model of tested notched beams

In the following points the numerical results are compared with the experimental results presented in the previous chapter. Furthermore in the case os SFRC beams, the corresponding parameters are fitted to simulate accurately the bridging effect of the fibers.

Notched beams made with EAFS (2T)

The EAFS concrete notched beam is used as a partial validation of the framework. The finite element model is modeled by the constitutive models for plain concrete described in Chapter 3 and Chapter 4. Table 7.1 reports the material properties defined through the test carried out at the University of Burgos. Bulk elements are defined by the elastic parameter of concrete while interface elements are determined through the tensile strength and the fracture energy.

Figure 7.3 illustrates the real load/CMOD curve of the test and the numerical curves. The numerical results are calculated through the tensile strength determined with the Dog-bone test and Brazilian test. As it is expected, the curve modeled through the data defined by the Dog-bone test fit better than the Brazilian test. This fact is due to the interface elements are damaged only by normal stresses to the base of the element. Dog-bone tests represent better this fracture mode (Mode I), than the Brazilian tests.

The numerical model also allows to motorize the crack development as it is showed in Figure 7.4. As concrete is a brittle material, just one main crack is developed as it can be also shown in the tests. The numerical model also displays this performance. The notched beam is cracked in the peak of the curve and afterwards, the crack is developed along the section of

Table 7.1 Material parameters used to model plain concrete notched beams with EAFS

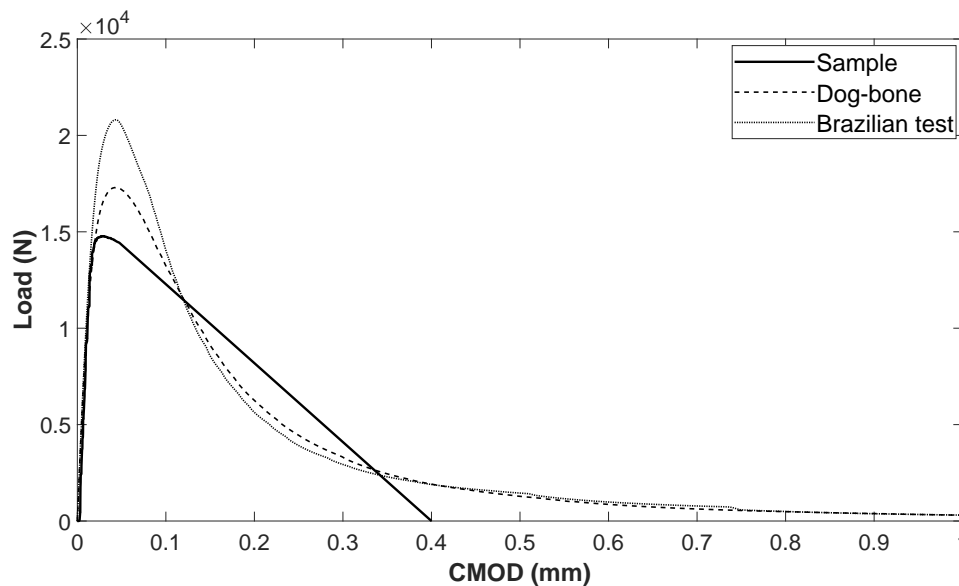| Bulk elements	
Young's modulus	40.1×10^3 MPa
Poisson's ratio	0.23
Interface elements	
Young's modulus	40.1×10^3 MPa
Poisson's ratio	0
Tensile strength (Dog-bone test)	4.25 MPa
Tensile strength (Brazilian test)	5.11 MPa
Fracture energy	0.137 N/mm

Fig. 7.3 Tested plain concrete notched beam Load/CMOD curve

the beam. The study of the crack development may be useful to evaluate the beam in terms of durability. Concepts such as crack width, crack depth and crack frequency, can affect for instance, the corrosion of steel reinforcement and the penetration of chlorides [114, 132].

The damage development can also be assessed through the quantification of the damage parameters of the interface elements as it is showed in Figure 7.5. Most of the damage is caused before getting the maximum value of the load. At the peak, the damage level reaches approximately 80%. Afterwards, most of the energy introduced into the system is dissipated through deformation. The quantification of damage is a useful tool to evaluate the state of the beam.
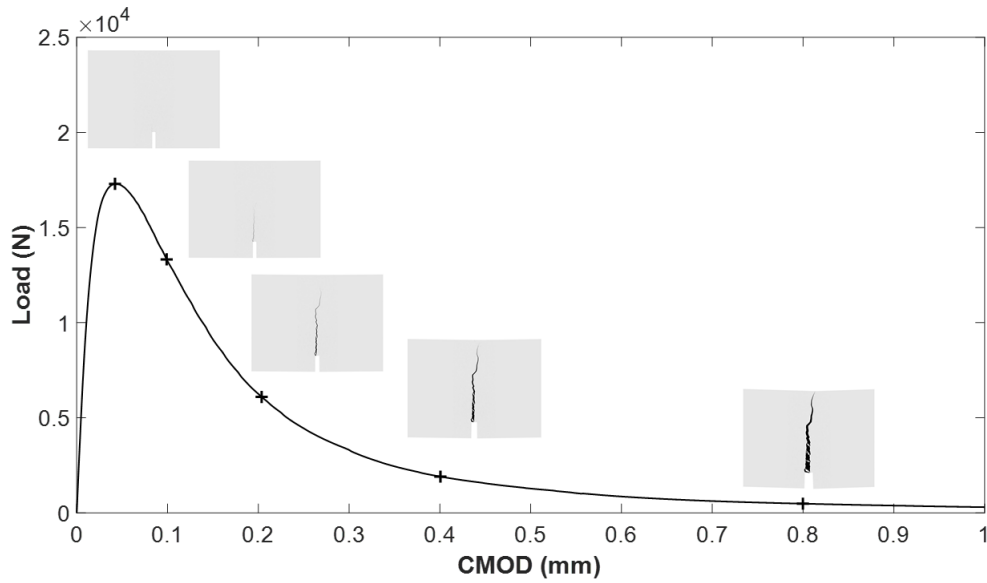
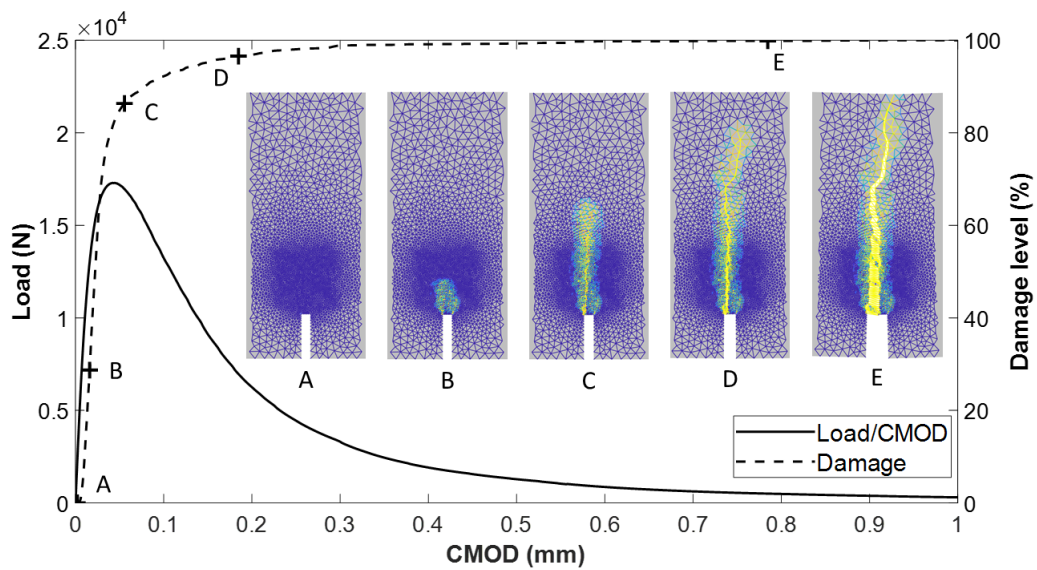Fig. 7.4 Fracture development during the loading

Fig. 7.5 Damage development during the loading

Notched beams made with EAFS and reinforced with steel fibers (2M)

The SFRC notched beam was used as an intermediate step to fit the numerical result to the experimental results. The parameters used to define the model are presented in Table 7.2. The modulus of Young is the elastic modulus of the composite and it is presented in the previous chapter. The introduced tensile strength was defined by the dog-bone test and it is obviously the tensile strength of the composite. The properties of the interface elements are

based on the characteristic of the fibers defined in the technical documentation detailed in Table 5.1.

Table 7.2 Material parameters used to model SFRC notched beams with EAFS

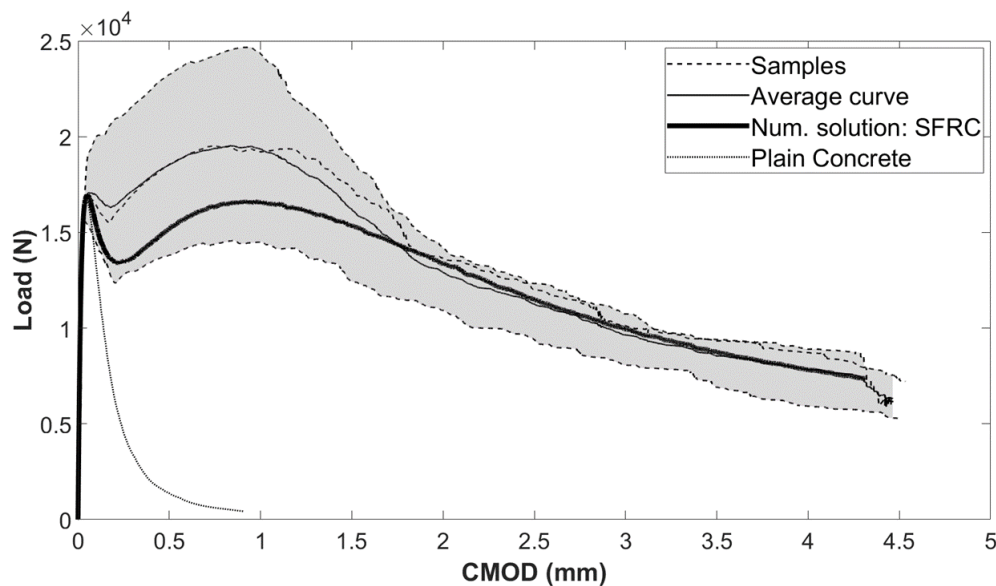| Bulk elements	
Young's modulus	34.7×10^3 MPa
Poisson's ratio	0.22
Tensile strength (Dog-bone test)	3.77 MPa
Tensile strength (Brazilian test)	4.84 MPa
Tensile fracture energy	0.137 N/mm
Interface elements	
Young's modulus	210×10^3 MPa
Poisson's ratio	0
Tensile strength	1,200 MPa
Fiber length	35 mm
Fiber diameter	0.55 mm
Volume content	0.5%
Shape	Hooked-end

Fig. 7.6 Tested 2m notched beam Load/CMOD curve

Figure 7.6 compares the numerical solution with the experimental measurements, it is also included the simulation of the beam without fibers to show the bridging effect of the fibers. It reveals a clear trend between the experimental and numerical solution especially

in the prepeak stage and the softening stage. After the first peak there is a decline due to concrete cracking and activation of steel fibers. This decline is sharper for the numerical results than for the mean curve. However, the drop in the load is not so sharp compared to the real behavior (samples). The numerical solution remains within the range during the whole loading history.
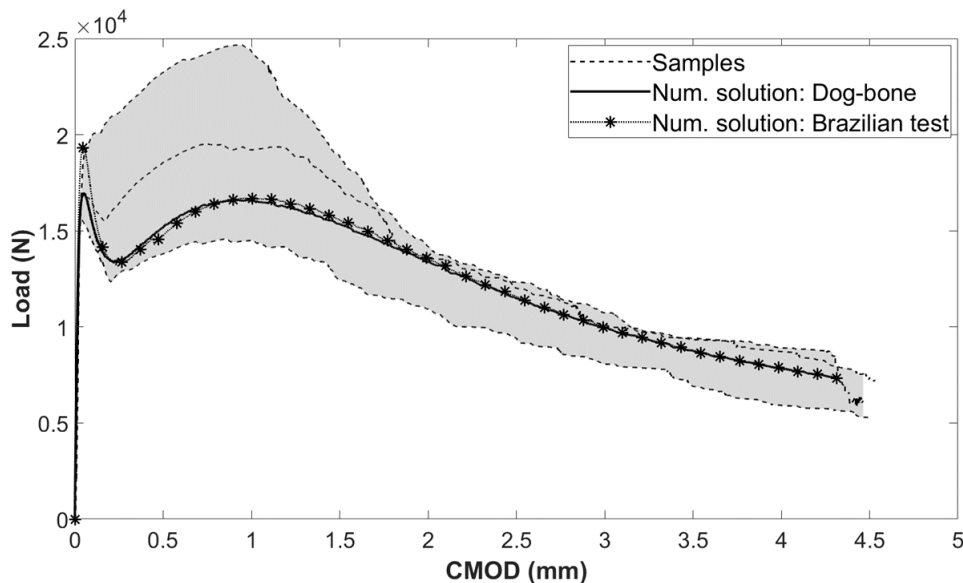

Fig. 7.7 Comparison of 2M notched beams modeled with tensile strength obtained through Dog-bone and Brazilian test

Focusing on the first stage of the curve (prepeak), the mechanical behavior is mainly described by the tensile strength and the elastic modulus of the composite. The difference of the elastic modulus of the composite and the plain concrete is negligible. Meanwhile, the tensile strength was calculated through two different methods, dog-bone test and Brazilian test. The tensile strength calculated through dog-bone test (direct tensile test) were slightly lower than the ones determined through the standardized method, Brazilian test (indirect tensile test).

Nevertheless, the use of interface element to simulate the bridging effect required the introduction of a tensile strength. The implemented damage model assumes that the element are damaged through perpendicular loads to the base of the triangle element. This method to simulate fracture can be considered as Mode I fracture (tension mode), where the loads are applied normal to the crack. Despite the fact that Brazilian test is the common and normalized method to calculate the tensile strength, the particularities of the model requires the tensile strength calculated through direct method. Thus, the tensile strength determined

by dog-bones test was introduced in the damage model. Figure 7.7 compares the load/CMOD curves calculated through both tensile strengths.
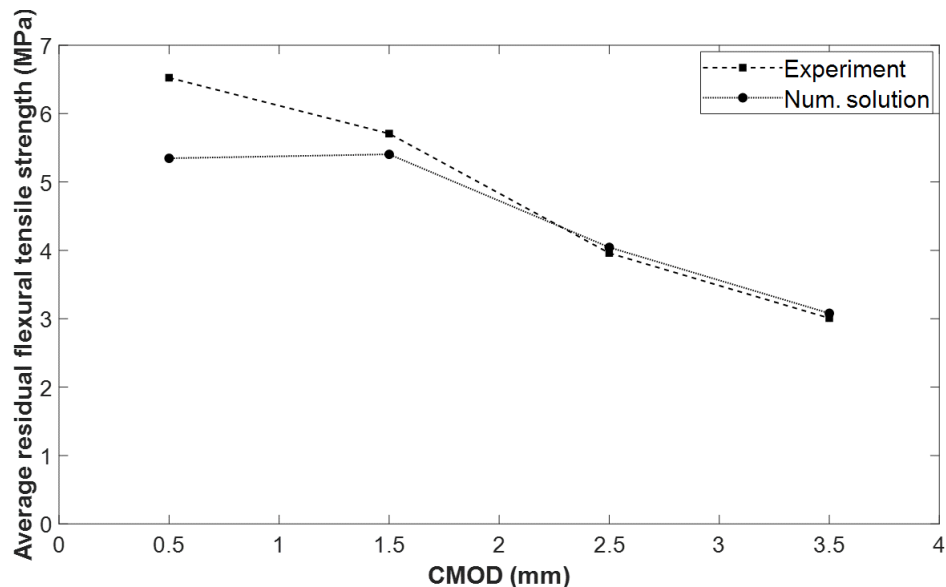

Fig. 7.8 Toughness index of numerical and experimental results

The softening stage depends on the properties and the quantity of the fibers reported in Table 7.2. Figure 7.6 shows the numerical results of plain concrete and SFRC, which allow to view the effect of the fibers. The bridging law giving by the Equation 3.61 has parameter that have to be calibrated to fit to experimental curves. The parameters of the bridging law assumed were $t_1 = 0.6$, $t_2 = 1.45$, $c_1 = 1.7$ and $c_2 = 2.0$ for SFRC made with EAFS. This test is used to calibrate material models which permits to go ahead with more complex mechanical behavior.

Focusing on the residual behavior, Figure 7.8 compares the residual strength of the experiment and the numerical results. The difference of the stresses at CMOD of 0.5 mm is considerable, about 20%. This difference is reduced along the CMOD, decreasing the difference from 8% at CMOD of 1.5 mm to being almost the same.

The FEM allows to quantify every parameter of the model at every pseudotime-step, for instance, the damage level. The parameter that determines the damage level of the beam was determined based on the damage coefficients of each finite element (0-1). Figure 7.9 shows the evolution of the damage of the notched beam and the damage level of each interface element. The elements are damaged mainly in the first stages of the loading (A-D). At the beginning, the elements are damaged near the notch and the loading point. The damage evolves up to the crack crosses the beam while increasing the CMOD. In a second
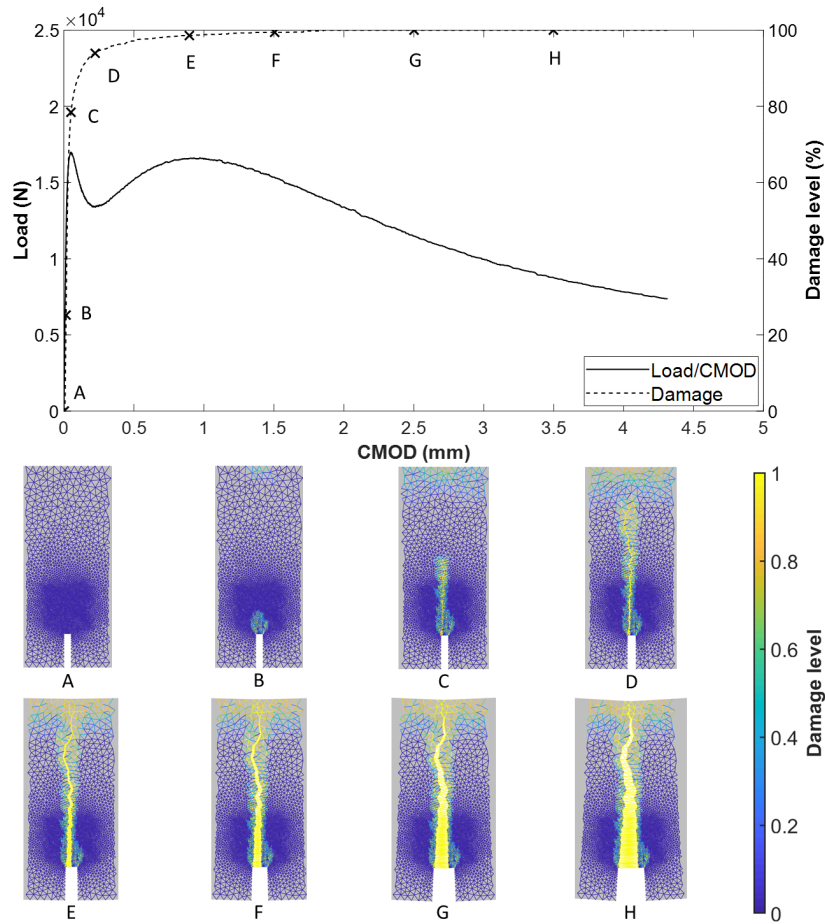
Fig. 7.9 Damage evolution of 2M notched beams

phase (E-H), the introduced energy is dissipated due to strain and the damage increases insignificantly.

Therefore, it is proved that the model is suitable to simulate the bridging effect and the fracture of SFRC made with EAFS. Furthermore, it can be considered that the model is calibrated through the information measured in the three samples. The numerical curve was fitted to the average curve through the variables t_1, t_2, c_1 and c_2 an the material parameter described in Table 7.2. The numerical curve differed from one of the samples, which displayed a hardening effect after the first peak, and best suited to the other two curves. It is noted that the numerical solution fits better when the tensile strength determined through dog-bone test is used.

Notched beams made with EAFS and reinforced with synthetic fibers (2S)

Table 7.1 reports the material properties that define the constitutive model for the mix 2S. The softening branch due to the addition of synthetic is defined by the parameters $t_1 = 0.1$,

Table 7.3 Material parameters used to model 2S notched beams

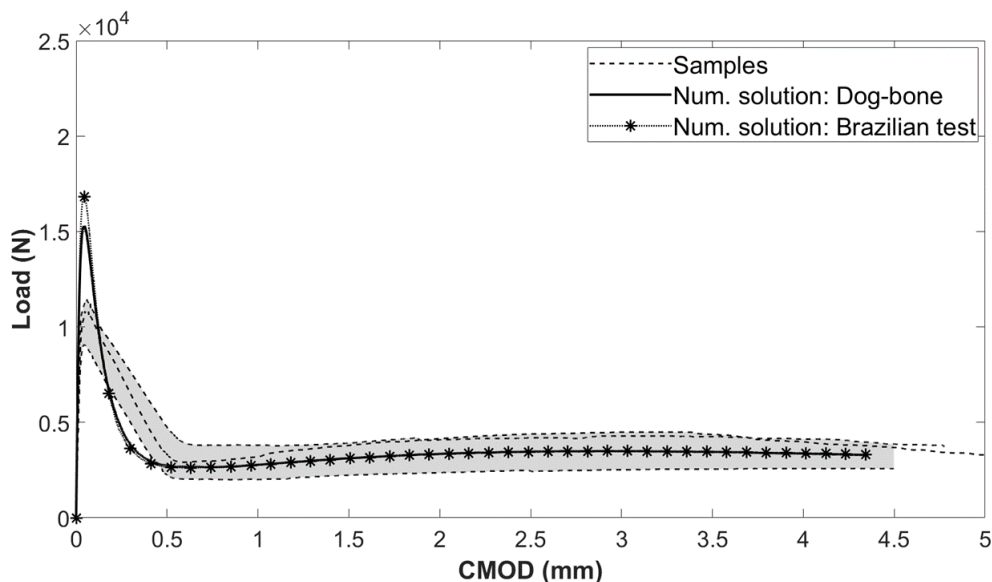| **Bulk elements**	
Young's modulus	31.6×10^3 MPa
Poisson's ratio	0.22
Tensile strength (Dog-bone test)	3.66 MPa
Tensile strength (Brazilian test)	4.35 MPa
Tensile fracture energy	0.137 N/mm
Interface elements	
Young's modulus	6×10^3 MPa
Poisson's ratio	0
Tensile strength	400 MPa
Fiber length	35 mm
Fiber diameter	0.93 mm
Volume content	0.5%
Shape	Dimpled-surface

Fig. 7.10 Comparison of 2S notched beams modeled with tensile strength obtained through Dog-bone and Brazilian test

$t_2 = 0.2$, $c_1 = 1.0$ and $c_2 = 0.6$. This test was mainly used to fit the numerical curve to the experimental results through the mentioned parameters.

Figure 7.10 compares the numerical results and the experimental results. The numerical curves are defined through the tensile strength calculated in the Dog-bone tests and Brazilian test. The curve defined by the direct tensile strength gives more accurate results as it was also reported previously.

However, the peak of the numerical results is about 50% greater than the experimental curves. Further studies are need to study this difference. The softening part of the curve are quite similar due to little relevancy of the synthetic fibers. The residual stress are not as significant as for mixes with steel fibers (2M and 3M).
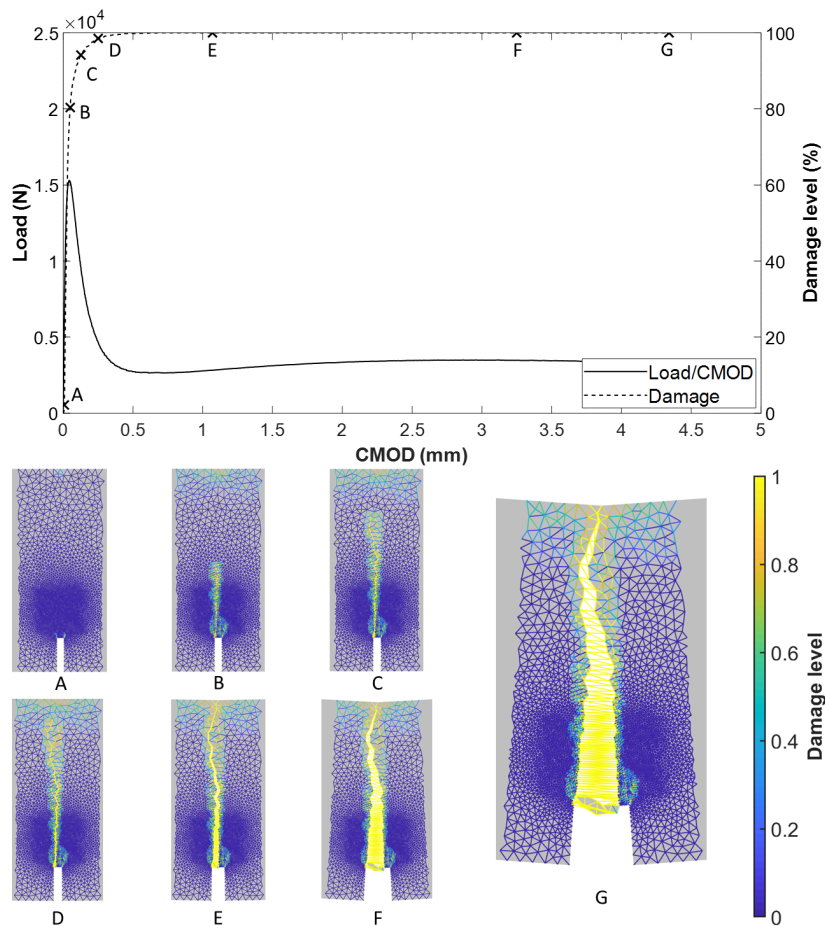

Fig. 7.11 Damage evolution of 2S notched beams

Figure 7.11 shows the development of the damage in the interface elements. The notched beam is damaged earlier compared to the sample 2M. The beam is almost damaged after the peak (Point A-D). After the Point D the beam is almost damaged, the crack opening

increases rapidly. As it has been deducted during the research work, the synthetic fibers does not produced an improvement as the steel fibers does.

Notched beams made with EAFS and reinforced with steel fibers (3M)

Table 7.4 Material parameters used to model 3M notched beams

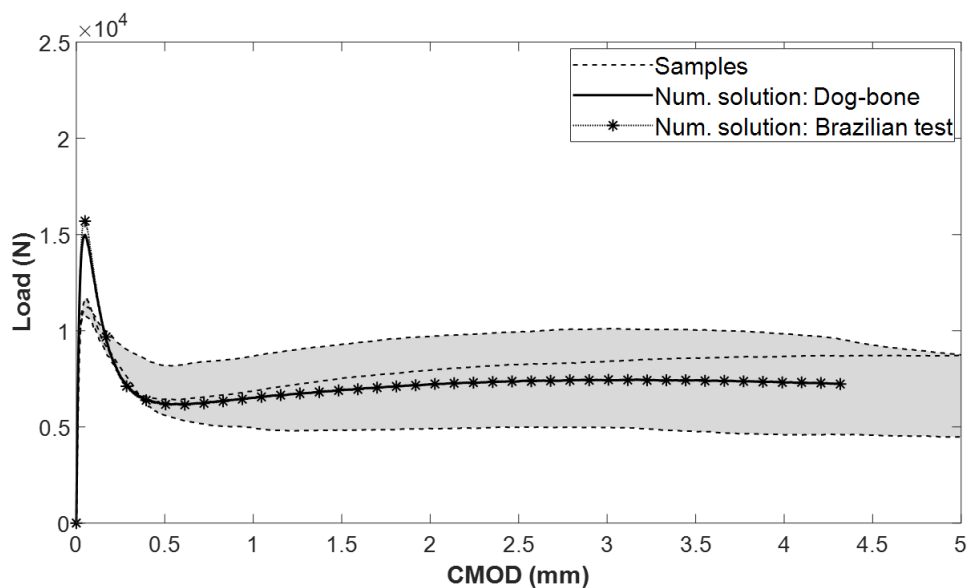| Bulk elements	
Young's modulus	26.1×10^3 MPa
Poisson's ratio	0.19
Tensile strength (Dog-bone test)	3.14 MPa
Tensile strength (Brazilian test)	3.36 MPa
Tensile fracture energy	0.137 N/mm
Interface elements	
Young's modulus	210×10^3 MPa
Poisson's ratio	0
Tensile strength	1,200 MPa
Fiber length	35 mm
Fiber diameter	0.55 mm
Volume content	0.5%
Shape	Hooked-end

Fig. 7.12 Comparison of 3M notched beams modeled with tensile strength obtained through Dog-bone and Brazilian test

Material parameters requested by the constitutive model are defined in Table 7.4. These parameters were defined through the experimentation presented in Chapter 5 and 6. The softening branch of the mix 3M is defined by the parameter $t_1 = 0.5$, $t_2 = 0.4$, $c_1 = 0.4$ and $c_2 = 0.5$. These parameters enables mainly fitting the residual behavior of the composite.

In this case, the indirect and direct tensile strength are quite similar. Due to this fact, the curves illustrated in Figure 7.12 are also similar. Although the difference between the tensile strengths is insignificant, the tensile strength determined through the Dog-bone test is slightly lower. As happened in 2S, the peak of the curve is greater than the experimental curve but the softening branch is well-captured. The softening branch in contrast to the mix 2M, does not show a hardening behavior due to the addition of steel fibers. However, the residual strength is greater than the mix 2S.
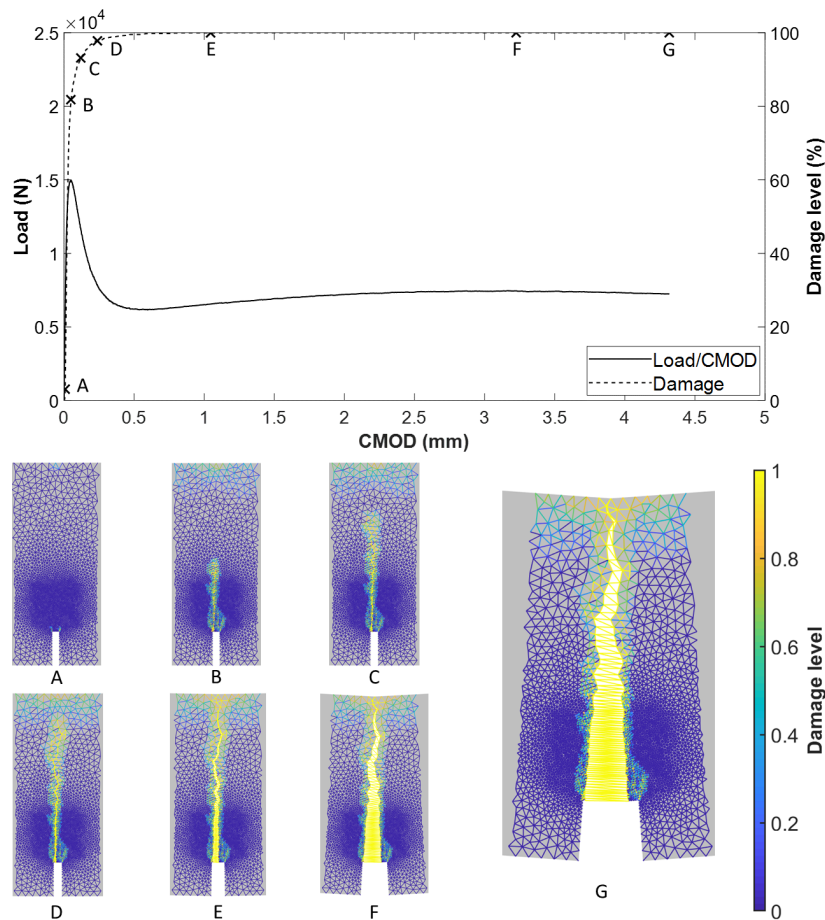

Fig. 7.13 Damage evolution of 3M notched beams

Figure 7.13 shows the development of the damage parameter through a range of snapshots at certain loading steps. The development of damage is more similar to the mix 2S than to the mix 2M. As there is not a hardening behavior after the peak, the notched beam is almost

damaged after the peak. The crack opening takes place mainly after interface elements are damaged (loss strength).

7.4   Full-scale test

7.4.1   Large-scale test set up

Fig. 7.14 Flexural beam set up

Concrete beams for flexural using were tested to evaluate the performance of the material and the numerical model. The experimental program consisted of four beams having rectangular cross-sections of 200 x 300 mm^2 (width x height) and length of 4,400 mm. The beams were simply supported (rollers at both ends) and the span was of 4,000 mm. The beam was subjected to a four-point load, according to Figure 7.14, with a distance between the loads of 1,000 mm.

The specimen was designed to evaluate the performance of fibers. To this end, the longitudinal reinforcement consisted of 2 ϕ16 bars in on the bottom part while 2 ϕ8 bar were placed at the top part. The transverse reinforcement consisted of ϕ8 hoops spaced 150 mm. Figure 7.15 shows the detailed settings of the beam.

The tests were conducted with deflection control at three different ranges:

1. Load step of 0.5 mm at 0.5 mm/min was applied until the first cracks were detected.

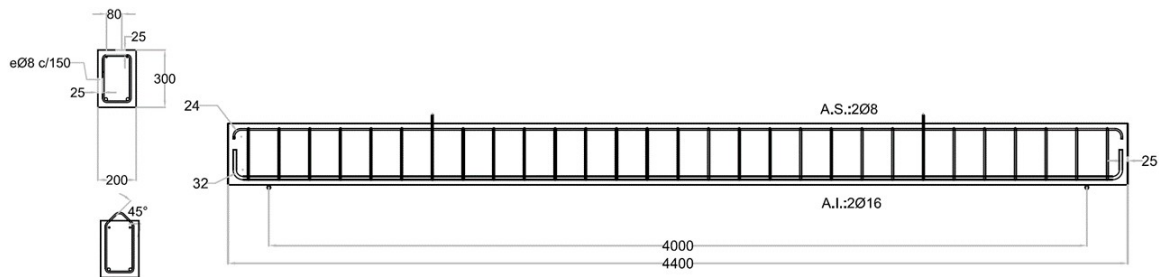2. Load step of 1 mm at 1 mm/min was applied while the cracking.

Fig. 7.15 Plans of the tested beams

3. Load step of 2 mm at 2 mm/min was applied when the cracks were generated up to the end of the test.

The load, support settlements and the strain at the mid-span were measured during the tests as it is showed in Figure 7.16. The cracks were painted while the tests were being carried out.
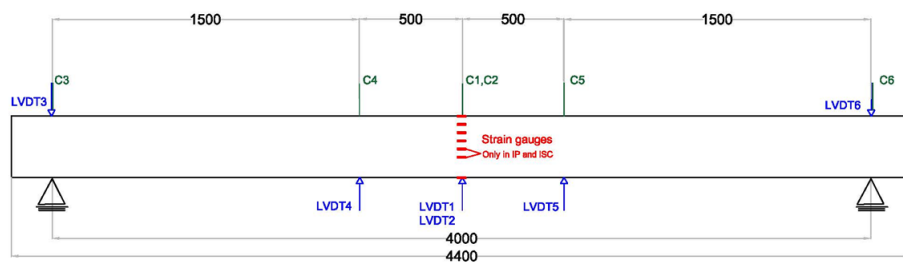

Fig. 7.16 Four-point bending beam tests

7.4.2 Large-scale experimental results

Figure 7.17 illustrates the the load/displacement curves of the four mixes. The displacement was measured at the middle point of the beam through a gauge placed at the mentioned point.

The mixes with fibers (2M and 2S) required higher load to fault than 2T. It is worth noting the beneficial effect of steel fibers which increased the failure load in 35% while the addition of synthetic fibers increased in 17% the failure load.
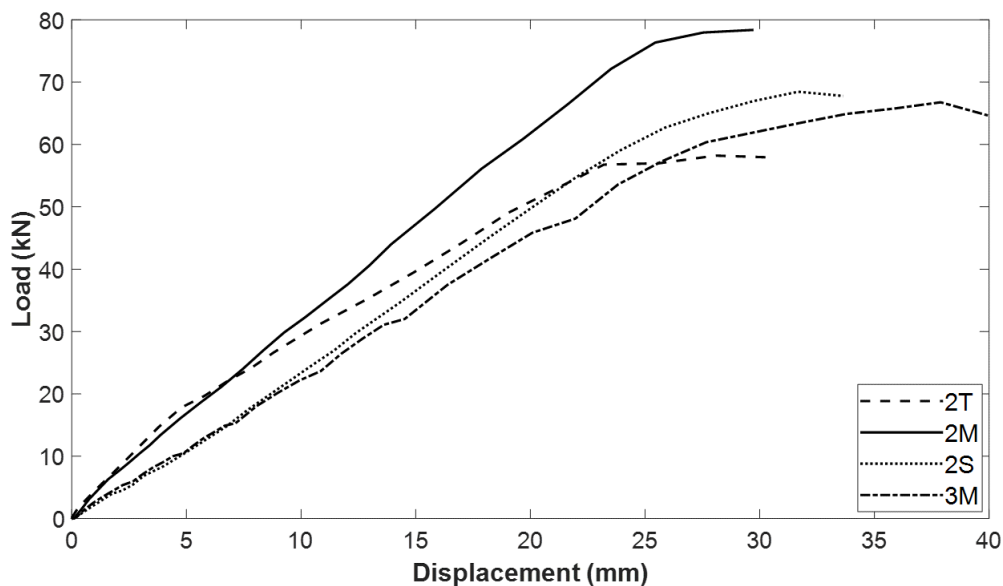
Fig. 7.17 Load/deflection curves of the beam

The mix 3M showed greater values of failure load than 2T despite the used cement. The addition of steel fibers allowed to gain almost the same strength of 2S. As it was reported in the experimental results presented in Section 6, the mix 3M showed the lowest stiffness.

7.4.3 Large-scale numerical results

In this section the described beams are modeled with the constitutive models presented along the dissertation and the obtained results are presented and studied. Figure 7.18 illustrates the finite element model where the longitudinal and shear reinforcement are drawn in blue and red color respectively. The linear element are arranged as it was explained in Section 5 [167]. The beam is meshed with triangular elements of 20 mm height and interface elements of 0.001 mm height are introduced along the beam.

In the left support the vertical and horizontal displacements are constrained while in the right support only the vertical displacement is constrained. The beam is loaded in two point as it is showed in Figure 7.14.

Reinforced concrete beam made with the mix 2T

The studied beam is constituted by the mix 2T (without fibers) and the inputs required by the numerical models are reported in Chapter 6.

Figure 7.19 illustrates the load/displacement curve at the middle point of the beam. The numerical model shows greater stiffness at the first stage up to concrete loses the strength in
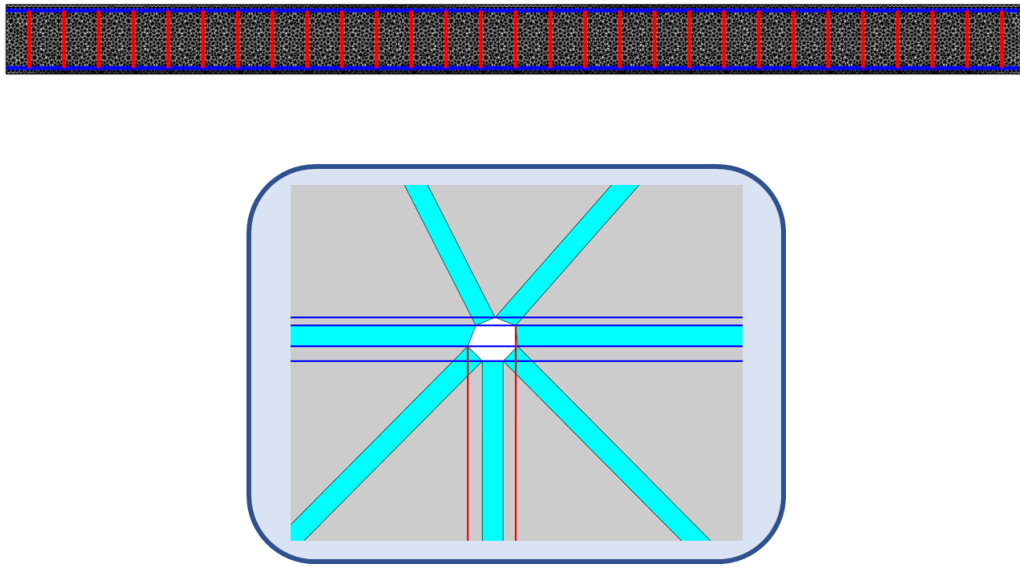
Fig. 7.18 The general mesh and the arrangement of the reinforcement
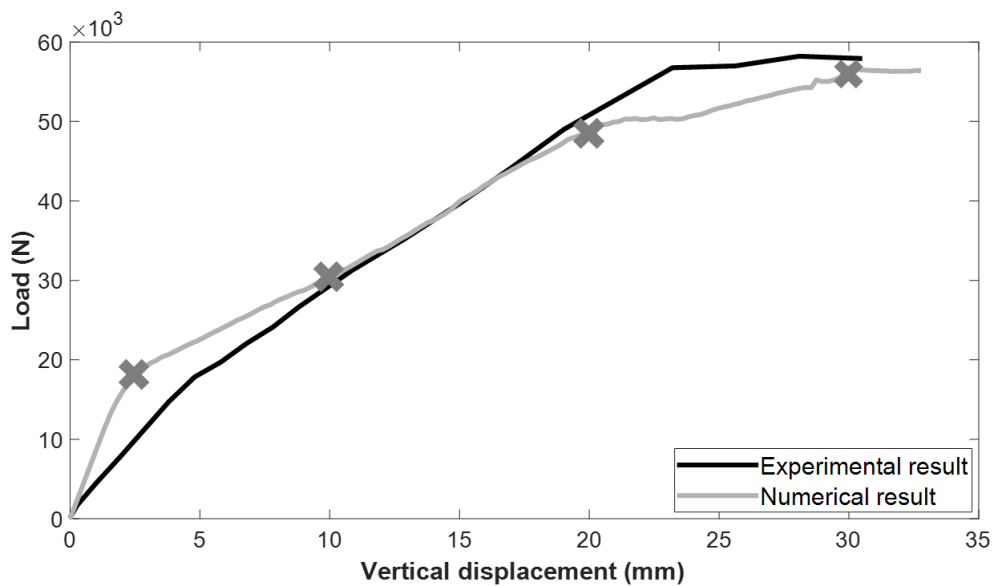
Fig. 7.19 Load/deflection curves of the beam made with the mix 2T

the tensile part (lower part of the cross section). After this point the strength of the beam in the tensile part is due to the steel bar, giving rise to change in the slope of the curve. The numerical curve shows less steeper curve which means that the steel bars are less stiffer than the reality. This will be a fact to improve in future studies. Lastly, the maximum load are quite similar in both cases, although the experimental curve reaches its highest value earlier.

The stress in the beam at the failure point is showed in Figure 7.20. The maximum values are in the compressive part of the beam, while the stresses of the bulk elements are lower
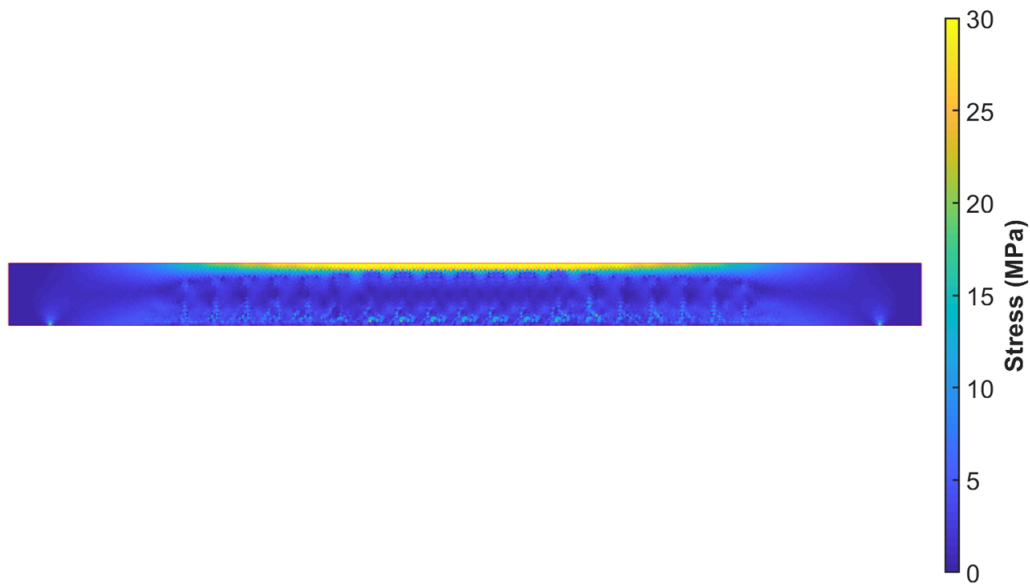
Fig. 7.20 Stress state at the last pseudo-time step

due to the implemented damage models in the tensile part. This highlights the need for implementing elastoplastic models for concrete. In the supports it can also be seen other stress concentration points as it is expected.

Fig. 7.21 Damage development in the beam made with the mix 2T

Examining the damage level of intermediate elements, the degradation of concrete elements can be studied. Figure 7.21 shows the evolution of the damage by four snapshots at the loading point indicated in Figure 7.19. In the first stage the damage is concentrated in the

Fig. 7.22 Cracking of beams made with the mix 2T

middle part of the beam and then damage is spread along the beam. The damage is focused on elements located perpendicularly, generating preferential bands. At the first the elements are damaged and the vertical displacement of the beam is more evident at the last stages.

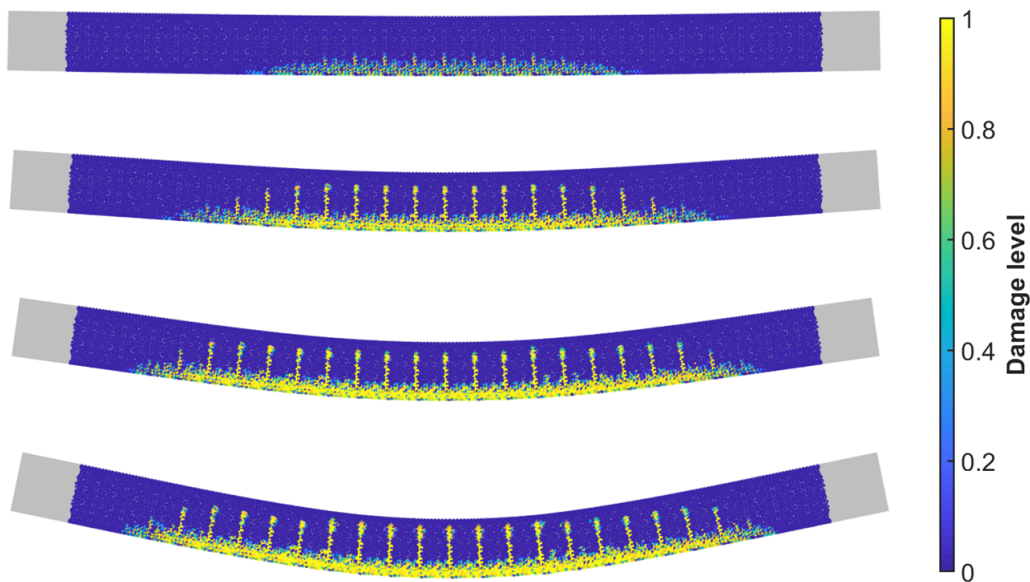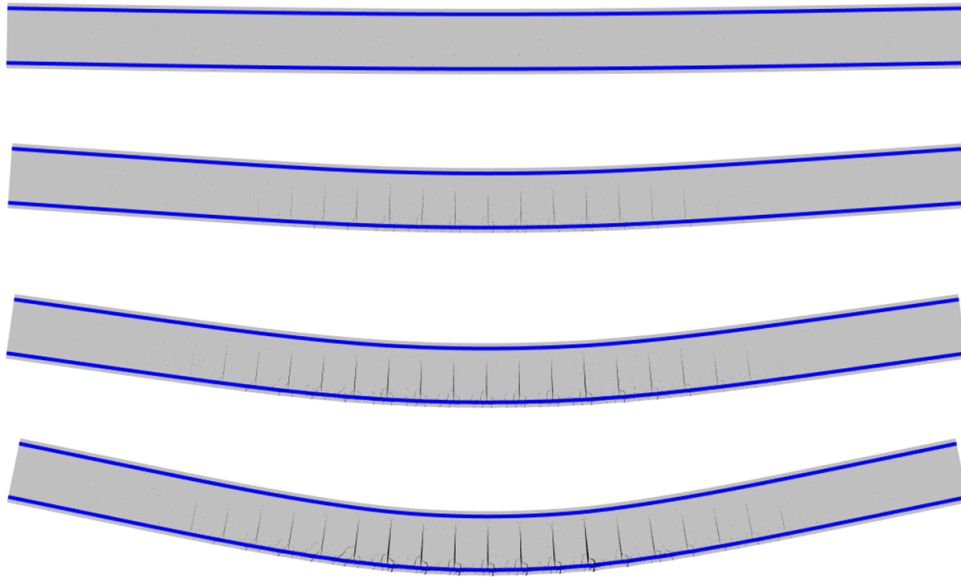Figure 7.22 shows the development of the cracks in the beam, where the displacements have been majored to facilitate the visualization of the cracks. One main perpendicular crack is generated in the beams every 150 mm and inclined secondary cracks are also developed. The numerical model allows to measure the depth and opening of the cracks, which might be an interesting point to study penetration of corrosion. This fact might be useful to evaluate the durability of the beam, for instance in marine environment.

Reinforced concrete beam made with the mix 2M

The tested beam in this point is made with the mix 2M (with steel fibers) and the properties of the mix are defined in Table 6.11. Figure 7.23 shows the load/displacement curve of the beam. The numerical curve show similar behavior to the numerical behavior of the beam without fibers. At the first stage, the slope of the numerical behavior is steeper than the experimental curve. After the failure of concrete in the tensile part, the beam is less stiffer than the real beam. In this case, the numerical failure load does not get the load of the experiment.

The fracture mode of beam with steel fibers is completely different to the one without steel fibers. The damage is spread along the beam due to the addition of fibers, which redistributed the stresses [47]. Figure 7.24 shows the evolution of the damage in the interface elements at the loading point indicated in Figure 7.23. At the first stages, the cracks are

Fig. 7.23 Load/deflection curves of the beam made with the mix 2M
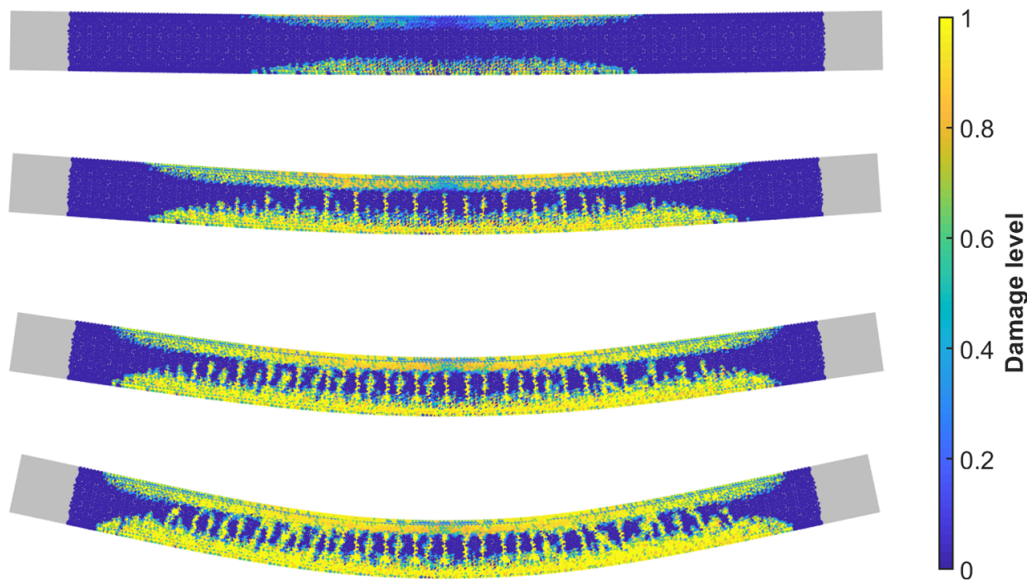
Fig. 7.24 Damage development in the beam made with the mix 2M

separated by 150 mm. However, in the last two snapshots another crack is generated between the initial cracks. All the cracks are developed up to the upper side of the beam, which is another difference from the beam without fibers.

Figure 7.25 shows the developed cracks at the loading step marked in Figure 7.23. The beam is more fractured compared to the beam made with the mix 2T. The early cracks are generated in the flexural part of the beam and they are developed vertically. However, the
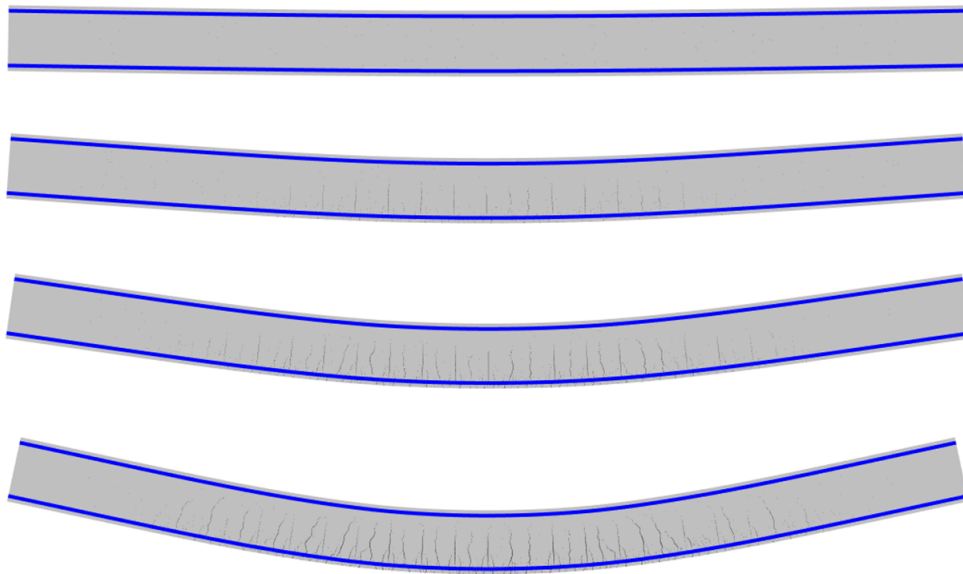
Fig. 7.25 Cracking of beams made with the mix 2M

cracks located closer to the supports tend to incline due to the shear stresses that take place. In this figure can also be appreciate the larger amount of cracks generated along the beam.

It can be concluded that the beam bears greater load despite the beam is more damaged than the beam 2T. The fibers are the responsible of spreading the damage along the beam due to the hardening behavior showed by the material in Section 7.3.

Reinforced concrete beam made with the mix 2S

The beam made with the mix 2S (synthetic fibers) is also modeled following the presented framework. Figure 7.26 compares the load/displacement curves of the experiment and the simulation. The numerical model fails close to the vertical displacement of 35 mm. After this point the numerical model shows anomalous behavior due to the high damage range of interface elements. The numerical curve shows higher rigidity than the experimental curve in the first loading steps. However, the stiffness decreased becoming less stiffer than the real beam. This behavior is in accordance with the previous results.

Damage is more distributed than the beam made with the mix 2T, while it is not as distributed as the mix 2M. Figure 7.27 shows the evolution of the damage at the loading steps pointed in Figure 7.26. In this case, it is not developed a secondary region of damaged elements as in the case of the mix 2M. In the middle zone of the mix (pure bending) the damage regions are vertical while close to the supports the damaged regions are inclined due to shear stresses.
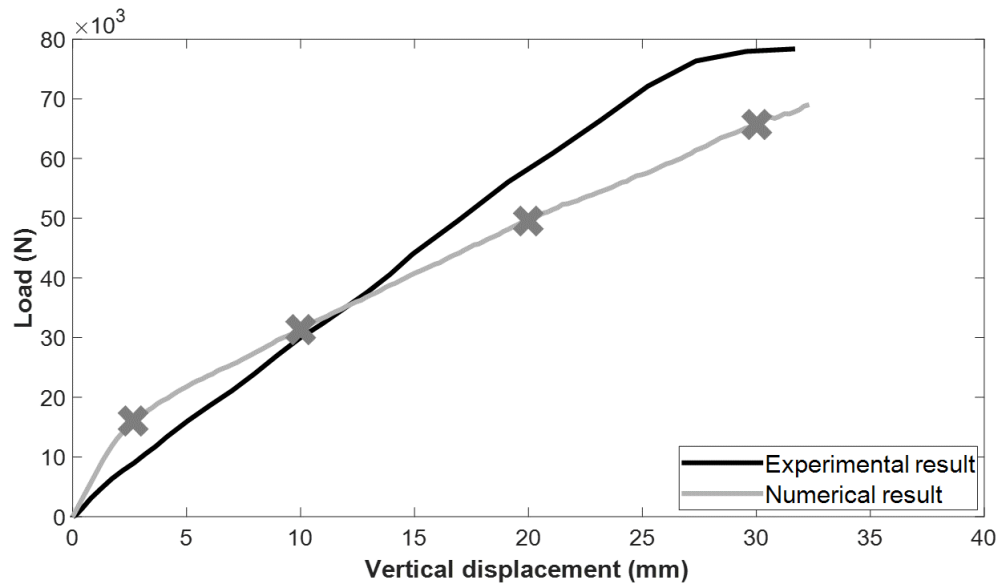
Fig. 7.26 Load/deflection curves of the beam made with the mix 2S
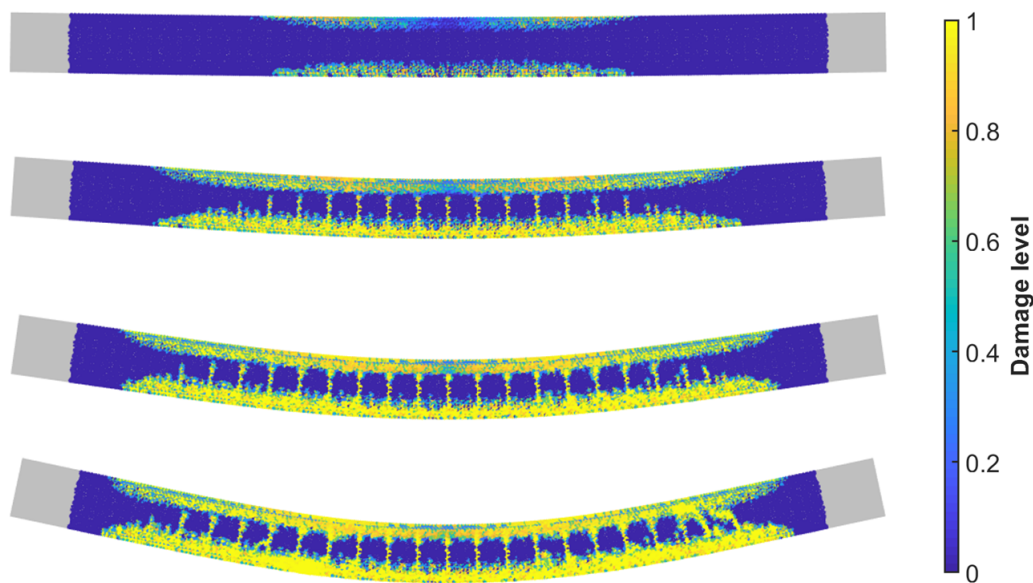
Fig. 7.27 Damage development in the beam made with the mix 2S

Figure 7.28 shows more clearly the development of the crack at the same loading points and the followed cracking paths. In the first loading point, the elements are damaged but it is not developed any crack. Afterwards the cracks are developed rapidly and distributed along the reinforcement bar. It is also visible the different cracking paths developed in the pure-bending zone and in the zone subjected to bending moments and shear forces.
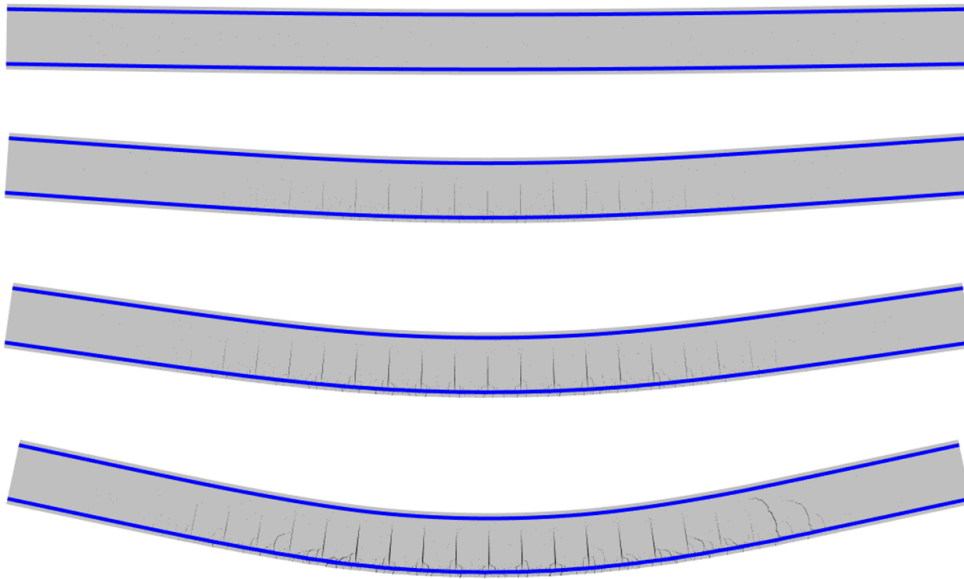
Fig. 7.28 Cracking of beams made with the mix 2S

Reinforced concrete beam made with the mix 3M

In this section the performance of the presented framework is assessed through a beam made with the mix 3M. This mix is distinguished from the other mixes by the lower values of the Elastic Modulus. This fact means that the slope of the curve is less inclined and it seems that numerical result is closer to the experimental curve as it is showed in Figure 7.29. The numerical analysis cannot be carried out up to the displacement of 40 mm. The numerical model fails earlier than the experimental result.

Figure 7.30 shows the development of damage at the loading steps pointed in Figure 7.29. Damage is less distributed than the beam made with the mix 2M. In this case is not completely developed a secondary damage region between the main damage zones. The beam is more damaged than the the made with the mix 2S and less damaged than the beam made with 2M.

The crack development is studied in Figure 7.31. The central cracks developed in the central zone of the beam are vertical due to the the bending moments in this region. The cracks tend to tilt due to the shear loads near the supports.
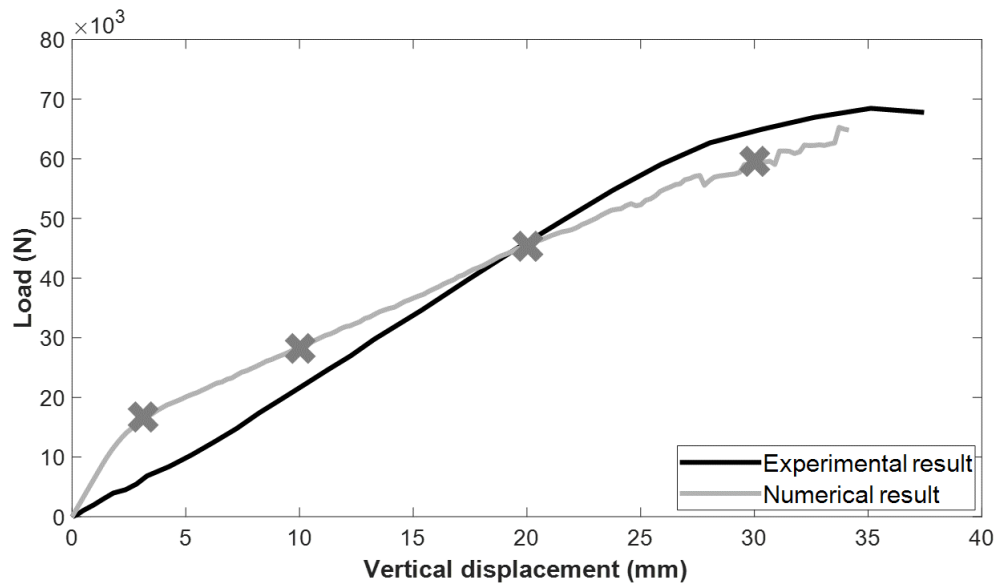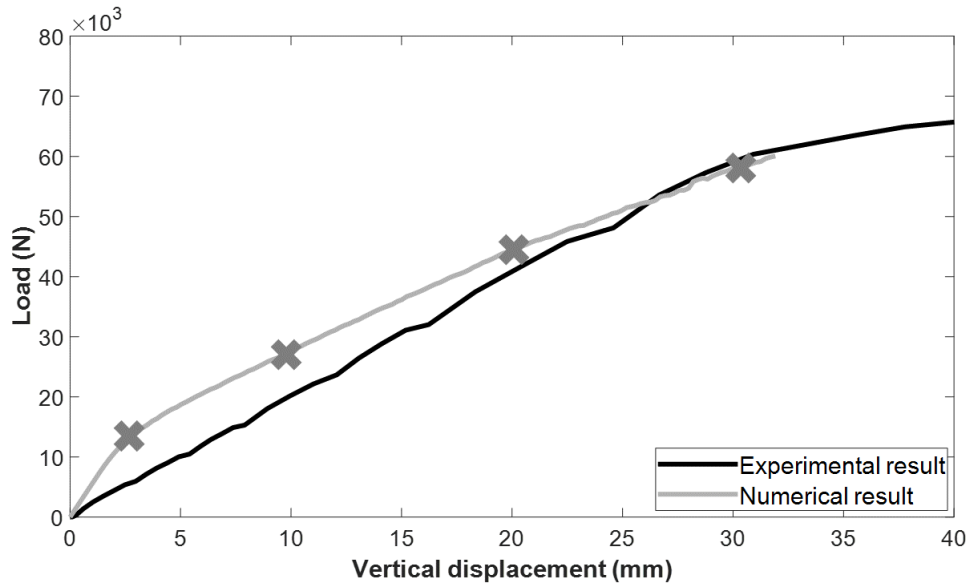
Fig. 7.29 Load/deflection curves of the beam made with the mix 3M
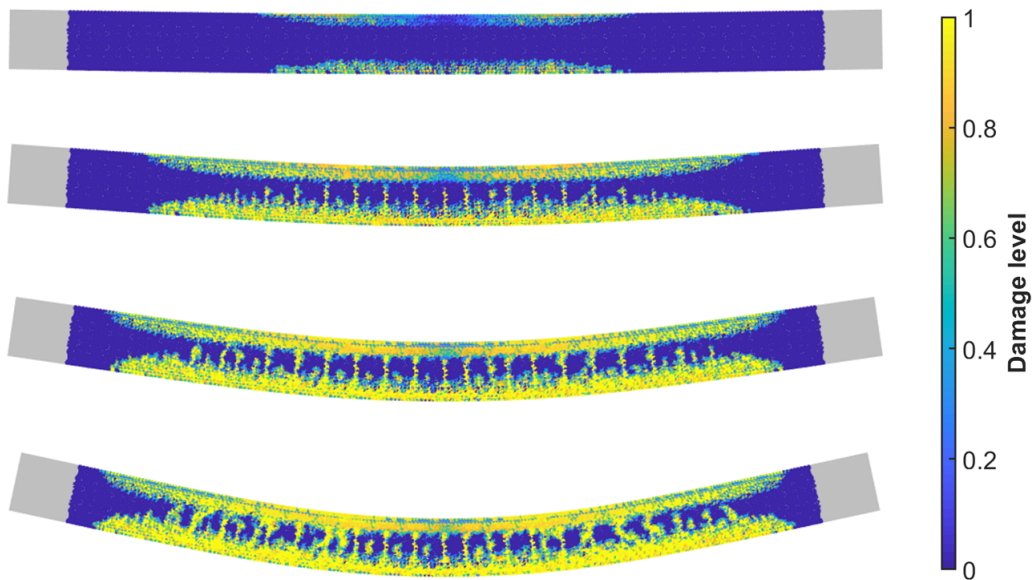
Fig. 7.30 Damage development in the beam made with the mix 3M
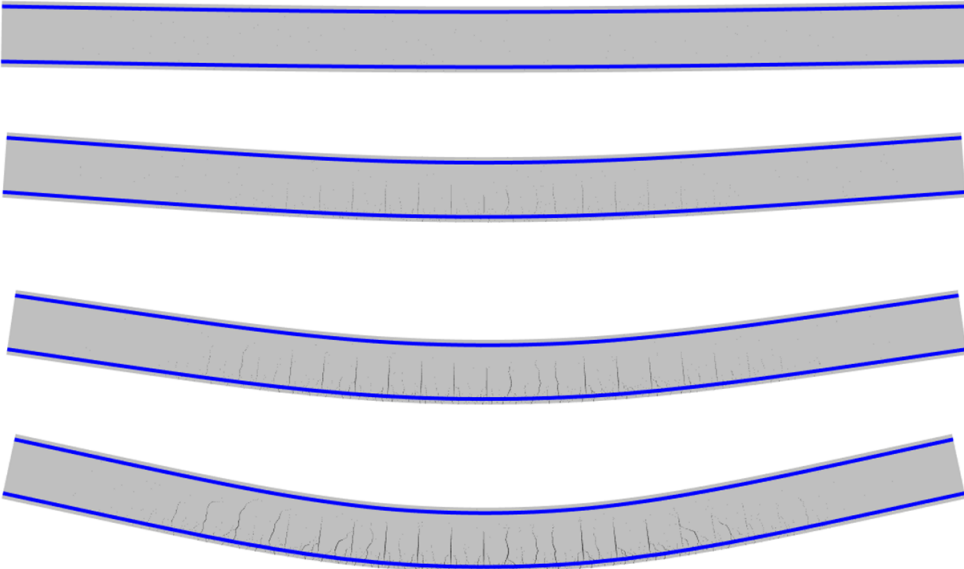
Fig. 7.31 Cracking of beams made with the mix 3M

Chapter 8

Conclusions and future works

8.1 Introduction

The dissertation consisted of experimental and computational studies to provide insight into the behavior of fiber reinforced concrete. A framework to design structural elements is presented and applied to calculate the behavior of four-point bending beam. The conclusions of the research and suggestions for future studies are presented in this chapter.

8.2 Conclusions

This study introduces a finite element approach for predicting the physical behavior of fiber reinforced concrete members subjected to static loading. The effect of fibers is modeled using zero-thickness interface elements and the appropriate constitutive model (bridging law). The degradation of plain concrete is also modeled using the same technique but changing the damage model (tensile damage model).

Elastoplastic constitutive model with strain hardening (Menegotto-Pinto model) is implemented to model the behavior of steel reinforcement. The discretization is carried out replacing each linear element by a number of linear elements defined by the number of triangular elements that shared the nodes. This enables the cracks crossing the reinforcement bars. It is also assumed that the steel bar are perfectly bonded into the concrete.

All these are implement in an in-house FEM code in an attempt to describe the physical behavior of fiber reinforced concrete. The aforementioned constitutive models are presented and the implementation of them in the in-house code is also explained in the dissertation. Implicit/Explicit (IMPL-EX) integration scheme is provided in order to integrate the consti-

tutive models. In order to asses the numerical models, a set of benchmark problems have been modeled.

The inputs required by the numerical models are determined through experimentation carried out at the Laboratory of Large Civil Engineering Structures at the University of Burgos. Among all tests, it is worth noting the dog-bone test, which is out of standards and it is designed exclusively for the research work. The experimentation is also used to study the performance of four different mixes (2T, 2M, 2S and 3M). The used material is characterized by the replacement of natural aggregates by EAFS and the addition of fibers (synthetic and steel fibers). The designed testing campaign assesses the material in terms of durability and mechanics and the main conclusions were:

- Self-compacting and pumpable mixes were designed despite the disadvantage of the high weight of EAFS. Furthermore, the mixes were also characterized by the use of fibers and ground granulated blast furnace. With these requirements, the performance of four mixes were assessed throughout the dissertation.

- In terms of durability, the addition of fibers, specially steel fibers, affected the internal structure of concrete (porosity and connectivity of pores) facilitating the penetration and spread of chemicals agents. It was also reported that synthetic and steel fibers shows similar performance. In this context, it was also reported that other factor, such as the w/c ratio, had also influenced in the internal structure. The tests had also concluded that the mix with ground granulated blast furnace showed the worst performance as it was expected.

- From a mechanical point of view, fibers influenced mainly the tensile behavior (Fracture energy, toughness and residual stress) of the mixes changing the failure mode from brittle material to ductile material. In particular, the positive effect of steel fibers must be reported improving remarkably the postpeak behavior.

- Tensile strength of the mixes were determined through Brazilian test (indirect method) and Dog-bone test (direct method). The Dog-bone test as it was not normalized and commonly used in construction, the specimen and molds had to be designed to carry out this test. The direct method represented better the fracture mode (Mode I) modeled through the implemented damage models. It was showed that the tensile strength calculated through direct method enable to get more accurate results in notched beams.

- A framework for the design of fiber reinforced concrete was presented and applied to study the structural behavior of beams. An experimental campaign and a numerical tool was provided to leap from material scale to structural scale.

- The numerical models were able to capture the failure mode due to the addition of fibers. Furthermore, it allows to study the width and the depth of the cracks which might be very helpful to study the durability of the beams. It is also useful to study the damage level of the beam.

- The beneficial effect of fibers was also showed from a structural point of view. The good performance of mixes with fibers was also reported, especially mixes with steel fibers.

8.3 Future works

Once the good performance of EAFS concrete has been showed, further analysis of the structural response are needed to take a step from material-scale to structural-scale. In order to extend the applicability, tests in large-scale elements must be carried out to study issues such as confinement level of concrete, bonding laws, response to dynamics loads, the shear behavior, etc. For instance, achieving this item enable to design structural elements in earthquakes-zones increasing the service life of the structures.

As regards fibers, studies of fiber distribution and their performance will improve the accurateness of the solution of the numerical results. The influence of size-scale effects on the experimental results must be also studied to understand better the postpeak behavior of the composite. An alternative tests might be carried out to determine the mechanical parameters more accurately.

The numerical tool can be improved by implementing new constitutive models or by using other techniques to model the fracture and the bridging phenomena. The library of constitutive models can be extended by including elastoplastic models for concrete. The modeling of traditional reinforcements can also be improved by adding bounding laws. Implementing all this in a more efficient code will save computational time and it would facilitate the use of it.

The presented framework might be improved in terms of experimentation and modeling. More experiments are required to validate the proposed framework to design fiber reinforced structural elements. It will be useful to study other issues such as the behavior of plates and the substitution of conventional reinforcements by fibers.

References

[1] Abbas, S. and Nehdi, M. L. (2018). Mechanical Behavior of RC and SFRC Precast Tunnel Lining Segments under Chloride Ions Exposure. *Journal of Materials in Civil Engineering*, 30(4):04018047.

[2] Agarwal, S. K., Masood, I., and Malhotra, S. K. (2000). Compatibility of superplasticizers with different cements. *Construction and Building Materials*, 14(5):253–259.

[3] Al-Ghamdy, D. O., Wight, J. K., and Tons, E. (1994). Flexural Toughness of Steel Fiber Reinforced Concrete. *JKAU: Eng. Sci*, 6:81–97.

[4] Alberti, M., Enfedaque, A., and Gálvez, J. (2017). Fibre reinforced concrete with a combination of polyolefin and steel-hooked fibres. *Composite Structures*, 171:317–325.

[5] Alberti, M. G., Enfedaque, A., Gálvez, J. C., Cánovas, M. F., and Osorio, I. R. (2014). Polyolefin fiber-reinforced concrete enhanced with steel-hooked fibers in low proportions. *Materials and Design*, 60:57–65.

[6] Alessi, R., Marigo, J.-J., and Vidoli, S. (2014). Digital Object Identifier (Gradient Damage Models Coupled with Plasticity and Nucleation of Cohesive Cracks. *Arch. Rational Mech. Anal*, 214:575–615.

[7] Ambati, M. and De Lorenzis, L. (2016). Phase-field modeling of brittle and ductile fracture in shells with isogeometric NURBS-based solid-shell elements. *Computer Methods in Applied Mechanics and Engineering*, 312:351–373.

[8] Ambati, M., Gerasimov, ·. T., and De Lorenzis, ·. L. (2015). Phase-field modeling of ductile fracture. *Computational Mechanics*, 55:1017–1040.

[9] Ambrosio, L. and Tortorelli, V. M. (1990). Approximation of functional depending on jumps by elliptic functional via t-convergence. *Communications on Pure and Applied Mathematics*, 43(8):999–1036.

[10] Armero, F. and Garikipati, K. (1996). An analysis of strong discontinuities in multiplicative finite strain plasticity and their relation with the numerical simulation of strain localization in solids. *International Journal of Solids and Structures*, 33(20-22):2863–2885.

[11] Arosio V, Arrigoni A, and Dotelli G (2019). Reducing water footprint of building sector: concrete with seawater and marine aggregates. In *IOP Conference Series: Earth and Environmental Science*.

[12] Arribas, I., Santamaría, A., Ruiz, E., Ortega-López, V., and Manso, J. M. (2015). Electric arc furnace slag and its use in hydraulic concrete. *Construction and Building Materials*, 90:68–79.

[13] Arribas, I., Vegas, I., San-José, J., and Manso, J. M. (2014). Durability studies on steelmaking slag concretes. *Materials & Design*, 63:168–176.

[14] Badr, A., Ashour, A. F., and Platten, A. K. (2006). Statistical variations in impact resistance of polypropylene fibre-reinforced concrete. *International Journal of Impact Engineering*, 32(11):1907–1920.

[15] Balouch, S., Forth, J., and Granju, J.-L. (2009). Surface corrosion of steel fibre reinforced concrete. *Cement and Concrete Composites*, 40(3):410–414.

[16] Banthia, N., Azzabi, M., and Pigeon, M. (1993). Restrained shrinkage cracking in fibre-reinforced cementitious composites. *Materials and Structures*, 26(7):405–413.

[17] Banthia, N. and Gupta, R. (2006). Influence of polypropylene fiber geometry on plastic shrinkage cracking in concrete. *Cement and Concrete Research*, 36(7):1263–1267.

[18] Banthia, N., Mindess, S., and Trottier, J. (1996). Impact Resistance of Steel Fiber Reinforced Concrete. *Aci materials journal*, 93(5).

[19] Banthia, N. and Sappakittipakorn, M. (2007). Toughness enhancement in steel fiber reinforced concrete through fiber hybridization. *Cement and Concrete Research*, 37(9):1366–1372.

[20] Barbato, M. (2009). Efficient finite element modelling of reinforced concrete beams retrofitted with fibre reinforced polymers. *Computers and Structures*, 87(3-4):167–176.

[21] Barcelo, L., Kline, J., Walenta, G., and Gartner, E. (2014). Cement and carbon emissions. *Materials and Structures/Materiaux et Constructions*, 47(6):1055–1065.

[22] Barros, J., Cunha, V., Ribeiro, A., and Antunes, J. (2005). Post-cracking behaviour of steel fiber reinforced concrete. *Materials and Structures*, 38:47–56.

[23] Barros, J., Pereira, E., Ribeiro, A., Cunha, V., and Antunes, J. (2004). Self-compacting steel fibre reinforced concrete for precasted sandwich panels – experimental and numerical research. Technical report, International RILEM symposium on fibre reinforced concrete, Varenna.

[24] Baum, H., Bentur, A., and Soroka, I. (1985). Properties and structure of oil shale ash pastes. II: Mechanical properties and structure. *Cement and Concrete Research*, 15(3):391–400.

[25] Bažant, Z. P. and Becq-Giraudon, E. (2002). Statistical prediction of fracture parameters of concrete and implications for choice of testing standard. *Cement and Concrete Research*, 32(4):529–556.

[26] Behnood, A., Verian, K. P., and Modiri Gharehveran, M. (2015). Evaluation of the splitting tensile strength in plain and steel fiber-reinforced concrete based on the compressive strength. *Construction and Building Materials*, 98:519–529.

[27] Belletti, B., Cerioni, R., Meda, A., and Plizzari, G. (2008). Design Aspects on Steel Fiber-Reinforced Concrete Pavements. *Journal of Materials in Civil Engineering*, 20.

[28] Belytschko, T. and Black, T. (1999). Elastic crack growth in finite elements with minimal remeshing. *International Journal for numerical methods in engineering*, 620(July 1998):601–620.

[29] Belytschko, T., Fish, J., and Engelmann, B. E. (1988). A finite element with embedded localization zones. *Computer Methods in Applied Mechanics and Engineering*, 70(1):59–89.

[30] Belytschko, T., Gracie, R., and Ventura, G. (2009). A Review of Extended/Generalized Finite Element Methods for Material Modelling. *Modeling and Simulation in Materials Science and Engineering*, 17(5).

[31] Bencardino, F., Rizzuti, L., Spadea, G., and Swamy, R. N. (2008). Stress-Strain Behavior of Steel Fiber-Reinforced Concrete in Compression. *Journal of Materials in Civil Engineering*, 20(3).

[32] Borden, M. J., Verhoosel, C. V., Scott, M. A., Hughes, T. J., and Landis, C. M. (2012). A phase-field description of dynamic brittle fracture. *Computer Methods in Applied Mechanics and Engineering*, 217-220:77–95.

[33] Bosco, M., Ferrara, E., Ghersi, A., Marino, E. M., and Rossi, P. P. (2016). Improvement of the model proposed by Menegotto and Pinto for steel. *Engineering Structures*, 124:442–456.

[34] Bourdin, B., Larsen, C. J., Richardson, C. L., Bourdin, B., Larsen, C. J., and Richardson, C. L. (2011). A time-discrete model for dynamic fracture based on crack regularization. *Boll. Un. Mat. Ital. B*, 168(8):105–123.

[35] Burgos-Montes, O., Palacios, M., Rivilla, P., and Puertas, F. (2012). Compatibility between superplasticizer admixtures and cements with mineral additions. *Construction and Building Materials*, 31:300–309.

[36] Carlesso, D. M., de la Fuente, A., and Cavalaro, S. H. P. (2019). Fatigue of cracked high performance fiber reinforced concrete subjected to bending. *Construction and Building Materials*, 220:444–455.

[37] CEB-FIB (2012a). Model Code 2010 (Volume 1).

[38] CEB-FIB (2012b). *Model Code 2010 (Volume 2)*.

[39] Cervera, M., Chiumenti, M., and Agelet de Saracibar, C. (2004). Shear band localization via local J2 continuum damage mechanics. *Computer Methods in Applied Mechanics and Engineering*, 193(9-11):849–880.

[40] Chandra, S. and Björnström, J. (2002). Influence of cement and superplasticizers type and dosage on the fluidity of cement mortars - Part I. *Cement and Concrete Research*, 32(10):1605–1611.

[41] Chen, J. J., Kwan, A. K., and Jiang, Y. (2014). Adding limestone fines as cement paste replacement to reduce water permeability and sorptivity of concrete. *Construction and Building Materials*, 56:87–93.

[42] Chiaia, B., Fantilli, A. P., and Vallini, P. (2009). Combining fiber-reinforced concrete with traditional reinforcement in tunnel linings. *Engineering Structures*, 31(7):1600–1606.

[43] Comi, C. and Mariani, S. (2007). Extended finite element simulation of quasi-brittle fracture in functionally graded materials. *Computer Methods in Applied Mechanics and Engineering*, 196(41-44):4013–4026.

[44] Corinaldesi, V. and Moriconi, G. (2004). Durable fiber reinforced self-compacting concrete. *Cement and Concrete Research*, 34:249–254.

[45] Darquennes, A., Rozière, E., Khokhar, M. I. A., Turcry, P., Loukili, A., and Grondin, F. (2012). Long-term deformations and cracking risk of concrete with high content of mineral additions. *Materials and Structures*.

[46] Dellinghausen, L. M., Gastaldini, A. L., Vanzin, F. J., and Veiga, K. K. (2012). Total shrinkage, oxygen permeability, and chloride ion penetration in concrete made with white Portland cement and blast-furnace slag. *Construction and Building Materials*, 37:652–659.

[47] Di Prisco, M., Plizzari, G., and Vandewalle, L. (2009). Fibre reinforced concrete: new design perspectives. *Materials and Structures and Structures*, 42.

[48] Ding, Y. (2011). Investigations into the relationship between deflection and crack mouth opening displacement of SFRC beam. *Construction and Building Materials*, 25(5):2432–2440.

[49] Dinh, H. H. (2009). *Shear behavior of steel fiber reinforced concrete beams without stiruup reinforcement*. PhD thesis, The University of Michigan.

[50] Djwantoro, H., Wallah, S. E., Sumajouw, D. M. J., and Rangan, B. V. (2004). On the Development of Fly Ash-Based Geopolymer Concrete. *ACI Materials Journal*, 101(6).

[51] Dolbow, J., Moës, N., and Belytschko, T. (2001). An extended finite element method for modeling crack growth with frictional contact. *Computer Methods in Applied Mechanics and Engineering*, 190:6825–6846.

[52] El-Dieb, A. S. and Reda Taha, M. M. (2012). Flow characteristics and acceptance criteria of fiber-reinforced self-compacted concrete (FR-SCC). *Construction and Building Materials*, 27(1):585–596.

[53] Elices, M., Guinea, G. V., and Planas, J. (1992). Measurement of the fracture energy using three-point bend tests: Part 3—influence of cutting theP-δ tail. *Materials and Structures*, 25(6):327–334.

[54] Escalante, J., Gómez, L., Johal, K., Mendoza, G., Mancha, H., and Méndez, J. (2001). Reactivity of blast-furnace slag in Portland cement blends hydrated under different conditions. *Cement and Concrete Research*, 31(10):1403–1409.

[55] Fatih Altun, Tefaruk Haktanir, and Kamura Ari (2007). Effects of steel fiber addition on mechanical properties of concrete and RC beams. *Construction and Building Materials*, 21(3):654–661.

[56] Fllippou, F. E., Popov, E. P., and Bertero, V. V. (1983). Effects of bond deterioration on hysteric behavior of reinforced concrete joints. Technical report.

[57] Folliard, K. J. and Berke, N. S. (1997). Properties of high-performance concrete containing shrinkage-reducing admixture. *Cement and Concrete Research*, 27(9):1357–1364.

[58] Francfort, G. and Marigo, J.-J. (1998). Revisiting brittle fracture as an energy minimization problem. *Journal of the Mechanics and Physics of Solids*, 46(8):1319–1342.

[59] Fuente-Alonso, J. A., Ortega-López, V., Skaf, M., Aragón, Á., and San-José, J. T. (2017). Performance of fiber-reinforced EAF slag concrete for use in pavements. *Construction and Building Materials*, 149:629–638.

[60] Germano, F., Tiberti, G., and Plizzari, G. (2016). Experimental behavior of SFRC columns under uniaxial and biaxial cyclic loads. *Composites Part B*, 85:76–92.

[61] Gettu, R., Gardner, D. R., Saldivar, H., and Barragfin, B. E. (2004). Study of the distribution :and orientation of fibers in SFRC specimens. *Materials and Structures*.

[62] Geuzaine, C. and Remacle, J.-F. (2009). Gmsh: a three-dimensional finite element mesh generator with built-in pre-and post-processing facilities. *International Journal for Numerical Methods in Engineering*, 0:1–24.

[63] Gonçalves, J., Tavares, L., Toledo Filho, R., Fairbairn, E., and Cunha, E. (2007). Comparison of natural and manufactured fine aggregates in cement mortars. *Cement and Concrete Research*, 37(6):924–932.

[64] Granju, J.-L. and Ullah Balouch, S. (2005). Corrosion of steel fibre reinforced concrete from the cracks. *Cement and Concrete Research*, 35(3):572–577.

[65] Grassl, P. and Jirásek, M. (2006). Damage-plastic model for concrete failure. *International Journal of Solids and Structures*, 43(22-23):7166–7196.

[66] Griffith, A. A. (1920). The phenomena of rupture and flow in solids. *Royal Society of London. Series A*, 221:163–198.

[67] Gruyaert, E., Van Den Heede, P., Maes, M., and De Belie, N. (2012). Investigation of the influence of blast-furnace slag on the resistance of concrete against organic acid or sulphate attack by means of accelerated degradation tests. *Cement and Concrete Research*, 42(1):173–185.

[68] Guerini, V., Conforti, A., Plizzari, G., and Kawashima, S. (2018). Influence of Steel and Macro-Synthetic Fibers on Concrete Properties. *Fibers*, 6(3):47.

[69] Haach, V. G., Vasconcelos, G., and Lourenço, P. B. (2011). Influence of aggregates grading and water/cement ratio in workability and hardened properties of mortars. *Construction and Building Materials*, 25(6):2980–2987.

[70] Han, T. Y., Lin, W. T., Cheng, A., Huang, R., and Huang, C. C. (2012). Influence of polyolefin fibers on the engineering properties of cement-based composites containing silica fume. *Materials and Design*, 37:569–576.

[71] Higgins, D. D. (2003). Increased sulfate resistance of ggbs concrete in the presence of carbonate. *Cement and Concrete Composites*, 25:913–919.

[72] Hillerborg, A. (1985). Results of three comparative test series for determining the fracture energy of concrete. *Materials and Structures*, 18(5):407–413.

[73] Hrynyk, T. D. and Vecchio, F. J. (2013). Behavior of Steel Fiber-Reinforced Concrete Slabs under Impact Load. *ACI Structural Journal*.

[74] Hughes, B. and Fattuhi, N. (1977). Stress-strain curves for fibre reinforced concrete in compression. *Cement and Concrete Research*, 7(2):173–183.

[75] Hwan Oh, B., Park, D. G., Kim, J. C., and Choi, Y. C. (2005). Experimental and theoretical investigation on the postcracking inelastic behavior of synthetic fiber reinforced concrete beams. *Cement and Concrete Research*, 35(2):384–392.

[76] ichi Tazawa, E. and Miyazawa, S. (1995). Experimental study on mechanism of autogenous shrinkage of concrete. *Cement and Concrete Research*, 25(8):1633–1638.

[77] Jamshidi Avanaki, M., Hoseini, A., Vahdani, S., and de la Fuente, A. (2018). Numerical-aided design of fiber reinforced concrete tunnel segment joints subjected to seismic loads. *Construction and Building Materials*, 170:40–54.

[78] Jin, Q. and Li, V. C. (2019). Development of lightweight engineered cementitious composite for durability enhancement of tall concrete wind towers. *Cement and Concrete Composites*, 96:87–94.

[79] Karaman, I., Sehitoglu., H., Chumlyakov, Y. I., Maier, H. J., and Kireeva, I. V. (2001). The effect of twinning and slip on the bauschinger effect of hadfield steel single crystals. *Metallurgical and Materials Transactions A: Physical Metallurgy and Materials Science*, 32(13):695–706.

[80] Kim, Y.-Y., Lee, K.-M., Bang, J.-W., and Kwon, S.-J. (2014). Effect of W/C Ratio on Durability and Porosity in Cement Mortar with Constant Cement Amount. *Advances in Materials Science and Engineering*, 2014:1–11.

[81] Kizilkanat, A. B., Kabay, N., Akyüncü, V., Chowdhury, S., and Akça, A. H. (2015). Mechanical properties and fracture behavior of basalt and glass fiber reinforced concrete: An experimental study. *Construction and Building Materials*, 100:218–224.

[82] Kwak, Y.-k., Eberhard, M. O., Kim, W.-s., and Kim, J. (2002). Shear Strength of Steel Fiber-Reinforced Concrete Beams without Stirrups. *ACI Structural Journal*, 99.

[83] Laranjeira, F., Grünewald, S., Walraven, J., Blom, C., Molins, C., and Aguado, A. (2011). Characterization of the orientation profile of steel fiber reinforced concrete. *Materials and Structures*, 44:1093–1111.

[84] Laranjeira, F., Molins, C., and Aguado, A. (2010). Predicting the pullout response of inclined hooked steel fibers. *Cement and Concrete Research*, 40:1471–1487.

[85] Lee, H.-H. (2007a). Shear strength and behavior of steel fiber reinforced concrete columns under seismic loading. *Engineering Structures*, 29(7):1253–1262.

[86] Lee, H.-H. (2007b). Shear strength and behavior of steel fiber reinforced concrete columns under seismic loading. *Engineering Structures*, 29:1253–1262.

[87] Levy, S. M. (2012). *Construction Calculations Manual*. Elsevier.

[88] Li, J., Qiu, J., He, S., and Yang, E.-h. (2018). Micromechanics-based design of strain hardening cementitious composites (SHCC). In Mechtcherine, V., Slowik, V., and Kabele, P., editors, *Strain-Hardening Cement-Based Composites*, volume 15.

[89] Li, V. C., Stang, H., and Krenchel, H. (1993). Micromechanics of crack bridging in fibre-reinforced concrete. *Materials and Structures*, 26(8):486–494.

[90] Li, V. C., Ward, R., and Hamza, A. M. (1992). Steel and synthetic fibers as shear reinforcement. *ACI Materials Journal*, 89(5):499–508.

[91] Lim, D. and Oh, B. (1999). Experimental and theoretical investigation on the shear of steel fibre reinforced concrete beams. *Engineering Structures*, 21(10):937–944.

[92] Liu, C., Prévost, J. H., and Sukumar, N. (2019). Modeling branched and intersecting faults in reservoir-geomechanics models with the extended finite element method. *International Journal for Numerical and Analytical Methods in Geomechanics*, 43(12):2075–2089.

[93] Maalej, M., Quek, S. T., and Zhang, J. (2005). Behavior of Hybrid-Fiber Engineered Cementitious Composites Subjected to Dynamic Tensile Loading and Projectile Impact. *Journal of Materials in Civil Engineering*, 17:143–152.

[94] Majain, N., Rahman, A. B., Mohamed, R. N., and Adnan, A. (2019). Effect of steel fibers on self-compacting concrete slump flow and compressive strength. In *IOP Conference Series: Materials Science and Engineering*, volume 513. Institute of Physics Publishing.

[95] Mannan, M. and Ganapathy, C. (2004). Concrete from an agricultural waste-oil palm shell (OPS). *Building and Environment*, 39(4):441–448.

[96] Manso, J. M., Gonzalez, J. J., and Polanco, J. A. (2004). Electric Arc Furnace Slag in Concrete. *Journal of Materials in Civil Engineering*, 16(6):639–645.

[97] Manso, J. M., Ortega-López, V., Polanco, J. A., and Setién, J. (2013). The use of ladle furnace slag in soil stabilization. *Construction and Building Materials*, 40:126–134.

[98] Manso, J. M., Polanco, J. A., Losañez, M., and González, J. J. (2006). Durability of concrete made with EAF slag as aggregate. *Cement and Concrete Composites*, 28(6):528–534.

[99] Mansur, M. A., Asce, M., Ong, K. C. G., and Paramasivam, P. (1986). Shear strength of fibrous concrete beams without stirrups. *Journal of Structural Engineering*, 112(9).

[100] Manzoli, O. L., Gamino, A. L., Rodrigues, E. A., and Claro, G. K. (2012). Modeling of interfaces in two-dimensional problems using solid finite elements with high aspect ratio. *Computers and Structures*, 94-95:70–82.

[101] Manzoli, O. L., Maedo, M. A., Bitencourt, L. A., and Rodrigues, E. A. (2016). On the use of finite elements with a high aspect ratio for modeling cracks in quasi-brittle materials. *Engineering Fracture Mechanics*, 153:151–170.

[102] Marcos, I., San-José, J. T., Garmendia, L., Santamaría, A., and Manso, J. M. (2016). Central lessons from the historical analysis of 24 reinforced-concrete structures in northern Spain. *Journal of Cultural Heritage*, 20:649–659.

[103] Marcos, I., San-José, J. T., Santamaría, A., and Garmendia, L. (2018). Early Concrete Structures: Patented Systems and Construction Features. *International Journal of Architectural Heritage*, 12(3):310–319.

[104] Massicotte, B., Bélanger, A., and Moffatt, K. (2000). Analysis and design of SFRC bridge decks. In *5th RILEM Symposium on Fibre-Reinforced Concretes (FRC)*, pages 119–128.

[105] McMahon, J. A. and Birely, A. C. (2018). Experimental Performance of Steel Fiber Reinforced Concrete Bridge Deck. *Journal of Bridge Engineering*, 23(10):04018074.

[106] Meyer, C. (2009). The greening of the concrete industry. *Cement and Concrete Composites*, 31(8):601–605.

[107] Miloud, B. (2005). Permeability and porosity characteristics of steel fiber reinforced concrete. *Asian Journal of Civil Engineering (Building and housing)*, 6(4):317–330.

[108] Ministerio de Fomento (2008). Code on structural concrete EHE-08. Technical report, Madrid.

[109] Mirsayah, A. A. and Banthia, N. (2002). Shear Strength of Steel Fiber-Reinforced Concrete. *ACI Materials Journal*, 99:473–479.

[110] Mobasher, B. and Destree, X. (2010). Design and construction aspects of steel fiber-reinforced concrete elevated slabs. *American Concrete Insititut, ACI Special Publication*, pages 95–107.

[111] Moës, N. and Belytschko, T. (2002). Extended finite element method for cohesive crack growth. *Engineering Fracture Mechanics*, 69:813–833.

[112] Mohammadi, Y., Carkon-Azad, R., Singh, S., and Kaushik, S. (2009). Impact resistance of steel fibrous concrete containing fibres of mixed aspect ratio. *Construction and Building Materials*, 23(1):183–189.

[113] Mohammadi, Y., Singh, S., and Kaushik, S. (2008). Properties of steel fibrous concrete containing mixed fibres in fresh and hardened state. *Construction and Building Materials*, 22(5):956–965.

[114] Mohammed, T. U., Otsuki, N., Hisada, M., and Shibata, T. (2001). Effect of crack width and bar types on corrosion of steel in concrete. *Journal of Materials in Civil Engineering*, 13(3):194–201.

[115] Mollah, M. Y., Adams, W. J., Schennach, R., and Cocke, D. L. (2000). Review of cement-superplasticizer interactions and their models. *Advances in Cement Research*, 12(4):153–161.

[116] Nataraja, M., Dhang, N., and Gupta, A. (1999). Statistical variations in impact resistance of steel fiber-reinforced concrete subjected to drop weight test. *Cement and Concrete Research*, 29(7):989–995.

[117] Neville, A. and Brooks, J. (2010). *Concrete technology (2nd ed.)*. Pearson Education Limited, limited pe edition.

[118] Nguyen, T. T., Yvonnet, J., Zhu, Q.-Z., Bornert, M., Chateau, C., Yvonnet, J., Zhu, Q.-Z., Bornert, M., and Chateau, C. (2015). A phase field method to simulate crack nucleation and propagation in strongly heterogeneous materials from direct imaging of their microstructure. *Engineering Fracture Mechanics*, 139:18–39.

[119] Nmai, C. K. (1998). Cold weather concreting admixtures. *Cement and Concrete Composites*, 20(2-3):121–128.

[120] Nogales, A. and De, A. (2020). Crack width design approach for fi bre reinforced concrete tunnel segments for TBM thrust loads. *Tunnelling and Underground Space Technology*, 98(December 2019):103342.

[121] Oh, B. H. (1992). Flexural analysis or reinforced concrete beams containing steel fibers. *Journal of Structural Engineering*, 118(10).

[122] Okeniyi, J. O., Loto, C. A., and Popoola, A. P. I. (2014). Morinda Lucida Effects on Steel-reinforced Concrete in 3.5% NaCl: Implications for Corrosion-protection of Wind-energy Structures in Saline/Marine Environments. *Energy Procedia*, 50:421–428.

[123] Oliver, J., Huespe, A., Pulido, M., and Chaves, E. (2002). From continuum mechanics to fracture mechanics: the strong discontinuity approach. *Engineering Fracture Mechanics*, 69:113–136.

[124] Oliver, J., Huespe, A. E., Blanco, S., and Linero, D. L. (2006). Stability and robustness issues in numerical modeling of material failure with the strong discontinuity approach. *Computer Methods in Applied Mechanics and Engineering*, 195(52):7093–7114.

[125] Ortega-López, V., Fuente-Alonso, J. A., Santamaría, A., San-José, J. T., and Aragón, Á. (2018). Durability studies on fiber-reinforced EAF slag concrete for pavements. *Construction and Building Materials*, 163:471–481.

[126] Ortiz, J. A., de la Fuente, A., Mena Sebastia, F., Segura, I., and Aguado, A. (2017). Steel-fibre-reinforced self-compacting concrete with 100% recycled mixed aggregates suitable for structural applications. *Construction and Building Materials*, 156:230–241.

[127] Ortiz, M., Leroy, Y., and Needleman, A. (1987). A finite element method for localized failure analysis. *Computer Methods in Applied Mechanics and Engineering*, 61(2):189–214.

[128] Osmanovic, Z., Haračić, N., and Zelić, J. (2018). Properties of blastfurnace cements (CEM III/A, B, C) based on Portland cement clinker, blastfurnace slag and cement kiln dusts. *Cement and Concrete Composites*, 91:189–197.

[129] Pakravan, H., Latifi, M., and Jamshidi, M. (2017). Hybrid short fiber reinforcement system in concrete: A review. *Construction and Building Materials*, 142:280–294.

[130] Pang, Y. and Li, L. (2018). Seismic collapse assessment of bridge piers constructed with steel fibers reinforced concrete. *PLOS ONE*, 13(7):e0200072.

[131] Papadopoulos, V., Murcia-Delso, J., and Benson Shing, P. (2018). Development of headed bars in slab-column joints of reinforced concrete slab bridges. *ACI Structural Journal*, 115.

[132] Park, S. S., Kwon, S. J., and Jung, S. H. (2012). Analysis technique for chloride penetration in cracked concrete using equivalent diffusion and permeation. *Construction and Building Materials*, 29:183–192.

[133] Parker, A. P., Troiano, E., Underwood, J. H., and Mossey, C. (2003). Characterization of steels using a revised kinematic hardening model incorporating Bauschinger effect. In *Journal of Pressure Vessel Technology, Transactions of the ASME*, volume 125, pages 277–281.

[134] Parvez, A. and Foster, S. J. (2015). Fatigue Behavior of Steel-Fiber-Reinforced Concrete Beams. *Journal of Structural EngineeringStructural Engineering*, 141(4).

[135] Pellegrino, C. and Faleschini, F. (2013). Experimental behavior of reinforced concrete beams with electric arc furnace slag as recycled aggregate. *ACI Materials Journal*, 110(2):197–205.

[136] Pellegrino, C. and Gaddo, V. (2009). Mechanical and durability characteristics of concrete containing EAF slag as aggregate. *Cement and Concrete Composites*, 31(9):663–671.

[137] Petek Gursel, A., Masanet, E., Horvath, A., and Stadel, A. (2014). Life-cycle inventory analysis of concrete production: A critical review. *Cement and Concrete Composites*, 51:38–48.

[138] Pinto, M. and Emilio, P. (1973). Method of analysis for cyclically loaded R . C . plane frames including changes in geometry and non-elastic behaviour of elements under combined normal force and bending.

[139] Priestley, M. J. N., Verma, R., and Xino, Y. (1994). Seismic shear strength of reinforced concrete columns. *Journal of Structural Engineering*, 120.

[140] Quilligan, A., O'Connor, A., and Pakrashi, V. (2012). Fragility analysis of steel and concrete wind turbine towers. *Engineering Structures*, 36:270–282.

[141] Rao, G. (2001). Generalization of Abrams' law for cement mortars. *Cement and Concrete Research*, 31(3):495–502.

[142] Rapoport, J., Aldea, C.-M., Shah, S. P., Ankenman, B., Karr, A. F., and Aldea, C. (2001). Permeability of Cracked Steel Fiber-Reinforced Concrete. Technical report.

[143] Ravi Mullapudi, T. and Ayoub, A. (2010). Modeling of the seismic behavior of shear-critical reinforced concrete columns. *Engineering Structures*, 32(11):3601–3615.

[144] Reis, J. and Ferreira, A. (2004). A contribution to the study of the fracture energy of polymer concrete and fibre reinforced polymer concrete. *Polymer Testing*, 23(4):437–440.

[145] Rondi, L., Bregoli, G., Sorlini, S., Cominoli, L., Collivignarelli, C., and Plizzari, G. (2016). Concrete with EAF steel slag as aggregate: A comprehensive technical and environmental characterisation. *Composites Part B: Engineering*, 90:195–202.

[146] Rossi, P. and Parant, E. (2008). Damage mechanisms analysis of a multi-scale fibre reinforced cement-based composite subjected to impact and fatigue loading conditions. *Cement and Concrete Research*, 38(3):413–421.

[147] Ruiz, G., Elices, M., and Planas, J. (1998). Experimental study of fracture of lightly reinforced concrete beams. *Materials and Structures*, 31(December):683–691.

[148] Samir A. Ashour, Faisal F. Wafa, and Mohmd I. Kamal (2000). Effect of the concrete compressive strength and tensile reinforcement ratio on the flexural behavior of fibrous concrete beams. *Engineering Structures*, 22(9):1145–1158.

[149] San-José, J. T., Vegas, I., Arribas, I., and Marcos, I. (2014). The performance of steel-making slag concretes in the hardened state. *Materials & Design*, 60:612–619.

[150] Sánchez, M., Manzoli, O. L., and Guimarães, L. J. (2014). Modeling 3-D desiccation soil crack networks using a mesh fragmentation technique. *Computers and Geotechnics*, 62:27–39.

[151] Santamaría, A., Orbe, A., Losañez, M., Skaf, M., Ortega-Lopez, V., and González, J. J. (2017). Self-compacting concrete incorporating electric arc-furnace steelmaking slag as aggregate. *Materials & Design*, 115:179–193.

[152] Santamaría, A., Ortega-López, V., Skaf, M., Chica, J. A., and Manso, J. M. (2019). The study of properties and behavior of self compacting concrete containing Electric Arc Furnace Slag (EAFS) as aggregate. *Ain Shams Engineering Journal*, (xxxx):1–13.

[153] Santamaría, A., Rojí, E., Skaf, M., Marcos, I., and González, J. J. (2016). The use of steelmaking slags and fly ash in structural mortars. *Construction and Building Materials*, 106:364–373.

[154] Santos, A. C., Ortiz-Lozano, J. A., Villegas, N., and Aguado, A. (2015). Experimental study about the effects of granular skeleton distribution on the mechanical properties of self-compacting concrete (SCC). *Construction and Building Materials*, 78:40–49.

[155] Sear, L., Dews, J., Kite, B., Harris, F., and Troy, J. (1996). Abrams law, air and high water-to-cement ratios. *Construction and Building Materials*, 10(3):221–226.

[156] Shah, J. (1996). A Common Framework for Curve Evolution, Segmentation and Anisotropic Diffusion. Technical report.

[157] Shah, S. P., Swartz, S. E., and Ouyang, C. (1995). *Fracture mechanics of concrete: applications of fracture mechanics to concrete, rock and other quasi-brittle materials.*

[158] Shen, D., Shi, X., Zhu, S., Duan, X., and Zhang, J. (2016). Relationship between tensile Young's modulus and strength of fly ash high strength concrete at early age. *Construction and Building Materials*, 123:317–326.

[159] Skaf, M., Manso, J. M., Aragón, Á., Fuente-Alonso, J. A., and Ortega-López, V. (2017). EAF slag in asphalt mixes: A brief review of its possible re-use. *Resources, Conservation and Recycling*, 120:176–185.

[160] Smadi, M. M. and Haddad, R. H. (2003). The use of oil shale ash in Portland cement concrete. *Cement and Concrete Composites*, 25(1):43–50.

[161] Smalley, A. J. and Pantermuehl, P. J. (2006). Realistically assessing load severity on concrete foundations and mounting systems for large reciprocating compressors. *ACI Structural Journal*, 103.

[162] Song, J.-H., Wang, H., and Belytschko, T. (2007). A comparative study on finite element methods for dynamic fracture. *Computational mechani*, 42:239–250.

[163] Sorelli, L., Meda, A., Plizzari, G. A., and Rossi, B. (2004). Experimental investigation on slabs on grade: Steel Fibers Vs Convenctional reinforcement. In *6th RILEM Symposium on Fibre-Reinforced Concretes (FRC) -.*

[164] Sorelli, L. G., Meda, . A., and Plizzari, G. A. (2005). Bending and Uniaxial Tensile Tests on Concrete Reinforced with Hybrid Steel Fibers. *Journal of materials in civil engineering.*

[165] Spasojević, A. (2008). *Structural ImplIcatIonS of ultra-HIgH performance fIbre-reInforced concrete In brIdge deSIgn.* À la faculté de l'environnement naturel, architectural et construit, École Polytechnique Fédërale de Lausanne.

[166] Stähli, P., Custer, R., and van Mier, J. G. M. (2008). On flow properties, fibre distribution, fibre orientation and flexural behaviour of FRC. *Materials and Structures*, 41(1):189–196.

[167] Stavridis, A. and Shing, P. B. (2010). Finite-Element Modeling of Nonlinear Behavior of Masonry-Infilled RC Frames. *Journal of Structural Engineering*, 136(3):285–296.

[168] Su, H., Yang, J., Ling, T.-C., Ghataora, G. S., and Dirar, S. (2015). Properties of concrete prepared with waste tyre rubber particles of uniform and varying sizes. *Journal of Cleaner Production*, 91:288–296.

[169] Sukumar, N., Dolbow, J. E., and Moës, N. (2015). Extended finite element method in computational fracture mechanics: a retrospective examination-of-unity enrichment · X-FEM. *International Journal of Fracture*, 196:189–206.

[170] Swartz, S. E. and Yap, S. T. (1988). The influence of dead load on fracture energy measurements using the RILEM method. *Materials and Structures*, 21(6):410–415.

[171] The European Federation of Specialist Construction Chemicals and Concrete Systems (2002). The European Guidelines for Self Compacting Concrete. Technical report.

[172] Thorneycroft, J., Orr, J., Savoikar, P., and Ball, R. (2018). Performance of structural concrete with recycled plastic waste as a partial replacement for sand. *Construction and Building Materials*, 161:63–69.

[173] Torrents, J. M., Blanco, A., Pujadas, P., Aguado, A., Juan-García, P., and Sánchez-Moragues, M. Á. (2012). Inductive method for assessing the amount and orientation of steel fibers in concrete. *Materials and Structures*, 45(10):1577–1592.

[174] Trottier, J.-F. and Banthia, N. (1994). Toughness characterization of steel-fiber reinforced concrete. *Journal of Materials in Civil Engineering*, 6(2):6070.

[175] Tsivilis, S., Chaniotakis, E., Kakali, G., and Batis, G. (2002). An analysis of the properties of Portland limestone cements and concrete. *Cement and Concrete Composites*, 24(3-4):371–378.

[176] UNE 12390-13 (2014). Determination of secant modulus of elasticity in compression.

[177] UNE 12390-3 (2014). Compressive strength of test specimens.

[178] UNE 12390-6:2010 (2014). Tensile strength.

[179] UNE 12390-8:2009 (2011). Depth of penetration of water under pressure.

[180] UNE 14651:2005+A1 (2008). Test method for metallic fibre concrete. Measuring the flexural tensile strength.

[181] UNE 197-1:2011 (2013). Composition, specifications and conformity criteria for commo on cements.

[182] UNE 83509 (2004). Flexure strength.

[183] UNE 83510:2004 (2004). Determination of the index of tenacity and strength at the first crack.

[184] UNE 83514 (2005). Determination of the impact strength.

[185] UNE 83982 (2008). Determination of the capillar suction in hardened concrete. Fagerlund method.

[186] UNE-EN 83318:1994 (1994). Determination of the length change.

[187] Van Mier, J. and Van Vliet, M. (2003). Influence of microstructure of concrete on size/scale effects in tensile fracture. *Engineering Fracture Mechanics*, 70(16):2281–2306.

[188] Vandewalle, L. (2000). Cracking behaviour of concrete beams reinforced with a combination of ordinary reinforcement and steel fibers. *Materials and Structures*, 33:164–170.

[189] Vicente, M. A., Mínguez, J., and González, D. C. (2019). Variation of the pore morphology during the early age in plain and fiber-reinforced high-performance concrete under moisture-saturated curing. *Materials*, 12(6).

[190] V.M.C.F., C., J.A.O., B., and J.S., C. (2007). Pullout behaviour of hooked-end steel fibres in self-compacting concrete. Technical report.

[191] Wang, Z.-L., Liu, Y.-S., and Shen, R. (2008). Stress–strain relationship of steel fiber-reinforced concrete under dynamic compression. *Construction and Building Materials*, 22(5):811–819.

[192] Washburn, E. W. (1921). Note on a method of determining the distribution of pore sizez in a porous material. *Proceedings of the National Academy of Sciences of the United States of America*, 7:115–116.

[193] Wild, S., Khatib, J., and Jones, A. (1996). Relative strength, pozzolanic activity and cement hydration in superplasticised metakaolin concrete. *Cement and Concrete Research*, 26(10):1537–1544.

[194] Wille, K., El-Tawil, S., and Naaman, A. (2014). Properties of strain hardening ultra high performance fiber reinforced concrete (UHP-FRC) under direct tensile loading. *Cement and Concrete Composites*, 48:53–66.

[195] Xu, B. and Shi, H. (2009). Correlations among mechanical properties of steel fiber reinforced concrete. *Construction and Building Materials*, 23(12):3468–3474.

[196] Yeh, I.-C. (2006). Generalization of strength versus water–cementitious ratio relationship to age. *Cement and Concrete Research*, 36(10):1865–1873.

[197] Yoo, D.-Y., Yoon, Y.-S., and Banthia, N. (2015). Flexural response of steel-fiber-reinforced concrete beams: Effects of strength, fiber content, and strain-rate. *Cement and Concrete Composites*, 64:84–92.

[198] Yoshida, F. and Uemori, T. (2002). A model of large-strain cyclic plasticity describing the Bauschinger effect and workhardening stagnation. In *International Journal of Plasticity*, volume 18, pages 661–686.

[199] Yoshitake, I., Zhang, W., Mimura, Y., and Saito, T. (2013). Uniaxial tensile strength and tensile Young's modulus of fly-ash concrete at early age. *Construction and Building Materials*, 40:514–521.

[200] Yousefieh, N., Joshaghani, A., Hajibandeh, E., and Shekarchi, M. (2017). Influence of fibers on drying shrinkage in restrained concrete. *Construction and Building Materials*, 148:833–845.

[201] Zhan, Y. and Meschke, G. (2017). Adaptive Crack Modeling with Interface Solid Elements for Plain and Fiber Reinforced Concrete Structures. *Materials*, 10:771.

[202] Zhang, Y., Fan, J., and Fan, W. (2016). Seismic fragility analysis of concrete bridge piers reinforced by steel fibers. *Advances in Structural Engineering*, 19(5):837–848.

[203] Zhang, Y.-Y., Harries, K. A., and Yuan, W.-C. (2013). Experimental and numerical investigation of the seismic performance of hollow rectangular bridge piers constructed with and without steel fiber reinforced concrete. *Engineering Structures*, 48:255–265.

[204] Zhou, J. K. and Ge, L. M. (2015). Effect of strain rate and water-to-cement ratio on compressive mechanical behavior of cement mortar. *Journal of Central South University*, 22(3):1087–1095.

[205] Živica, V. (2009). Effects of the very low water/cement ratio. *Construction and Building Materials*, 23(12):3579–3582.

[206] Zollo, R. F. (1997). Fiber-reinforced concrete: an overview after 30 years of development. *Cement and Concrete Composites*, 19(2):107–122.

[207] Zongjin, L. (2011). *Advanced concrete technology*. John Wiley & Sons, Inc.